Spectroscopic Insights in the Gas Detection Mechanism of Tin Dioxide Based Gas Sensors

Dissertation

der Mathematisch-Naturwissenschaftlichen Fakultät

der Eberhard Karls Universität Tübingen

zur Erlangung des Grades eines

Doktors der Naturwissenschaften

(Dr. rer. nat.)

vorgelegt von

Diplom Chemiker David Degler
aus Reutlingen

Tübingen

2017

Gedruckt mit Genehmigung der Mathematisch-Naturwissenschaftlichen Fakultät der Eberhard Karls Universität Tübingen.

Tag der mündlichen Qualifikation:	25.07.2017
Dekan:	Prof. Dr. Wolfgang Rosenstiel
1. Berichterstatter:	Prof. Dr. Udo Weimar
2. Berichterstatter:	Prof. Dr. Günter Gauglitz

“We must trust to nothing but facts: These are presented to us by Nature, and cannot deceive. We ought, in every instance, to submit our reasoning to the test of experiment, and never to search for truth but by the natural road of experiment and observation.”

Antoine Laurent de Lavoisier

I. Table of Content

I. Table of Content ..... A
II. List of symbols C
III. List of abbreviations ..... F
1. Introduction and Motivation 1
2. Basic Aspects of Gas Sensing with Tin Dioxide 3
2.1. Definitions for Chemical Sensors 3
2.2. Properties of Tin Dioxide 5
2.2.1. Crystal Structure 5
2.2.2. Optical Active Vibrational Modes 5
2.2.3. Electronic Properties 7
2.2.4. Single Crystal Surfaces 7
2.2.5. Adsorption and Adsorbed Surface Species on SnO_2 9
2.3. Working Principle of Tin Dioxide Based Gas Sensor 16
2.4. Role of Noble Metal Loadings 18
3. Fundamentals of the operando spectroscopic methods 20
3.1. Ex-situ, in-situ and operando methods for gas sensor research 20
3.2. IR spectroscopy 20
3.3. UV/Vis spectroscopy 23
3.4. X-ray Absorption Spectroscopy 23
4. Materials & Experimental Methods 26
4.1. Sample Preparation 26
4.1.1. Powder Preparation 26
4.1.2. Sensor Fabrication 27
4.2. Experimental Techniques 28
4.2.1. Basic Material Characterization 28
4.2.2. Gas Mixing 29
4.2.3. DC Resistance Measurements 30
4.2.4. Catalytic Conversion Measurements 31
4.2.5. Diffuse Reflectance Infrared Fourier-Transform Spectroscopy 31
4.2.6. UV/vis Diffuse Reflectance Spectroscopy 32
4.2.7. X-Ray Absorption Spectroscopy 33
5. The Gas Reception Mechanism of Pristine Tin Dioxide 34
5.1. Basic Characterization of undoped SnO_2 34
5.2. Identification of the Reactive Oxygen Species on pristine SnO_2 37
5.2.1. Operando DRIFTS investigation on the reactive oxygen species 38

5.2.2. Operando UV/vis-DRS measurements 45
5.2.3. Proposed model for the gas reception mechanism on pristine SnO_2 46
5.3. Surface Chemistry of Water Vapour and Hydroxyl Groups 49
5.3.1. DRIFTS study on the temperature dependence of water adsorption 49
5.3.2. Proposed model for the interaction of water with the SnO_2 surface 55
5.3.3. Electrical impact of the different adsorbed water species 57
5.3.4. Conclusions on the interaction of water vapour with the SnO_2 surface 60
6. The Impact of Platinum on the Gas Sensing Mechanism 61
6.1. Structure of the Platinum Loading 62
6.2. Gas Sensing Performance and Catalytic Activity of Pt-doped SnO_2 67
6.3. Impact on gas reception 69
6.4. Impact on transduction 73
6.5. Summary of the changes in gas reception and transduction 75
7. Summary 77
8. Outlook 79
9. References 80
10. Appendix 90
11. Publications 101
12. Curriculum Vitae 102
13. Academic Teachers 103
14. Acknowledgements 104

II. List of symbols

A……absorbance

a, b, c……lattice parameters (in case of crystal structures)

A_{1g}……Raman-active vibrational mode

A_{2g}……optically inactive vibrational mode

A_{2u}……IR-active vibrational mode

b……sensitivity

B_{1g}……Raman-active vibrational mode

B_{2g}……Raman-active vibrational mode

B_{1u}……optically inactive vibrational mode

c……concentration

c_0……speed of light

$C_{CO,measured}$……measured CO concentration (sample)

$C_{CO,reference}$……reference CO concentration (blank measurement)

$CC_{\%}$……(relative) catalytic conversion

Γ……irreducible representation of the optical modes

E……energy

e……elementary charge of an electron

E_1, E_2, E_3……energy levels of a free gas

$E_{1,surf}$, $E_{2,surf}$, $E_{3,surf}$……energy levels of a gas adsorbed at the surface

ΔE_a……activation energy

$E_{A,\ surf}$……surface acceptor state

E_C……conduction band edge

E_D……energy of a donor level

E_F……Fermi energy

E_g……Raman-active vibrational mode

E_{gap}……energy of the band gap

E_{pot}……potential energy

E_u……IR-active vibrational mode

E_V……valence band edge

E_{vac}……vacuum level

eV_s……energy of the surface band bending

F_j……backscattering amplitude

h……Planck constant

ΔH_{chem}……chemisorption enthalpy

ΔH_{phys}……physisorption enthalpy

I……current

I_0……Intensity of IR radiation recorded of a sensor in carrier gas atmosphere

I_{gas}……Intensity of IR radiation recorded of a sensor during the exposure to a target gas

I_{Ref}……Intensity of UV/vis radiation recorded of a reference material coated sensor

I_{Sample}……Intensity of UV/vis radiation recorded of sensor

k……wave vector

k_{ads}……reaction rate constant of adsorption

k_B……Boltzmann constant

k_{des}……reaction rate constant of desorption

k_f……force constant

k_{react}……reaction rate constant of reaction (e.g. oxidation of CO)

λ(k)……mean free path of a photo electron

M1 to M6……mirrors (diffuse reflectance optic)

m_e……mass of an electron

μ……reduced mass

μ(E)……absorption coefficient

n_b……concentration of electrons in the bulk

N_j……coordination number

n_s……concentration of electrons at the surface

ν……wavelength

$\tilde{\nu}$……wavenumber

R……resistance

R%……(relative) reflectance

R_0……resistance in the reference condition (pure carrier gas)

R_{gas}……resistance during test gas exposure

r, r_j……interatomic distance

R_{ref}……resistance of the reference resistor

R_{sens}……resistance of the sensing layer

S……sensor signal

S_0……amplitude reduction factor

σ_j……Debye-Waller factor

T……temperature

U……voltage

U_{ref}……potential prop over a reference resistor

U_{sens}……potential prop over the sensing layer

V_s……surface potential

ΔV_s……change of the surface potential

Φ……work function

$\varphi_{ij}(k)$……phase shift

χ……electron affinity

$\chi(E)$……EXAFS function

z……distance

III. List of abbreviations

% r.h. ……..percent relative humidity

AC……..Alternating Current

CCD……..Charge Coupled Device

DC……Direct Current

DCR……DC Resistance

DESY……...Deutsches Elektronen Synchrontron (Hamburg, Germany)

DRIFTS……Diffuse Reflectance Infrared Fourier-Transform Spectroscopy

DRS……..Diffuse Reflectance Spectroscopy

EPR……Electron Paramagnetic Resonance

ESRF……European Synchrotron Radiation Facility (Grenoble, France)

EXAFS……Extended X-ray Absorption Fine Structure

FT……..Fourier-transform or Fourier-transformed

GMS……Gas Mixing System

HAADF……...High-Angle Annular Dark Field

HERFD……High Energy Resolved Fluorescence Detection

ICIQ……..Institut Català d'Investigació Química (Tarragona, Spain)

ICP……..Inductively Coupled Plasma

ICSD……..Inorganic Crystal Structure Database

IR……..Infrared

KIT……..Karlsruhe Institute of Technology (Karlsruhe, Germany)

KNMF……...Karlsruhe Nano Micro Facility (KIT, Karlsruhe, Germany)

MFC……..Mass Flow Controller

OES……Optical Emission Spectrometry

PETRA III……...Positron-Elektron-Tandem-Ring-Anlage III (synchrotron light source at DESY)

SEM……...Scanning Electron Microscopy

STEM……..Scanning Transmission Electron Microscopy

SMOX……Semiconducting Metal Oxides

TEM……Transmission Electron Microscopy

TPD……..Temperature Programmed Desorption

TPR……Temperature Programmed Reduction

UPS……..UV photoelectron spectroscopy

UV……..Ultra Violet

vol%.....volume fraction

vis…….visible

wt%.....mass fraction

XANES…….X-ray Absorption Near Edge Structure

XAS…….X-ray Absorption Spectroscopy

XRD……..X-ray Diffraction

1. Introduction and Motivation

Gas sensors based on semiconducting metal oxides (SMOX) are cost-efficient and reliable devices used to detect a large variety of gases and volatile compounds. Their application ranges from industrial and safety applications to health and comfort [1]–[3]. Recent progress in the miniaturization of SMOX-based gas sensors drastically decreased the size, production costs and energy consumption, thus making gas sensors available for integration in consumer electronics and large-scale applications [4]. Sensors in general are considered to be an emerging technology for the Internet of Things. Gas sensors specifically are capable of providing chemical information based on traces of gases or volatile compounds [5]. But still, the major drawbacks of today's SMOX-based gas sensors are the low selectivity and strong cross interference as well as the still high operation temperature. The knowledge-based design of new sensing materials, which overcome these drawbacks, requires a detailed understanding of structure-function-relationships of gas sensing materials. However, identifying the relation of structure and function is quite challenging, solely because of the complexity of the gas sensing process itself and the large number of SMOX-based sensing materials [6]. For SnO_2, the most widely studied SMOX used for gas sensors [7], the impact of the preparation route, as well as the selection and introduction of noble metal additives, are reported to have a strong influence on material properties and gas sensing performance [8]–[11]. The essential question, however, is how to get insights into the fundamental processes of gas sensing. Early research one in order to understand the gas sensing process was based on experiments done on uniform single crystal surfaces, in ultrahigh vacuum conditions [12]–[14], i.e. there are tremendous gaps, in terms of materials, operation temperature and atmospheric conditions between the experiment and real-life applications. In order to overcome these gaps, the experimental techniques should be applicable to real gas sensor devices operated at 200-400 °C and at normal pressure, and also sensitive enough to detect changes, which are caused by traces of target gases in the ppm range or lower. Furthermore, the techniques should be applicable in real time and allow the simultaneous evaluation of the gas sensor performance, e.g. by continuous measuring the sensor resistance [6], [15]. Like in the case of other functional materials, such as catalysts or batteries, this is realized by so called in-situ and operando methods [16]–[18]. In-situ and operando methodology for gas sensor research (Figure 1) includes different spectroscopies as well as electrical measurement techniques [6], [15]. The number of in-situ and operando methods applied in gas sensor research has steadily increased during the last decades and has provided a more and more detailed picture of the fundamental processes on SMOX-based gas sensors. In case of pristine WO_3 and In_2O_3, which are after SnO_2 the most relevant SMOX for gas sensors, the gas reception mechanism of reducing gases was successfully revealed by applying operando spectroscopic

techniques. In both cases the detection of reducing gas involves lattice oxygen, i.e. the partial reduction of the materials. But despite all efforts, the role of surface oxygen species on SnO_2 and the interaction gases are still matter of ongoing discussions [19]. Also for noble metal loaded SMOX materials the identification of structure-function-relationships advanced due to extensive operando studies. Especially in case of homogeneously doped SnO_2, a series of works revealed the chemical and electrical effects of noble metal ions incorporated in the SnO_2 lattice [20]–[23]. In case of an inhomogeneous dispersion of the noble metals, the reports in literature are limited to Au-loaded SnO_2, which is an exception compared to other dopants, since Au is always present in a metallic state and does not influence the electronic properties of the supporting SnO_2 [24], [25].

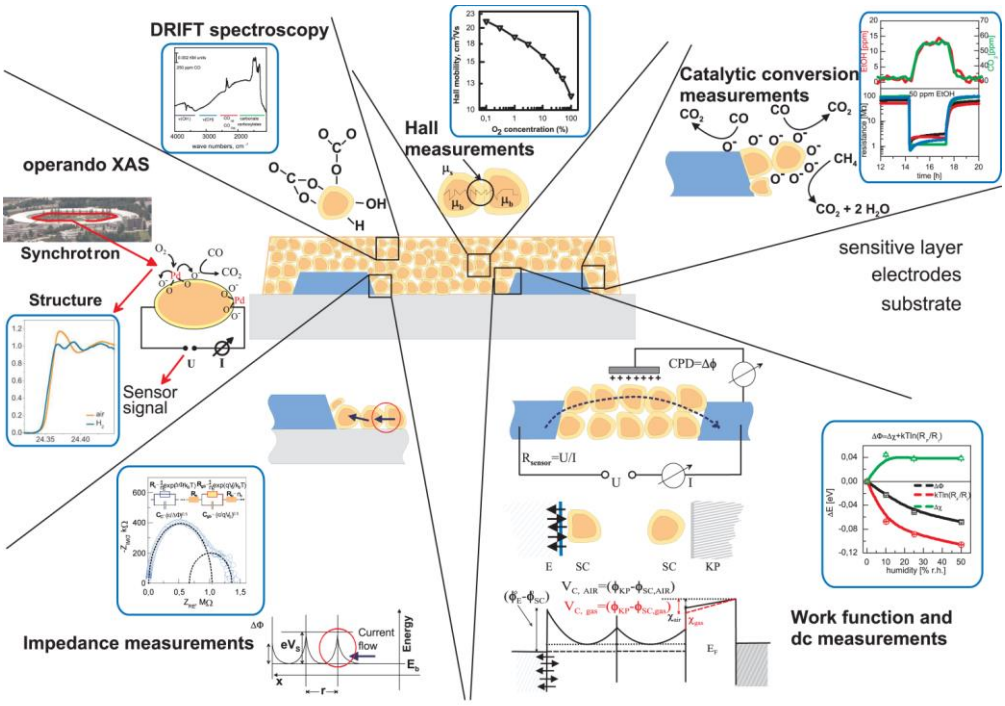

Figure 1. Overview of the operando techniques used by the gas sensor research group at the University of Tübingen. The measurements at synchrotron light sources are done in cooperation with the Karlsruhe Institute of Technology (KIT). The figure is based on [6], [26].

This work investigates the gas reception of undoped, i.e. pristine, and Pt-doped SnO_2 gas sensing materials. The aim of the investigations on undoped SnO_2 is to identify the reactive oxygen species on SnO_2 and its interaction with reducing gases, as well as with water vapour, which is the omnipresent interfering gas in ambient conditions. In the case of Pt-doped SnO_2, the measurements will enable the determination of the structure of the Pt loadings, especially in operation conditions, the impact of Pt on the surface chemistry and reactivity of SnO_2 and the possible electronic effect related to the found Pt structures. Combining these results will provide a conclusive model which links the structure of the Pt loading with its impact on gas sensing.

2. Basic Aspects of Gas Sensing with Tin Dioxide

2.1. Definitions for Chemical Sensors

In general sensors can be divided into physical and chemical sensors based on the measured property of a system, which can be either physical or chemical. The International Union of Pure and Applied Chemistry defines a chemical sensor as "a device that transforms chemical information (…) into an analytically useful signals." [27]. The sensor as such does not include sample, single or data processing, and has two basic functional units: the receptor and the transducer. The receptor function transforms the chemical information into a form of energy that is measured by the transducer. Accordingly, the transducer function transforms the energy, created by the chemical information, into a useful analytical signal [27]. The above described fundamental principle of a chemical sensor is illustrated in Figure 2.

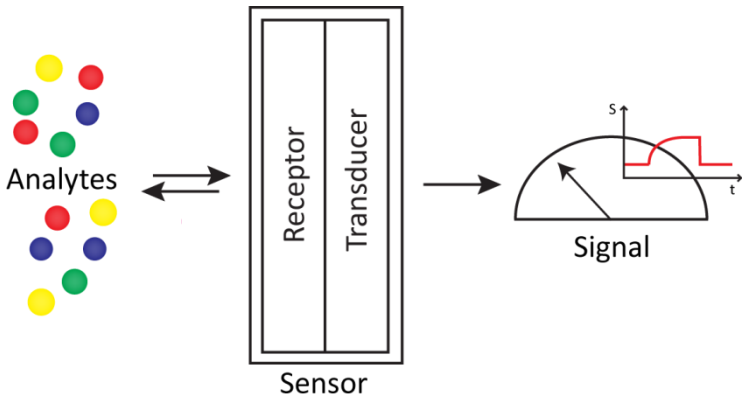

Figure 2. Fundamental principle of a chemical sensor with the two basic functions reception and transduction.

Based on the transducer's working principle chemical sensors can be classified into optical, electrochemical, electrical, mass sensitive, magnetic or thermometric devices. According to this classification SMOX-based gas sensors belong to the group electrical sensors. Additionally sensors may also be grouped by the determined analytes or the methods used for measuring an effect [27]. In addition to the classification of chemical sensors as such, several characteristics of a chemical sensors are relevant to describe the performance of these devices. Although this is only a selection the terms signal, sensitivity, selectivity, specificity and stability will be briefly defined. In case of SMOX-based gas sensors the readout is typically the resistance of the sensitive layer R and the (steady-state) sensor signal S is either the ratio, difference or a combination of both of the sensor readout in a reference condition (R_0), e.g. absence of the analyte, and the presence of a certain analyte concentration (R_{gas}) [28]:

$$S_1 = \Delta R = R_0 - R_{gas} \qquad \textbf{Equation 1}$$

$$S_2 = \frac{R_0}{R_{gas}} \qquad \textbf{Equation 2}$$

$$S_3 = \frac{\Delta R}{R_0} = \frac{S_1}{R_0} = S_2 - 1$$ **Equation 3**

The Sensitivity b describes the relationship between changes in the chemical stimulus, i.e. analyte concentration c, and the obtained signal, or short the slope of a calibration curve [29], [30]:

$$b = \left.\frac{dS}{dc}\right|_c$$ **Equation 4**

Selectivity is an expression for the ability of a sensor to respond to a certain group of analytes in an analyte mixture, while specificity is the ability of a sensor to respond to one analyte in an analyte mixture [30]. The (long-term) stability of a sensor is its ability to maintain its performance, like readout values under a certain condition (e.g. baseline stability), signal, sensitivity and/or selectivity/specificity, for a certain timespan [30].

2.2. Properties of Tin Dioxide

2.2.1. Crystal Structure

Tin dioxide, also referred as stannic oxide, crystallizes in the tetragonal rutile structure (see Figure 3), named after the mineral Cassiterite. The unit cell possesses a space-group symmetry of $P4_2/mnm$ (point group D_{4h}^{14}) and the lattice constants a = b = 4.7374 Å and c = 3.1864 Å [31], [32]. For stoichiometric SnO_2 a unit cell consists of six atoms: two six-fold coordinated tin and four three-fold coordinated oxygen ions with the oxidation states +4 (Sn^{4+}) and -2 (O^{2-}), respectively [31]. The cations (Sn^{4+}) are located at the corners (0,0,0) and the centre (½, ½, ½) of the unit cell, the anions (O^{2-}) at ±(x,x,0) and ±(½+x, ½-x,½) with x=0.307 [33].

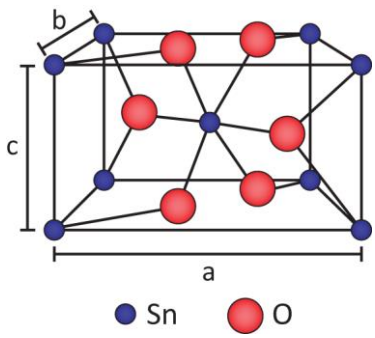

Figure 3: Unit cell of SnO_2 (rutile structure), as adapted from [32]. Each tin atom (blue) is coordinated by six oxygen atoms (red). Each oxygen atom is coordinated by three tin atoms.

2.2.2. Optical Active Vibrational Modes

The irreducible representation of the optical modes of the Cassiterite unit cell is [34]:

$$\Gamma = A_{1g} + A_{2g} + B_{1g} + B_{2g} + E_g + A_{2u} + 2B_{1u} + 3E_u \qquad \textbf{Equation 5}$$

The A_{2u} and the triply degenerated E_u modes are IR active; the non-degenerated A_{1g}, B_{1g}, B_{2g} and doubly degenerated E_g modes are Raman active. The remaining A_{2g} and B_{1u} modes are silent (optically inactive) [34]–[39]. In the IR active modes the Sn^{4+} and O^{2-} ions vibrate along the c-axis (A_{2u} mode) or in the plane perpendicular to the c-axis (E_u mode), see Figure 4 a, b. In the Raman active modes only the O^{2-} ions vibrate, while the Sn^{4+} atoms rest. The A_{1g}, B_{1g} and B_{2g} modes vibrate in the plane perpendicular to the c-axis (Figure 4 c-e), the doubly degenerated E_g mode vibrates in the direction of the c-axis (Figure 4 e, f) [34]–[36].

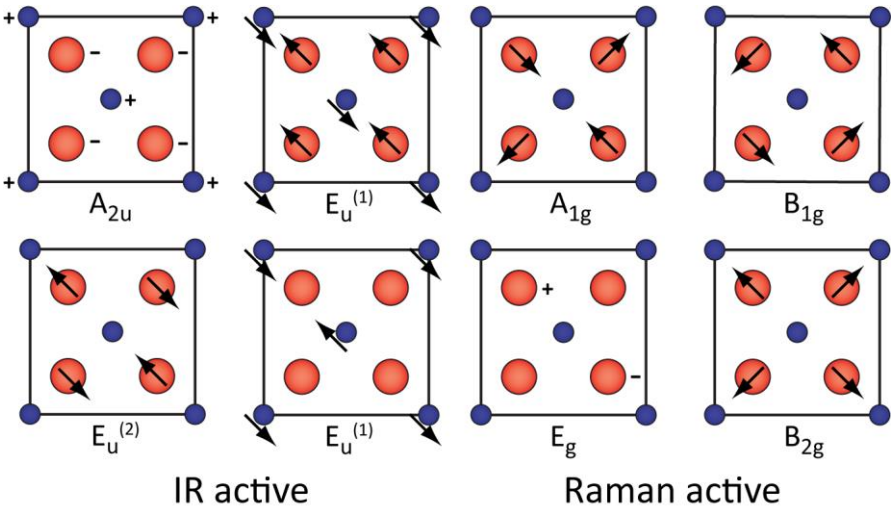

Figure 4: Optical active vibrational modes of Rutile [35], [36]. The 2D representation is view along the c axis of the unit cell with Sn atoms (blue) and O atoms (red). Movements of the atoms in the plane are indicated by arrows, movements along the c axis by plus and minus.

Table 1. IR and Raman active vibrational modes found for single crystalline SnO_2.

Mode	Active in	Wavenumber [cm^{-1}]		Reference
		calculated	experimental	
B_{1g}	Raman	100	--	[37]
E_u TO	IR	236	244; 243	[40]; [41]
E_u LO	IR	268	276; 273	[40]; [41]
E_u TO	IR	297	293; 284	[40]; [41]
E_u LO	IR	377	366; 368	[40]; [41]
E_g	Raman	441	476; 475	[40]; [37]
A_{2u} TO	IR	512	477; 465	[40]; [41]
A_{1g}	Raman	646	638; 634	[40]; [37]
E_u TO	IR	651	618; 605	[40]; [41]
A_{2u} LO	IR	687	705; 704	[40]; [41]
E_u LO	IR	750	770; 757	[40]; [41]
B_{2g}	Raman	752	782; 776	[40]; [37]
E_u x E_u	IR	1270	1290 - 1220	[42]
			1320 - 1260	[40]
E_u x E_u	IR	1405	1390; 1370	[40]; [42]
A_{2u} x A_{2u}	IR	1414	1460 - 1370	[42]
			1485 -1400	[40]
B_{2g} x E_u	IR	1540	1560; 1520	[40]; [42]

2.2.3. Electronic Properties

Non-stoichiometric SnO_2 is a wide-bandgap semiconductor with n-type behaviour caused by electronic donor states related to oxygen vacancies. The valance and conduction band are separated by a direct band gap of 3.6 eV [31]. For single crystalline SnO_2, experimental findings show a band gap of 3.5969 eV or 3.5971 eV, obtained by Zeeman effect or UV-vis absorption measurements at 1.8 K, respectively [43]. The valence band of SnO_2 can be divided into three different energy regions. The valence band maximum (0 to -2 eV) has a dominant O 2p character. The centre region (-2 to -5 eV) is the result of the hybridization of Sn 5p and O 2p orbitals and at the lower region of the valance band (-5 to -9 eV) the Sn 5s states have a larger share to the hybridization with the O 2p states than the Sn 5p states [44], [45]. The conduction band has only a small contribution of O 2p orbitals, its bottom (3.6 to 8 eV) has a dominant Sn 5s character, and above (8 to 12) eV a dominant Sn 5p character [44]. The composition of the valance and conduction band is illustrated in Figure 5a. The n-type semiconductor properties arise from oxygen vacancies which create donor states in the band gap below the conduction band. Combined Hall mobility and conductivity measurements between 80 and 325 K identify two donor levels located 30-34 meV and 140-150 meV below the conduction band (see Figure 5b) [46].

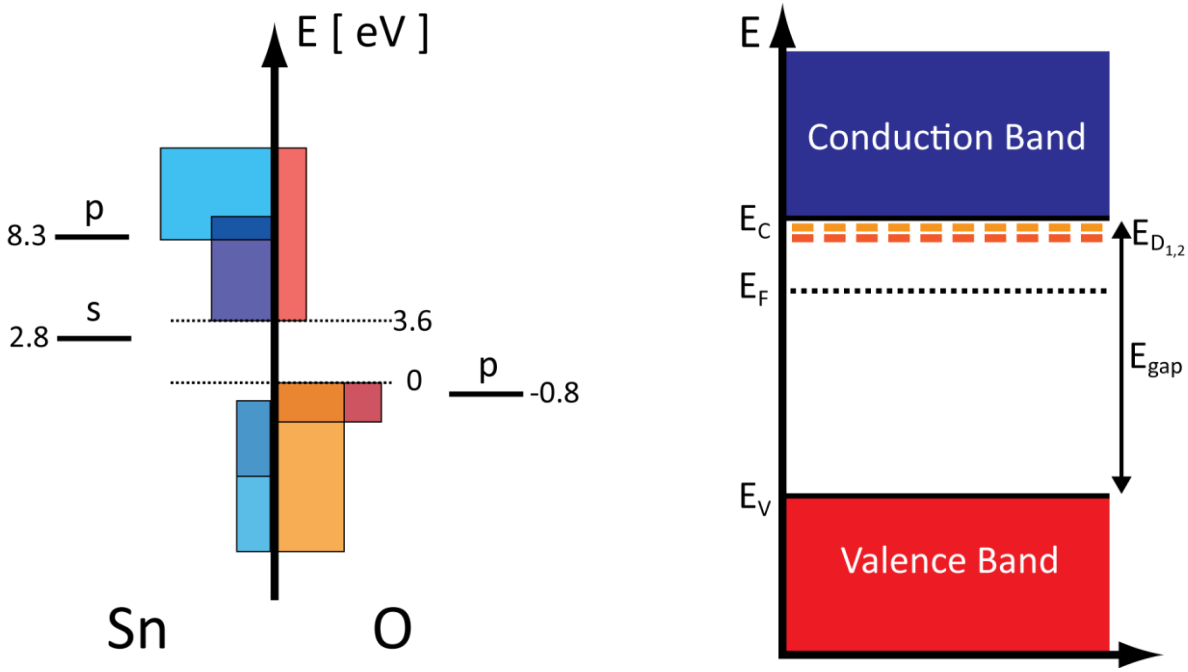

Figure 5. Simplified representation of the density of states of the valance and conduction band of bulk SnO_2 (a) and schematic representation of the SnO_2 band diagram including donor states below the conduction band (b). The left figure is adapted from [44].

2.2.4. Single Crystal Surfaces

Single crystalline SnO_2 exposes a series of different faces whereof the {110} and the {101} surfaces are the predominant ones. Thus the (110) and (101) surfaces of SnO_2 are most widely studied by

surface science methods and theoretical calculations, as reviewed in the works of M. Batzill and U. Diebold [31], [47], which provide the basis for the following discussion. Stoichiometric surfaces are obtained by truncating the bulk crystal along the crystal planes, cutting the same number of bonds direct from a tin to an oxygen atom and vice versa. In case of stoichiometric surfaces all atoms maintain their oxidation state [31]. The stoichiometric (110) surface (Figure 6a) is terminated by two different types of oxygen atoms which are threefold or twofold coordinated and are referred as in-plane or bridging oxygen atoms, respectively. An additional type of oxygen is considered to be placed atop a Sn atom in the (110) surface plane. The notation of the different oxygen species on the (110) surface are shown in Supporting Figure 1. By removing the bridging oxygen the reduced (110) surface is obtained (Figure 6b), due to the reduction some tin atoms are reduced to Sn^{2+}. However, this structure for the reduced (110) surface is expected to have a high surface energy. Lower surface energies may be obtained by additionally removing 50 % of the in-plane oxygen atoms [31]. The resulting surface structure is shown in Figure 6c. For the (101) surface both, stoichiometric and reduced, terminations are stable and their occurrence depends on the equilibrium with the gas phase. The stoichiometric (101) surface is terminated by twofold coordinated oxygen atoms and five-fold terminated tin atoms (Figure 6d). The reduced (101) surface is terminated by three-fold coordinated tin atoms, as shown in Figure 6e, all present in the Sn^{2+} state [31].

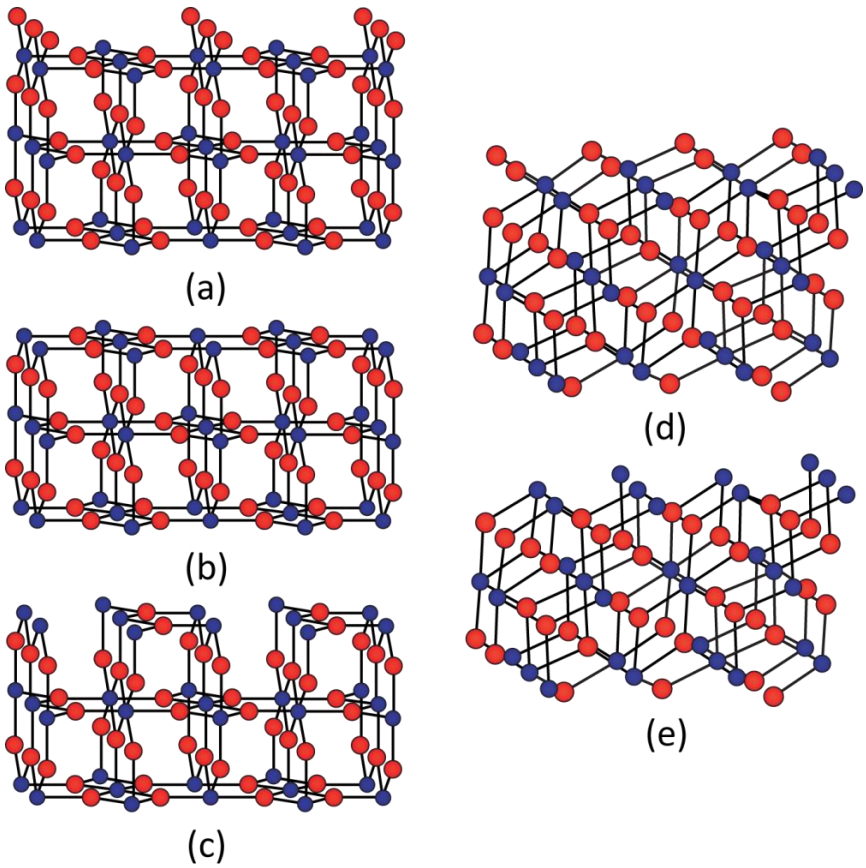

Figure 6. Ball-stick models of (110) and (101) SnO_2 surfaces, a-c and d-e respectively. A detailed description of the stoichiometric (a and d) and reduced (b, c and e) surfaces is given in the text. The figures are adapted from [31].

It is important to note that single crystal surfaces may already exhibit various surface reconstructions and multidimensional defects and thus may differ from the idealized ball-stick models shown in Figure 6 [31]. Nonetheless theoretical and experimental works performed on such idealized surfaces provide important insights in order to understand surfaces on an atomistic level.

2.2.5. Adsorption and Adsorbed Surface Species on SnO_2

The reception of gases is one of the fundamental processes of SMOX-based gas sensors and is strongly related to the formation of adsorbates, their reactions and their effect on the SMOX's surface. The following paragraphs describe processes relevant to the adsorption of molecules on surfaces and surface species found on SnO_2, which are considered to be relevant to the gas sensing process.

In general molecules can be adsorbed on a surface in two different ways. In the case of physisorption the interaction between the adsorbate and the surface is limited to dispersion forces, e.g. van der Waals interactions. In the case of chemisorption the adsorption involves the formation of chemical bonds between the adsorbate and adsorbent [48], [49].

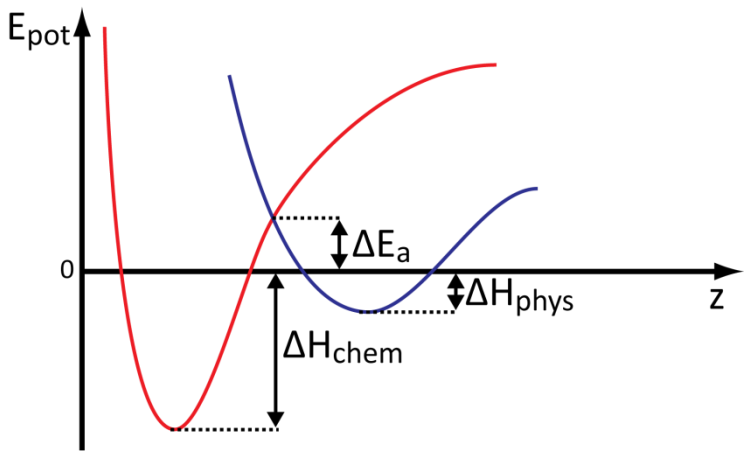

Figure 7. Potential energy E_{pot} of an activated adsorption as function of the distance z. The Lennard-Jones potential of physisorption and chemisorption are shown in blue or red, respectively. Figure is adapted from [49].

The Lennard-Jones diagrams shown in Figure 7 highlights the differences of both adsorption processes. Physisorption takes place at longer distances from the surface and the adsorbate is only weakly bound to the surface, as it can be seen from the lower physisorption enthalpy ΔH_{phys}. Physisorption does not cause changes of the electronic structure or dissociation of the adsorbed molecule. Chemisorption presents much higher enthalpies (ΔH_{chem}) than physisorption and the adsorbate is bound closer to the surface. Due to the formation of chemical bonds the electronic structure of the adsorbate and the surface are altered. Chemisorption may involve the dissociation of the adsorbed molecule. Generally, but not in all cases, the physisorbed and chemisorbed states are separated by an energy barrier, which corresponds to the activation energy caused by the

dissociation of the molecule or the energy required to adjust bonds of the adsorbed molecule [48], [49]. If a chemisorbed species forms separate charged species the process is termed ionosorption [50]. Chemisorption alters the bonds, i.e. electronic structure, of both, the adsorbed molecule and the solid [48], [50]. These changes are best understood by looking at the energy bands of the solid, the energy levels of the adsorbed molecule and the formation of surface states, which are a result of chemisorption. Therefore, two examples will be discussed: chemisorption of gas molecule on a transition metal and on a n-type semiconductor.

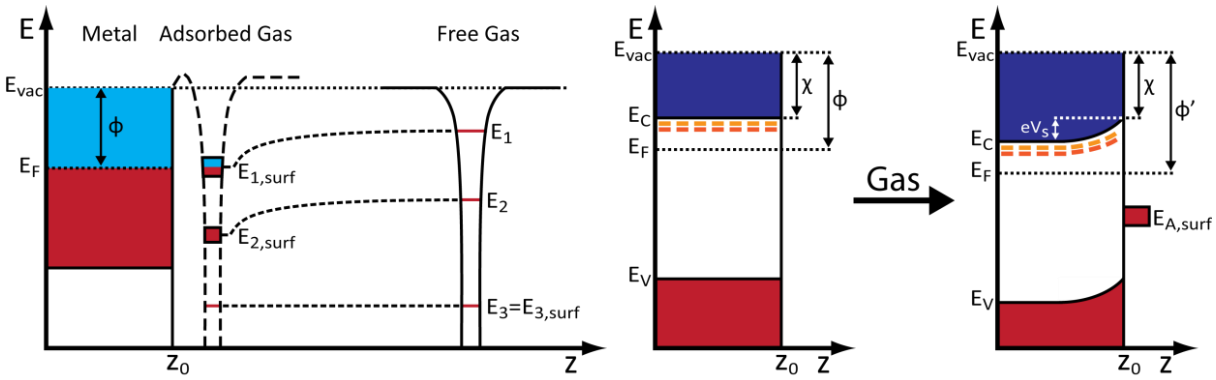

Figure 8. Weak chemisorption of a gas molecule on a metal (left) and ionosorption of a gas molecule on a n-type semiconductor (right). The left and right figure are adapted from [48] and [14], respectively.

As a gas molecule approaches the surface the initially narrow electronic states are broadened and lowered in energy by interaction with electronic sates of the solid (E_1 and E_2 in Figure 8, left). However, if there is no corresponding energy band in the solid the electronic states of the gas molecule are not changed (E_3 in Figure 8, left). The occupation of the broadened adsorbate orbitals depends of their position with respect to the Fermi level of the solid, i.e. the adsorbate orbitals are filled, partially filled or not filled (see Figure 8, left) [48]. These new electronic surface states act as acceptor states (below the Fermi level) or donor states (above the Fermi level) [12], [14], [51], [52]. In case of metals, due to screening of the high free charge carrier density, the effect on the energy bands is small and thus negligible [51]. However, in case of a semiconductor the situation is different. The presence of a surface state, either an acceptor or a donor state, causes an electron transfer from the solid to the adsorbate. The right part of Figure 8 shows the adsorption of a gas, e.g. O_2, creating a surface acceptor state $E_{A,surf}$. The adsorbate is charged negatively, while in the solid an electron depleted, i.e. positive, space charge layer is formed. The formation of this depletion layer causes the energy bands at the surface to bend upwards with respect to the Fermi level. The band bending induced by the depletion layer has an impact on the solids properties, like e.g. the work function [12], [14], [51], [52]. In case of a donor state the opposite effect is observed, namely a downwards band bending and the formation of an accumulation layer [12], [51], [53].

2.2.5.1. Adsorption of Oxygen

The surface oxygen species of SnO_2 are considered to be essential for its catalytic and gas sensitive properties and during the last decades the reactive oxygen species was discussed controversially. Molecular species, namely superoxo (O_2^-) and peroxo (O_2^{2-}) species, as well as atomic species, namely an atomic radical (O^-) and closed valence shell oxide (O^{2-} or O_O) were proposed to be present on the SnO_2 surface [19], [52]. Considering all species as intermediates of the transformation of atmospheric oxygen to lattice oxygen (Reaction 1) the following cascade of reactions can be proposed, assuming that only the transfer of one electron per reaction step and only the formation of neutral, mono and doubly negatively charged oxygen species. The reaction steps are simplified by neglecting the role of surface sites and oxygen vacancies. In a first step, atmospheric oxygen is adsorbed as an uncharged molecular species (Reaction 2), which traps electrons form the solid first forming a superoxide (Reaction 3), followed by the formation of a peroxide (Reaction 4). In a next step the molecular oxygen dissociates into two atomic species (Reaction 5), which, by abstracting additional electrons, will settle as lattice oxygen on the surface layer of the metal oxide (Reaction 6) [12], [19], [54], [55].

$$\frac{1}{2}O_{2,gas} + V_O^{2+} + 2e^- \leftrightharpoons O_O \qquad \textbf{Reaction 1}$$

$$O_{2,gas} \leftrightharpoons O_{2,ads} \qquad \textbf{Reaction 2}$$

$$O_{2,ads} + e^- \leftrightharpoons O_{2,ads}^- \qquad \textbf{Reaction 3}$$

$$O_{2,ads}^- + e^- \leftrightharpoons O_{2,ads}^{2-} \qquad \textbf{Reaction 4}$$

$$O_{2,ads}^{2-} \leftrightharpoons 2O_{ads}^- \qquad \textbf{Reaction 5}$$

$$O_{ads}^- + e^- \leftrightharpoons O_{ads}^{2-} \leftrightharpoons O_O \qquad \textbf{Reaction 6}$$

Considering theoretical calculations for the adsorption of oxygen on SnO_2 (110) and (101) surfaces the superoxide species and lattice oxygen, namely twofold coordinated bridging oxygen, can be assumed to be the most stable molecular and atomic species, respectively [56], [57]. Experimental evidence for the different oxygen species is mainly based on three techniques: Temperature Programmed Desorption (TPD), Electron Paramagnetic Resonance (EPR) or IR spectroscopy. TPD studies report three main desorption features, corresponding to molecular oxygen, atomic oxygen and the decomposition of the material, respectively [58], [59]. The appearance of these oxygen species strongly depends on the pre-treatment of the sample. The first desorption peak, found below 200 °C, was identified by EPR spectroscopy as singly charged molecular oxygen (superoxide) [59]. For reduced SnO_2 samples the existence of the superoxide is verified by IR spectroscopy [60], [61].

The second desorption peak - at 400-600 °C [59] or 500-700 °C [58] – is assigned to atomic oxygen [59]. Unlike the molecular oxygen species, the atomic ones are not observable by IR spectroscopy. The only report claiming to have observed paramagnetic atomic radical species by EPR spectroscopy [62], is discussed controversially [19]. Above 600-700 °C the metal oxide is decomposed [58], [59]. Lattice oxygen of the metal oxide will be present at temperatures relevant to gas sensing, but its reactivity may depend on the temperature and differ for lattice oxygen at the surface and in the bulk. According to $^{16}O_2$-$^{18}O_2$ exchanges experiments on pristine SnO_2, bulk oxygen is exchanged above 425 °C [63].

2.2.5.2. Adsorption of Water

On SnO_2 surfaces water is present as molecular species or as hydroxyl groups (see Supporting Figure 2). The molecular adsorption includes physisorbed (Reaction 7) and associative adsorbed/H-bonded water molecules (Reaction 8). In case of dissociative adsorption the formation of hydroxyl groups requires one additional oxygen atom to balance the stoichiometry of the reaction, e.g. as proposed by S. R. Morrison for dissociative adsorption of water of oxide surfaces (Reaction 9) [50]. Various experimental works demonstrate that molecular water is observed up to 200 °C, while hydroxyl groups, i.e. dissociative adsorbed water, are present up to above 500 °C, but strongly decrease around 300-400°C [59], [64]–[67]. The TPD profile of water adsorbed on SnO_2 shows two desorption peaks centered at 100 and 400 °C. The low temperature peak corresponds to desorption of molecular water, which is completed around 200 to 250 °C. The recombination of surface hydroxyl groups starting at 250 to 300 °C causes the second desorption peak [59], [64]. The TPD studies are in good agreement with IR spectroscopic studies observing the desorption of physisorbed water up to 150 °C and a strong decrease of surface hydroxyls above 200 °C [66], [67].

$$H_2O_{gas} \leftrightharpoons H_2O_{phys}$$ **Reaction 7**

$$H_2O_{gas} + O_O \leftrightharpoons HO \cdots H \cdots O_O$$ **Reaction 8**

$$H_2O_{gas} + O_O + S \leftrightharpoons (OH)_O + (OH)_S$$ **Reaction 9**

There are several proposed models for the electrical effect of water vapour based on dissociative adsorption. The above shown reactions are simplistic, as the nature of the surface and the attachment of the oxygen and hydroxyl species on the surface are disregarded. In general water has a reducing effect on SnO_2, which is explained by different mechanisms. The first of which includes the formation of an oxygen vacancy and two hydroxyl groups bound to Sn, so called terminal hydroxyl groups (see Supporting Figure 2). The overall reducing effect is due to the ionization of the oxygen vacancy (Reaction 10) [12]. The second reaction results in the formation of one terminal hydroxyl group and one bound to several Sn (Reaction 11), a so called rooted hydroxyl group (see Supporting

Figure 2). Rooted hydroxyl groups are also considered to be donors [12]. An additional reaction of water vapour with the SnO_2 surface is the formation of two rooted hydroxyl groups based on the reaction of surface oxygen, a surface oxygen vacancy and a water molecule (Reaction 12) [68]. This reaction yields hydroxyl groups, without having an effect on the conductivity of the material.

$$H_2O_{gas} + O_O + 2Sn_{Sn} \leftrightharpoons 2\left(Sn_{Sn}^{\delta+} - OH^{\delta-}\right) + V_O^{2+} + 2e^- \qquad \textbf{Reaction 10}$$

$$H_2O_{gas} + O_O + Sn_{Sn} \leftrightharpoons \left(Sn_{Sn}^{\delta+} - OH^{\delta-}\right) + (OH)_O^+ + e^- \qquad \textbf{Reaction 11}$$

$$H_2O_{gas} + V_O^{2+} + O_O + Sn_{Sn} \leftrightharpoons 2(OH)_O^+ \qquad \textbf{Reaction 12}$$

Besides models based on dissociative adsorption, the reducing effect of water vapour is also explained based on the associative adsorption of water. Water molecules either interact with acid or basic surface species influencing their electronic states [50], [69] or hinder oxygen adsorption, e.g. by competing with adsorbed (molecular) oxygen species for the same surface sites [69], [70]. Theoretical calculations for stoichiometric, reduced and oxidized SnO_2 (110) surfaces were used to evaluate the stable associative and dissociated adsorbates and their electronic effects [71]: Associative adsorption (Reaction 8) causes electron donation from water molecules to the SnO_2 surface; accordingly water molecules act as weak electron donors. However, during dissociative adsorption an electron donation from surface/bridging oxygen to the terminal hydroxyl groups was found. The charge transfer from the surface oxygen to the formed terminal hydroxyl group compensates the initial charge transfer related to associative adsorption, i.e. in sum dissociative adsorption would not change the resistance. Based on this model the reducing effect of water vapour is either caused by predominant associative adsorption or the formation of oxygen vacancies. However, this theoretical work may not cover the full scope of processes occurring on poly crystalline SnO_2, which offers various different facets and defects. Furthermore, the theoretical calculations reveal, that the ratio between associative and dissociative adsorption is strongly influenced by the stoichiometry, i.e oxygen coverage, of the surface and the initial presence of dissociated water, i.e. hydroxyl groups [71]. The theoretical calculations are supported by experimental results of differently prepared (110) surfaces, which show the strong influence of surface stoichiometry on the dissociative water adsorption [72]. The same trends are, theoretically and experimentally, found for the (101) surface [73]. In summary, the experimental works show that the water related adsorbates depend strongly on temperature and surface composition; the theoretical calculations support that water adsorption is influenced by the nature of the surface, e.g. stoichiometry or existing hydroxyl groups, and furthermore indicate different electronic effects for associative and dissociative adsorbed water molecules.

2.2.5.3. Adsorption of Carbon Monoxide and Carbon Dioxide

Various IR spectroscopic studies report the formation of carbonate and carboxylate species upon CO or CO_2 exposure [66], [74]–[76]. Uni- and bidentate carbonates as well as carboxylates are reported for CO and CO_2 exposure over a large temperature range from room temperature up to 400 °C [66], [74], [76]. However, a strong influence of the sample pre-treatment and the material's calcination temperature on the appearance of carbonate and carboxylate species is reported [66], [74], [75]. Bicarbonate species are reported to be formed at room-temperature [76], but are not present at 200 °C or higher temperature [74]; a clear assignment of bicarbonates was found to be difficult, as the identification by deuteration failed [75]. Different reactions of CO or CO_2 with surface oxygen species are proposed for the formation of carbonate and carboxylate species [75]. Theoretical calculations for (110) surfaces indicate that carbonate species are formed by the reaction of CO with molecular oxygen adsorbed on an oxygen vacancy (Reaction 13), while carboxylates are formed by the reaction of CO with a lattice oxygen atom of a strongly reduced surface (Reaction 14) [56]. Similar findings were made for the (101) surface: Theoretical calculations suggest a carboxylate-like reaction intermediate for the reaction of CO with lattice oxygen (Reaction 14), which desorbs creating an oxygen vacancy (Reaction 15) [57]. However, for the formation of carbonates the calculations for the (101) surface propose a reaction of CO_2 with lattice oxygen (Reaction 16) [57].

$$CO_{gas} + O_{2,ads}^{\alpha-} + (2-\alpha)\cdot e^- \leftrightharpoons (CO_3)^{\alpha-} \qquad \textbf{Reaction 13}$$

$$CO_{gas} + O_O \leftrightharpoons (CO_2)_O \qquad \textbf{Reaction 14}$$

$$(CO_2)_O \leftrightharpoons CO_2 + V_O^{2+} + 2\cdot e^- \qquad \textbf{Reaction 15}$$

$$CO_{2,gas} + O_O \leftrightharpoons (CO_3)_O \qquad \textbf{Reaction 16}$$

The reversible adsorption of CO_2 as carbonates or decomposition of carbonates formed by a reaction with CO should not yield in significant changes in the electronic properties of the solid; while the decomposition of the carboxylates formed by CO result in the formation of an oxygen vacancy, which can donate electrons to the solid.

The formation of carbonyl species (Reaction 17) on pristine SnO_2 materials is only reported for CO adsorption at 120 K [77]. According to the theoretical calculations the electronic effects of CO adsorption are much smaller than the changes caused by the formation of an oxygen vacancy [56], [57].

$$CO_{gas} \leftrightharpoons CO_{ads} \qquad \textbf{Reaction 17}$$

The above discussed surface species are summarized in Figure 9. In case of surface oxygen, only species verified by experimental techniques are shown. It should be noted that, with few exceptions,

the experimental conditions – temperature, pressure, atmospheric composition and sample form – diverge strongly from the operation conditions of gas sensors. A more detailed summary with the assignment of the experimental techniques can be found in [52].

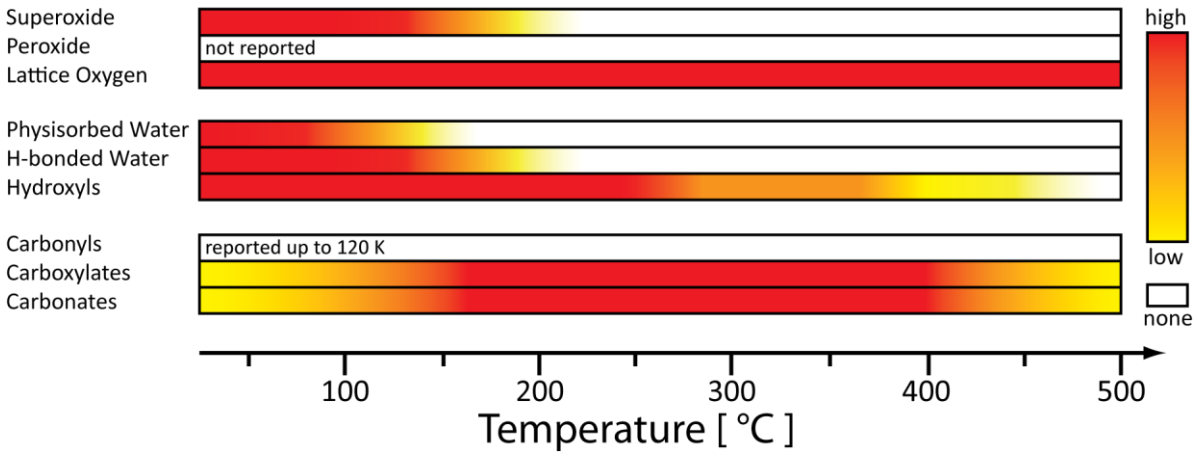

Figure 9. Surface species observed on SnO_2, by various experimental techniques. The appearance of the different species is indicated by the colour tone as shown on the scale on the right side of the figure. The figure is adapted from [52].

2.3. Working Principle of Tin Dioxide Based Gas Sensor

The resistance of the sensing layer determines the measured output and, as the resistance can be changed by the presence of reducing or oxidizing gases, the signal of resistive gas sensor based on SMOX [52], [78]–[80]. As for all chemical sensors, the sensing effect is based on the principle of reception and transduction. The reception of the analyte gases takes place by a chemical interaction with the SMOX. Such an interaction is either a chemisorption process whereupon the analyte gas adsorbs and desorbs as the same molecule or the reaction of the analyte gas with the another surface species [14]. The transduction of the changes at the SMOX surface is based on changes of the electronic properties of the SMOX or its surface which influence the charge transport within the sensing layer and thus the measured overall resistance [80].

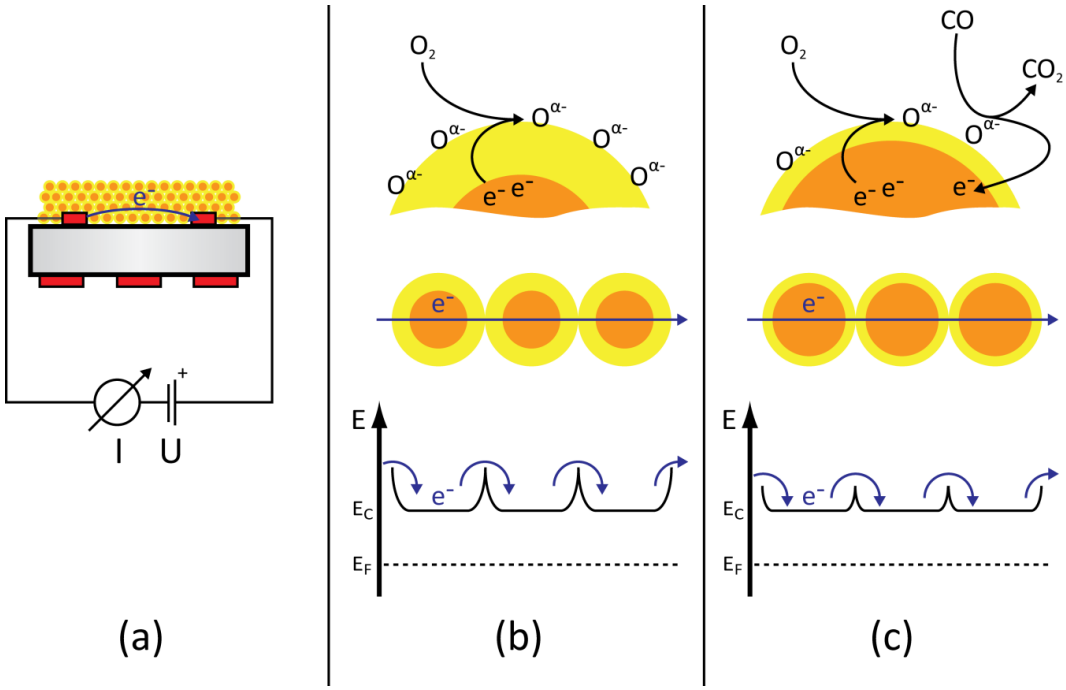

Figure 10. Schematic cross-section (a) and working principle (b and c) of a SMOX-based resistive gas sensor. The simplified surface chemistry is shown on top of b and c; the potential barriers, which limit the charge transport, at the bottom of b and c. The unaffected bulk region of the grains is shown in orange and the electron depleted layer in yellow.

In a typical SMOX-based resistive gas sensor consisting of a porous SMOX layer deposited on an insulating substrate with (measurement) electrodes on the frontside and a heater on the backside (see Figure 10a). The measured resistance is the sum of the resistances of grain-grain, grain-bulk and grain-electrode interfaces [52]. The limiting factor is the resistance at the grain-grain interfaces, which is determined by the charge carrier concentration and mobility at the surface of the grains. In the case of SnO_2, electrons act as the majority charge carriers. The mobility of the electrons is not changed during gas sensing [52], thus resistance depends solely on the surface concentration of electrons. In the absence of any intrinsic surface states or adsorbates the electron concentration at the surface equals the one in the bulk. This situation is referred as the flat band situation [80]. In the

presence of surface acceptor states, e.g. caused by ionosorption, a depletion layer is formed leading to an upwards band bending, resulting in back-to-back Schottky barriers at the grain-grain boundaries. This situation is shown in Figure 10b and c bottom. If the Schottky approximation is valid, i.e. all donors are fully ionized, the concentration of electrons n_s is described by the Boltzmann distribution [52], [81], [82]:

$$n_s = n_b \cdot exp\left(-\frac{eV_s}{k_B T}\right) \qquad \textbf{Equation 6}$$

Accordingly, the resistance of sensing layer will be proportional to the surface band bending eV_s:

$$R \propto exp\left(\frac{eV_s}{k_B T}\right) \qquad \textbf{Equation 7}$$

By combining

Equation **2** and Equation 7 the sensor signal can be described by the change of the surface band bending:

$$S = \frac{R_0}{R_{gas}} \propto \frac{exp\left(\frac{eV_{s,0}}{k_B T}\right)}{exp\left(\frac{eV_{s,gas}}{k_B T}\right)} = exp\left(\frac{e \cdot \Delta V_s}{k_B T}\right) \qquad \textbf{Equation 8}$$

For typical operation conditions – sensing layer heated 300 °C and low test gas concentrations (ppm) in dry air – the dominant surface adsorbate, which is responsible for the surface band bending , is assumed to be ionosorbed oxygen [52]. The surface concentration of the ionosorbed oxygen species depends on the partial pressure of oxygen and the presence (or partial pressure) of reducing gases [52], [80]. In the absence of reducing gases, oxygen will be ionosorbed (Reaction 18) at the surface resulting in an upwards band bending at the grain surfaces (Figure 10b).

$$\frac{1}{2}O_2 + S + \alpha \cdot e^- \underset{k_{des}}{\overset{k_{ads}}{\leftrightharpoons}} O_S^{\alpha-} \qquad \textbf{Reaction 18}$$

$$O_S^{\alpha-} + CO \xrightarrow{k_{react}} S + CO_2 + \alpha \cdot e^- \qquad \textbf{Reaction 19}$$

In the case of CO exposure, the ionosorbed oxygen species will react with CO forming CO_2 (Reaction 19), which desorbs as a neutral species releasing the trapped electrons to the solid and thus decrease the negative charge trapped at the surface. Consequently, the back-to-back Schottky barriers at the grain-grain boundaries are lowered and the resistance of the sensing layer decreases (Figure 10c).

The above described model links the atmospheric composition with the resistance of the sensing layer and represents the generally accepted working principle for SMOX-based gas sensors. However,

this model is to limited simple gases, like CO, in idealized conditions, i.e. no interfering gases like H_2O; for noble metal loaded SnO_2. More complex gases, e.g. organic compounds, or in the presence of interfering gases this sensing mechanism differs and requires more sophisticated models, taking in to account changes in the gas reception and/or transduction mechanisms.

2.4. Role of Noble Metal Loadings

The addition of noble metal loadings to SMOX is one of the most common methods to improve the sensitivity , selectivity and stability of SMOX-based gas sensors [2], [3], [83]–[85]. These noble metal loadings, or dopants, influence the reception and/or transduction of the sensing materials. Assuming that the noble metal loadings are present as a separate phase (inhomogeneous dispersion) two main sensitisation mechanisms are considered: A chemical sensitisation mechanism related to a spill-over of gases, thus referred to as a spill-over mechanism, and an electronical sensitisation mechanism which is based on the alignment of the Fermi levels of the SMOX and the noble metal phase and referred to as Fermi-level control mechanism [83]–[87]. The spill-over mechanism is mainly attributed to metallic clusters whereon oxygen [24], [25], [83] or reducing gases [83]–[87], e.g. CO or H_2, are adsorbed, activated, and subsequently transferred to the SMOX surface increasing the reactivity of the SMOX surface and thus the gas sensing effect [83]–[87]. In case of a spill-over related sensitisation, the reception takes place at the SMOX surface and the oxidation state of the noble metal remains unchanged [84]. Figure 11a shows the spill-over of oxygen and the subsequent reaction with CO on the SMOX surface. The activation of the gases on the metallic clusters may involve their dissociation [83]–[87] or a weakening of intramolecular bonds by the adsorption on the metal, e.g. by the partial filling of anti-bonding molecular orbitals [25], [48], [88]. The sensitisation by a Fermi-level control mechanism is based on an electronic interaction of the SMOX and the noble metal phase that has a different work function. The contact of the two materials leads to an alignment of the Fermi levels and in this way to a surface band bending [89]. This interaction pins the Fermi level of the SMOX and thus the surface band bending [89]; i.e. in the vicinity of the noble metal clusters the band bending is no longer determined by the presence of ionosorbed species, it is controlled by the contact of the SMOX and the noble metal (Figure 11b) [31], [86]. If the concentration of the noble metal loading is high enough and if it is well dispersed, the electron depletion caused by the noble metal loading completely controls the charge transport of the sensing layer (Figure 11c) [83]. In this case, the changes of the sensor resistance are solely caused by changing the electronic properties, i.e. the work function, of the noble metal loading, e.g. by (partial) reduction or oxidation. If a reaction causes a work function change of the noble metal cluster the electron depletion caused by the noble metal loading, and thus the resistance of the sensing layer, will be changed [86]. A Fermi level control mechanism is not limited to the contact of two solids; a

similar pinning of the SMOX's Fermi level is also caused by the introduction of noble metal related surface states, acting as electron acceptor or donor [89]. If there is no chemical or electronic interaction of the noble metal phase and the SMOX, the presence the catalytic more active noble metal causes a competitive reaction on the noble phase which decreases the concentration of the target gas which is reaction on the SMOX surface and thus decreases sensing effect [83] (Figure 11d). The mechanisms considered up to now assume that the noble metals form a separated phase (Figure 11 a-d), however, it was found that the noble metals can also be atomically distributed in the SMOX lattice (homogeneous dispersion) [21], [22], [90]–[92], where they may influence the chemical and electric properties of the SMOX. The presence of single noble metal ions at the SMOX surface creates new adsorption sites for reactive gases [20]. Furthermore, metal atoms that replace the cations of the SMOX within lattice are found to create donor [31] or acceptor [23], [31] states depending on their charge with respect to the one of the original cation. The effects of incorporated noble metal atoms are shown in Figure 11e.

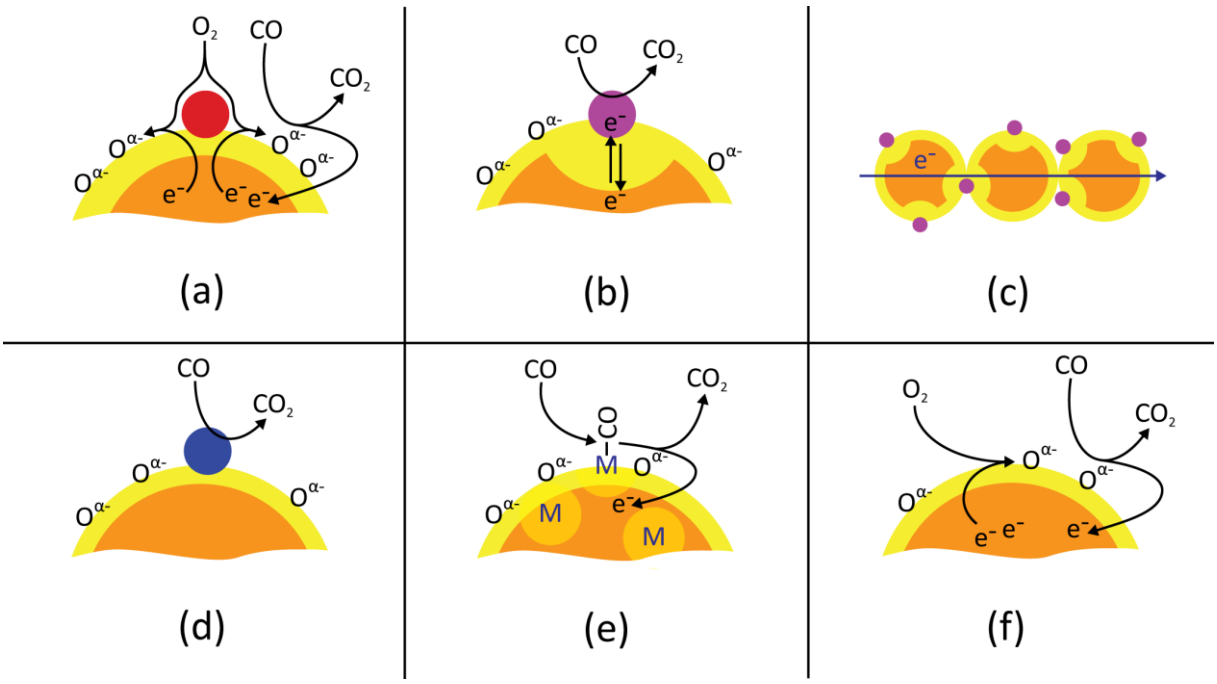

Figure 11. Effect of noble metal loadings for SMOX-based sensing materials: Spill-over of oxygen (a) – for analyte gases the mechanism is not shown, Fermi-level control (b, c), competing catalytic reaction (d), and atomic sites (e) acting as reactive sites and/or acceptors/donors. For comparison, the chemistry of pristine SMOX is given (f).

3. Fundamentals of the operando spectroscopic methods

3.1. Ex-situ, in-situ and operando methods for gas sensor research

The terms ex-situ, in-situ and operando are widely used to distinguish techniques, which are used to study functional materials, by the experimental conditions regarding their match with realistic operation conditions. The use of operando techniques is most widely spread in catalysis research and is defined as the combination of a spectroscopic technique with the on-line evaluation of the catalytic activity of the material [16]–[18]. This approach was adapted to study various kinds of functional materials, including gas sensors [6], [15]. In case of operando research on gas sensors, the sensor response, e.g. the sensor resistance of a SMOX-based gas sensor, is evaluated, while additional material properties are probed by spectroscopic or electrical techniques. The clear definition is still controversial, but a common classification of the three terms can be done as follows [6], [15]:

- Ex-situ experiments include all types of specimens, which are measured in any conditions, (temperature, pressure and atmospheric composition), that are not related to the actual operation conditions of the corresponding sensing material
- Experiments that are performed in-situ are done on any type of specimen in conditions that are relevant to gas sensor operation, but there is no simultaneous evaluation of the sensor response of the studied sample
- Operando experiments are done on real sensor devices, in conditions relevant to gas sensor application and involved the simultaneous evaluation of the sensor response.

Today's tool box of operando techniques for gas sensor research offers various spectroscopic and electrical techniques. The spectroscopic techniques range from IR [74], [93]–[95] and Raman spectroscopy [96], [97] over UV/vis [98] to X-ray absorption and emission spectroscopies [21], [22], [99]. The electrical techniques include work function measurements using the Kelvin probe setup [53], [100], [101], AC impedance spectroscopy [95], [102] and Hall effect measurements [103], [104]. The following chapter will briefly introduce the theoretical background of the operando spectroscopic techniques used in this work.

3.2. IR spectroscopy

IR spectroscopy is used to study molecular vibrations and enables the identification of molecules or functional groups [105]. The fundamental requirement is an IR-active vibrational transition, i.e. the dipole momentum of the molecule has to be changed due to the corresponding vibration [49], [106]. The energy of an IR transition is determined by specific parameters of the molecule or functional group, like the mass of the vibrating atoms and the bond strength between the vibrating atoms. The

potential curve of a diatomic molecule is shown in Figure 12. Close to the equilibrium distance of the two atoms, the potential can be approximated by a parabolic potential, and the vibration is described by a harmonic oscillator [49], [106].

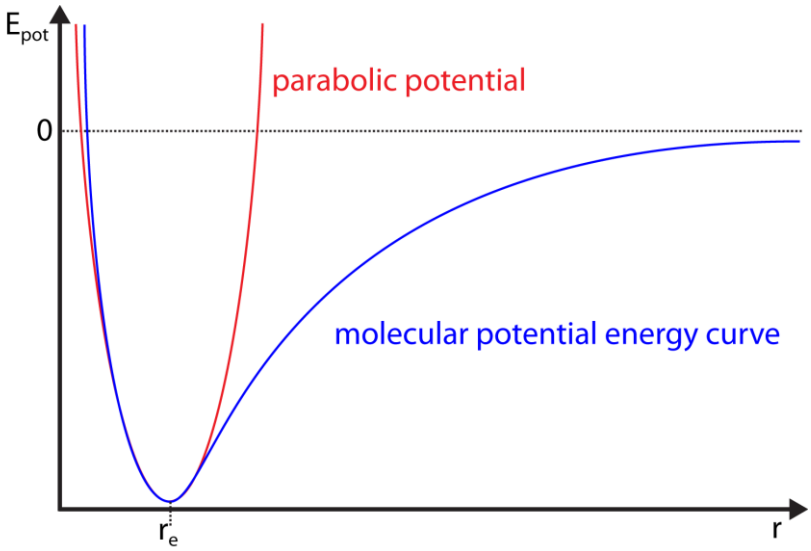

Figure 12. Molecular potential energy curve of a diatomic molecule (blue) and a parabolic potential (red). For higher energies, the approximation based on a parabolic potential is no longer valid. The figure is adapted from [49].

Based on this approximation, the dependency of the wavenumber of the IR transition on the masses of the involved atoms (reduced mass μ) and the bond strength (force constant k_f) is described by Equation 9, where c_0 is the speed of light.

$$\tilde{\nu} = \frac{1}{2\pi c_0}\sqrt{\frac{k_f}{\mu}} \qquad \textbf{Equation 9}$$

According to Equation 9, vibrations involving light atoms and/or strong bonds will be found at higher wavenumbers than of those involving heavier atoms and/or weaker bonds [105]. The effect of the bond strength is observed when comparing the O-H stretch vibrations of different surface hydroxyl groups: The O-H stretch vibration of acidic hydroxyl groups is found at lower wavenumbers; e.g. on zeolites, the O-H stretch band of very weakly acidic hydroxyls is found around 3745 cm^{-1}, while the ones of acidic Brønsted sites is found at 3610 cm^{-1} [105]. In case of hydroxyl groups on the surface of metal oxides, the acidity, and thus the position of the O-H stretch band, depends on the cation coordination of oxygen atom of the hydroxyl group; for zeolites, the band at 3745 cm^{-1} is assigned to terminal groups on Si (Si-OH) and the band at 3610 cm^{-1} to bridged hydroxyl groups (Si-OH-Al) [105]. If the mass of a hydroxyl group is changed by replacing the proton by deuteron, the correspond O-D stretch band is found at lower wavenumber. Based on Equation 9, the shift is calculated by:

$$\frac{\tilde{\nu}_{OD}}{\tilde{\nu}_{OH}} = \sqrt{\frac{\mu_{OH}}{\mu_{OD}}} \qquad \textbf{Equation 10}$$

The theoretical shift calculated by Equation 10 is 0.728, which is only slightly lower the experimental values of 0.737 for the OH/OD exchange terminal OH groups on SnO_2 [94]. The difference between the experimental shift and the one obtained by Equation 10 can be explained by the limitation of harmonic oscillator approximation for a diatomic molecule, which apparently fails to describe a surface hydroxyl group as a part of a more complex structure like a surface or solid.

The most common IR spectroscopic method to study solids is the transmission measurement of either very thin pellets or pellets of the substance diluted in KBr. Transmission measurements on thin pellets were the basis of many in-situ studies on SnO_2-based gas sensing materials [65], [107]. Another possible geometry to record IR spectra is diffuse reflectance, which emerged with the appearance of commercial mirror optics [105]. Diffuse Reflectance Infrared Fourier-Transform Spectroscopy (DRIFTS), requires a less complex sample preparation and enables operando measurements on thick film layers, i.e. SMOX-based gas sensors [108]. Reflection at surfaces includes two types of reflection: The specular or mirror-type reflection (Figure 13a) and diffuse reflectance (Figure 13b), which involves multiple reflection, refraction and diffraction processes inside the material [105], [109]. However, real surfaces will always show contributions of both types of reflection (Figure 13c).

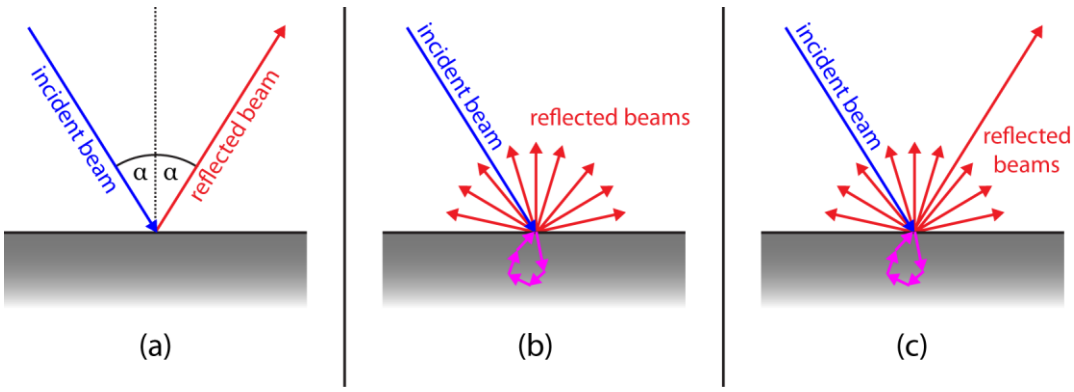

Figure 13. Specular reflection (a) diffuse reflection (b) and the superposition of both (c) on a surface. The incident beam is show in blue and the reflected beams in red. The radiation passing through the material by multiple processes (see text) is shown in magenta. The figure is adapted from [110].

Specular reflection is mainly found on flat and polished surfaces, while diffuse reflection dominates on rough surfaces and matt surfaces. In case of a layer consisting of individual grains, which are small with respect to the wavelength of the radiation, diffuse reflection will be the dominant process [105], [109]. The radiation penetrating the sample during diffuse reflection can be partially absorbed and thus diffuse reflected radiation possesses spectroscopic information about the sample. In order to record a spectrum in diffuse reflectance, special mirror optics are used to maximize the collection of diffuse reflected radiation [105], [109]. DRIFT spectra show the same qualitative features found in transmission spectra; however, the quantitative analysis of DRIFT spectra requires the use of the Kubelka-Munk theory for diffuse reflectance spectroscopy [105], [109].

3.3. UV/Vis spectroscopy

Diffuse reflectance spectroscopy (DRS) is not limited to IR radiation and is commonly used to record UV/vis spectra of solid samples, e.g. to study the electronic structure of a solid [109]. The reflection of UV/vis radiation is described by the same theory, which is described above for IR radiation. The electronic structure of a solid is characterized by energy bands instead of discrete sates [51]. In case of insulators or semiconductors the occupied valance band and the unoccupied conduction bands are separated by a forbidden zone, which is characterized by the energy gap between the valence band maximum and conduction band minimum [51]. In the simplest case, there is a direct optical band gap, i.e. the valence band maximum and conduction band minimum are found at the same coordinate in the reciprocal lattice (see Figure 14a). If the photon energy exceeds E_{Gap}, electron from the valence band will be excited to the conduction band (Figure 14b) and various electronic transitions between different levels of the two bands occur above this energy. There are several methods reported to extract E_{Gap} based on UV/vis absorbance spectra [109], [111], [112]. Besides the estimation of E_{Gap}, the UV/vis spectra of solids can provide information on point defects, electronic transitions of metal cations or the local surface plasmon resonance of metallic nanoparticles [109].

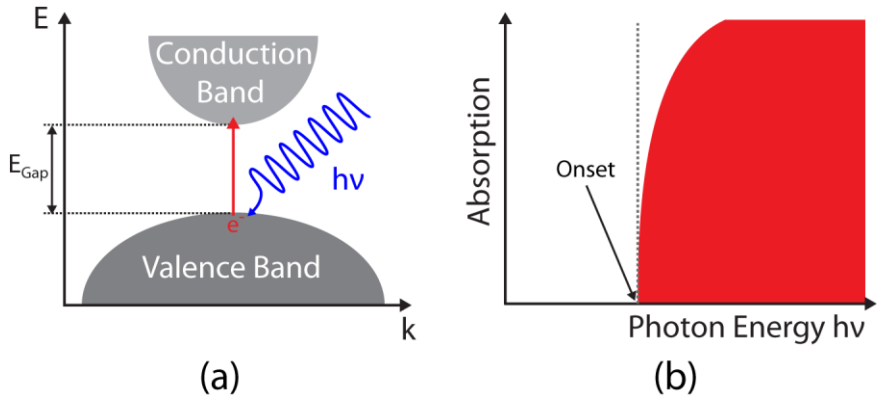

Figure 14. Direct optical band gap (a), i.e. the maximum of the valence band and the minimum of the conduction band are found at the same k-value (wave-vector), and The corresponding optical absorption (b), in case of a pure insulator at 0 K. The figure is adapted from [109].

3.4. X-ray Absorption Spectroscopy

Since their discovery X-rays became an essential probe to study the structure and composition of solids and today's X-ray-based methods involve various techniques based on diffraction, scattering, absorption or emission of X-rays [49], [113]. X-ray Absorption Spectroscopy (XAS) is used to characterize the structure and the electronic properties of a sample, and is a suitable technique for operando research as well as the study of highly dispersed active species [114], [115]. XAS is element specific, does not require long-range ordered samples and can be applied at normal pressure. Thus, XAS is a highly valuable tool to characterize noble metal loadings in gas sensing materials [116]. The X-ray absorption spectrum shows characteristic steps, at which the X-ray absorption drastically

increases. These steps occur if the energy of the incident photon is sufficient to excite a core level electron to a free electron state (see Figure 15a).

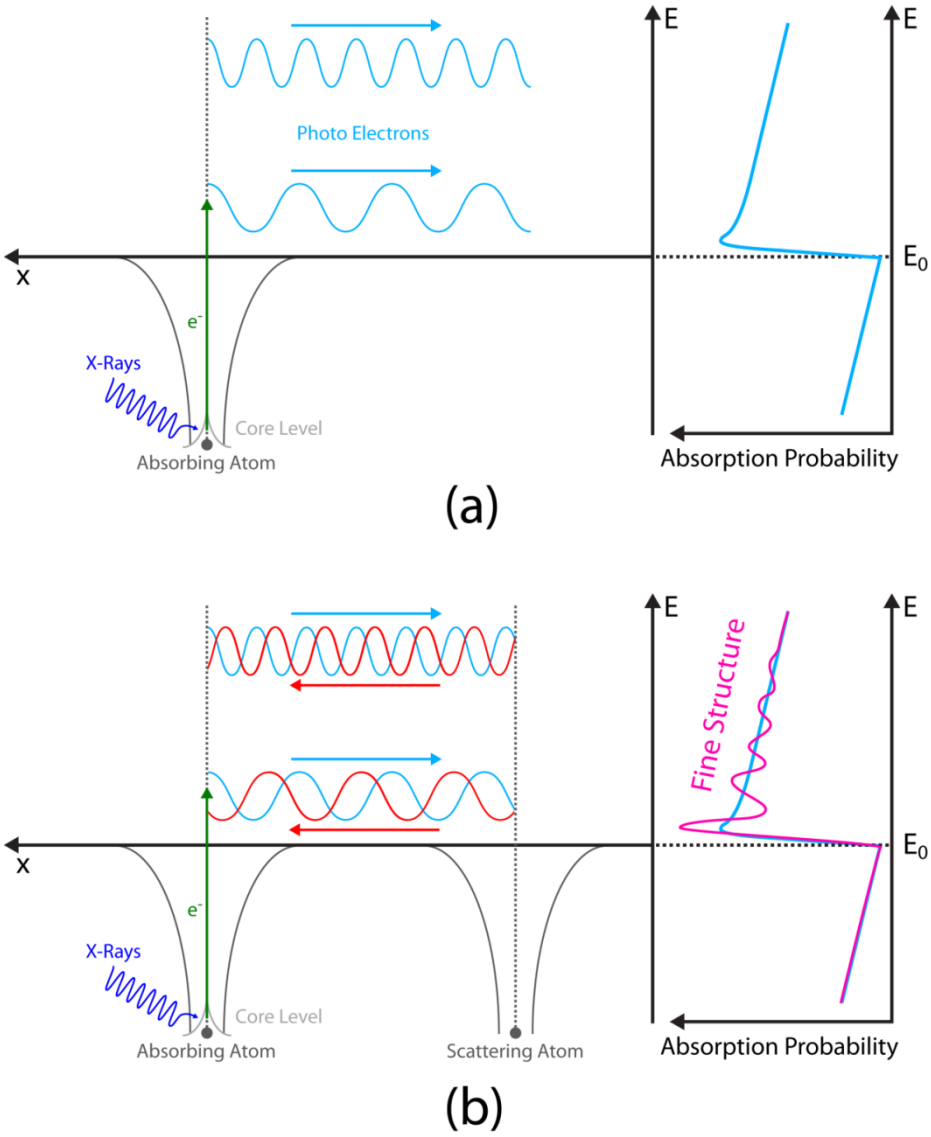

Figure 15. Schematic, one-dimensional representation of the photo electron emission and scattering processes in case of a monoatomic absorbing material (a) and an absorber with a neighbouring atom (b). The left part of the figure shows potential wells of the involved atoms, while the resulting absorption is shown on the right. The incident X-rays are shown in blue, excitation/photo electron emission in green and the wave functions outgoing or backscattered electrons in light blue and red, respectively. The figure is adapted from [117].

The curve of the absorption probability shown in Figure 15a corresponds to a monoatomic substance and has no fine structure. In case of a solid the X-ray absorption spectrum shows a fine structure (Figure 15b), which is commonly separated in two parts: The X-ray Absorption Near Edge Structure (XANES) and the Extended X-ray Absorption Fine Structure (EXAFS). The XANES region is typically located between -20 and +50 eV around the edge step and is determined by the electronic structure of the absorbing element. Thus, XANES spectra provide information on the oxidation state of the absorbing element and local geometric structure of the material [115]. The EXAFS region, which is located from +50 eV up to +600 eV after the edge step, originates form backscattering of the exited

electron by neighbouring atoms (Figure 15b). According to Fermi's golden rule the absorption propability depends on the wave function of the initial and final state of the involved electron. The initial state is defined by the core level of the absorbing atom and determines the energy of the absorption edge, while the finial state is defined the free electron [115], [118]. If the outgoing electron wave is scattered by a neighbouring atom, the backscattered electron wave interferes with outgoing electron waves. The resulting interference can either be constructive or destructive and thus certain transitions will be amplified or attenuated, respectively. As a result of the interference an oscillatory fine structure is found post the absorption edge [115]. The EXAFS contains information about the structure around the absorbing atoms and can be further analysed. Therefore, the EXAFS function χ(k) is obtained by subtracting the background (Equation 11) and converting energy into k (wave vector) by using Equation 12.

$$\chi(E) = \frac{\mu(E) - \mu_0(E)}{\mu_0(E)}$$ **Equation 11**

$$k = \sqrt{\frac{2m_e}{h^2}}(E - E_0)^{\frac{1}{2}}$$ **Equation 12**

The FT of the EXAFS function (Equation 13) is a pseudo-function of the radial distribution of backscattering neighbours in real space, where the peaks are shifted to lower distances due to dephasing [115].

$$FT(r) = \frac{1}{\sqrt{2\pi}} \int_k k^n \, \chi(k) e^{-2ikr} \, dk$$ **Equation 13**

The quantitative determination of structural parameters is done by fitting the EXAFS spectra using the EXAFS equation (Equation 14), which sums all contribution of backscattering neighbours [118].

$$\chi(k) = \sum_j S_0^2 \frac{N_j}{kr_j^2} F_j(k). \exp\left(-\frac{2r_j}{\lambda(k)}\right) \cdot \exp\left(-2{\sigma_j}^2 k^2\right) \cdot sin\left(2kr_j + \varphi_{ij}(k)\right)$$ **Equation 14**

The structural parameters of interest are the number of backscattering atoms (N_j) in a coordination shell of identical atoms, the corresponding average distance (r_j) and Debye-Waller factor (σ_j), which is a measure for the structural and thermal disorder of the sample. The other parameters are the amplitude reduction factor (S_0) and mean free path of a photo electron (λ(k)), which consider inelastic effects, as well as the backscattering amplitude $F_j(k)$ and the phase shift $\varphi_{ij}(k)$, which are element specific for each backscattering atom [118]. Due to the short mean free path of electron in a solid, the EXAFS only provides information on the local structure, i.e. within a few coordination shells around the absorbing element [115], [118].

4. Materials & Experimental Methods

4.1. Sample Preparation

The preparation of a gas sensor involves the preparation of the sensing material, usually as a powder, and the deposition of the sensing material onto the sensor substrate.

4.1.1. Powder Preparation

Nanosized SnO_2 was obtained by an aqueous sol-gel process, followed by subsequent milling and calcination procedures [28], [88]. In a three-neck round-bottom flask a 2 M aqueous ammonia solution was prepared by diluting an aqueous ammonia solution (Riedel-deHean, 33 %vol.) in deionized water and cooled down to 0 °C. An aqueous solution of $SnCl_4$ (Merck, purified by distillation) was added dropwise to the cooled 2 M aqueous ammonia solution under stirring. After $SnCl_4$ solution was completely added, the reaction mixture was stirred at room temperature for 30 min. The obtained white precipitate was separated by centrifugation and repeatedly washed with deionized water, until no chlorine was found by precipitation with $AgNO_3$ in the separated liquid phase. The washed powder was dried at 120 °C. The obtained glassy crystals were first ground in a mortar and afterwards using a shaker mill (30 Hz, 3 h) with ZrO_2 balls (⌀ 5 mm). The obtained white powder was calcined 1000 °C for 8h and afterwards ground using a shaker mill (30 Hz, 3 h; ZrO_2 balls, ⌀ 5 mm). The process is summarized schematically in Figure 16 (grey route).

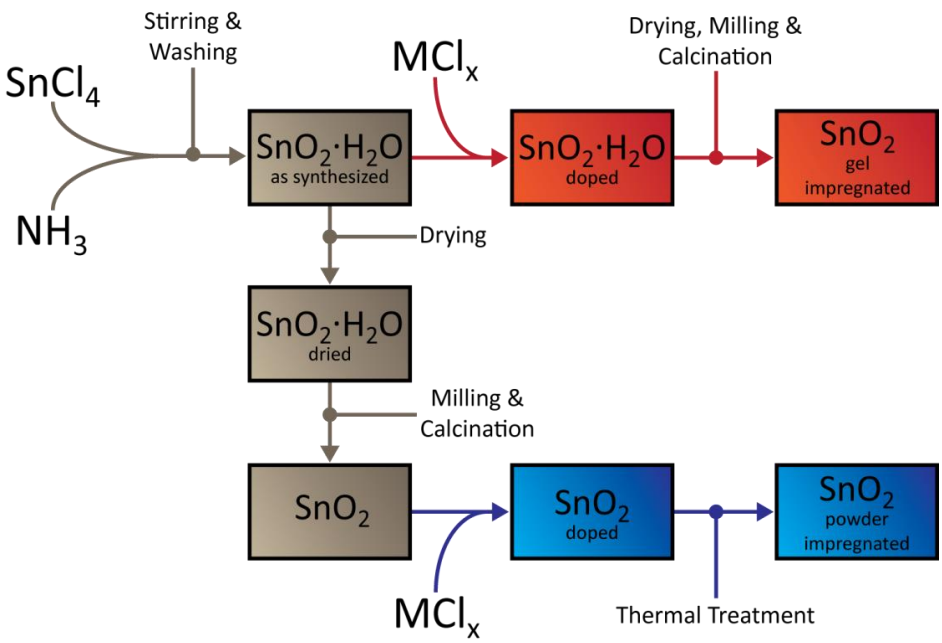

Figure 16. Material preparation schema for undoped and doped SnO_2 gas sensing materials obtained by an aqueous sol-gel route: synthesis of SnO_2 starting with $SnCl_4$ (grey), noble metal introduction by gel impregnation (red) and powder impregnation (blue).

During the powder preparation, the addition of noble metal loadings can be done in two different ways: The noble metal can be added prior the calcination/milling step (Figure 16, red route) or after

the calcination/milling step (Figure 16, blue route); these routes are referred to as gel impregnation or powder impregnation. The present work is focused on Pt-doped SnO_2 materials made by the powder impregnation route, thus only this route is described in detail. It was done by adding an aqueous solution of $PtCl_4$ (Sigma-Aldrich, ≥99.99 % trace metal basis) to an aqueous suspension of undoped SnO_2, to obtain nominal loadings of 0.2 and 2.0 %wt. Pt. The reaction mixtures were stirred at room temperature for 48 h. The solid was separated by centrifugation, washed with deionized water, dried at 80 °C and finally annealed at 450 °C for 1 h. The annealed powder was ground using a shaker mill (30 Hz, 3 h; ZrO_2 balls, ⌀ 5 mm).

4.1.2. Sensor Fabrication

The sensing layers were deposited by screen-printing a 1,2-propandiol-based paste of the sensing materials onto a sensor substrate, which is equipped with interdigitated electrodes on the front and a heating meander on the back (see Figure 17). Generally, the electrodes and the heater are made of Pt; however, for the operando X-ray spectroscopic investigations of the Pt-doped sample the electrodes are made of Au and the heater of an Pd/Ag alloy, to avoid any signal of the electrodes or the heater.

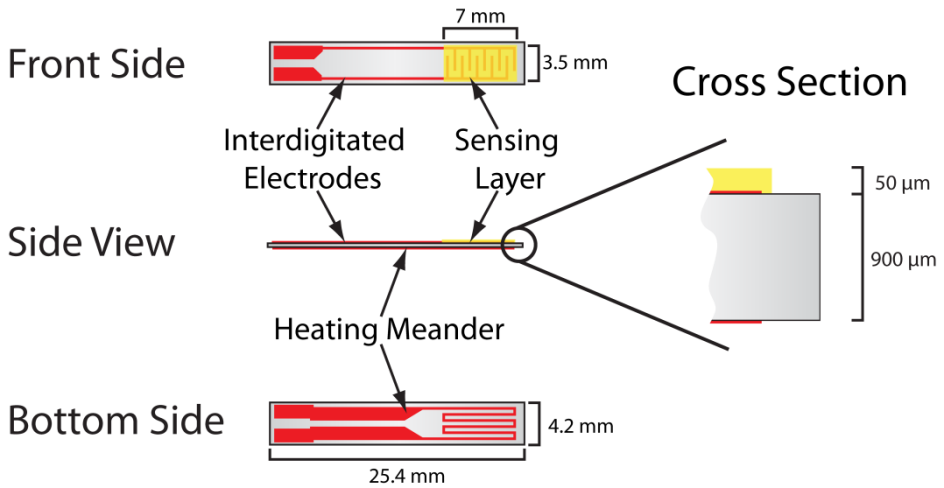

Figure 17. Schematic drawing of a sensor substrate with a sensing layer (yellow) and interdigitated electrodes (red) on the front side and a heating meander (red) on the back. The thickness of the electrodes and heating meander are 5 µm.

After printing the sensors were dried at 70 °C and annealed at stepwise varied temperatures (300 °C, 400 °C, 500 °C and 400 °C). For each individual sensor a temperature calibration was made, by plotting the temperature of the sensing layer versus the resistance of the heater. Based on the linear relation of layer temperature and the resistance of the heater the sensor can be precisely heated during the experiments.

4.2. Experimental Techniques

The following section gives an overview of the experimental techniques, including the basic material characterization, the gas mixing systems used for the investigations and a description of the of the in-situ/operando spectroscopic techniques.

4.2.1. Basic Material Characterization

The prepared undoped and Pt-doped sensing materials were characterized by different material characterization techniques. The experimental details of the basic characterization techniques are described in the following section.

4.2.1.1. X-ray powder diffraction (XRD)

Powder X-ray powder diffraction was done on a Bruker D8 Advance diffractometer, using Ge-monochromated Cu-K_α radiation, which was recorded with a VÅNTEC-1 X-ray detector in transmission geometry. The powder sample was deposited between two sheets of an X-ray amorphous polymer foil and fixed on a rotating sample holder. The measurement was done at the Institut Català d'Investigació Química (ICIQ) in Tarragona, Spain.

4.2.1.2. Vibrational spectroscopies

FT-IR transmission spectra were recorded on a N_2-purged Bruker Vertex70 spectrometer equipped with an internal mid IR globar and a RT-DLaTGS detector. Spectra were recorded from pellets with the sample diluted in KBr (0.5 wt%), with a spectral resolution of 0.5 cm^{-1} and as an average of 128 scans. IR spectra were processed using Bruker's OPUS software. The absorption was calculated taking the spectrum of a pure KBr pellet as reference. Raman spectra were recorded at the ICIQ using a fibre optic Raman probe with a 532 nm Laser (internal Laser source of a BWTEK iRaman microbeam Raman spectrometer) for excitation and a cooled CCD spectrometer (BWTEK Exemplar Plus) for detection. Raman spectra were recorded from powders placed on an aluminium sample holder.

4.2.1.3. Electron microscopies

Secondary electron images were recorded by scanning electron microscopy (SEM) using a HITACHI SU8030 cold filed emission scanning electron microscope, with an acceleration voltage of 5 kV and a probe current of 10 µA. All SEM images were recorded from powders supported on adhesive carbon pads and a working distance of 1.9 mm.

Transmission electron microscopy (TEM) was done at the Karlsruhe Nano Micro Facility (KNMF) of the KIT. Powder samples were placed on a carbon coated Cu grid and measured on a FEI Titan 80-300 aberration corrected electron microscope with an acceleration voltage of 300 kV. High-angle annular

dark field scanning transmission electron microscopy (HAADF-STEM) was recorded with a Fischione model 3000 HAADF-STEM detector.

4.2.1.4. Quantitative element analysis

The Pt content of the Pt-doped SnO_2 materials was determined by inductively coupled plasma optical emission spectrometry (ICP-OES), which was conducted at the Institute for Applied Materials - Applied Materials Physics (KIT) using a PerkinElmer Optima 4300 DV spectrometer. Prior the measurement the Pt-doped SnO_2 powders were dissolved in an acidic solution (HCl, H_2SO_4 and H_2O_2) at 240 °C (8 h). The Pt concentrations of the samples were determined by triple measurements

4.2.2. Gas Mixing

The precise and reproducible dosing of gas mixtures is an essential requirement for studying gas sensors. For this purpose, homemade gas mixing systems (GMS) are used, the systems vary in size and specifications, but are all based on the same concept shown in Figure 18. Each gas mixing system consists of a series of channels for dosing the carrier gas or test gases supplied by a gas bottle or a vaporizer. Each channel has a mass flow controller (MFC) to adjust the gas flow and two magnetic valves to prevent unintended gas diffusion. All parts of the GMS are connected by electrically polished stainless steel pipes or Teflon tubes. The MFCs and valves are operated by customized software (Agilent VEE). To obtain a certain test gas concentration at a given flow rate the flow the carrier gas and the test gas, generally pre-diluted in the carrier gas (ppm-range), are adjusted by the corresponding MFCs. For test gases dosed using a vaporizer the concentration is considered to be 100 % of the saturation at room temperature. If no water vapour is dosed and the gas stream is referred to as dry, however, also in this condition a low water vapour background of typically 10 to 20 ppm H_2O is found.

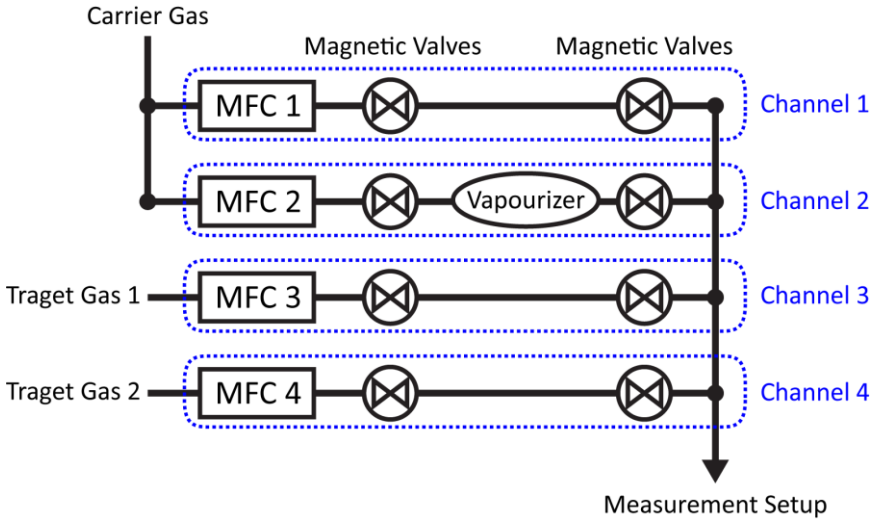

Figure 18. Schematic drawing of a gas mixing system with four channels: Carrier Gas (Channel 1), Humidity dosing (Channel 2) and two different test gases (Channel 3&4).

For all measurements done at the University of Tübingen, test gases (CO, ^{13}CO, H_2 and O_2) and carrier gases (synthetic air and N_2) were supplied by Westfalen AG, Münster. The purity of the carrier gases was 99.999 % for synthetic air (20.5 % oxygen) and 99.9999 % for N_2. For all test gases, an analysis certificate was delivered by Westfalen AG. Deionized water (building's supply system) and heavy water (euriso-top or Sigma-Aldirch, each with 99.9 % purity) were used for the vaporizers to generate water vapour. For the measurements at the synchrotron light sourches, test gases from Westfalen were used; synthetic air and a H_2/He-mixture were delivered by the local supply infrastructure.

4.2.3. DC Resistance Measurements

Recording the DC resistance (DCR) is a common way of measuring the gas sensing performance of SMOX-based gas sensors [102]. A standard experimental setup is shown in Figure 19 (left); gases are dosed by a GMS, which delivers a continuous gas flow (150 sccm) to a measurement chamber containing one sensor fixed in a socked with a feedthrough to connect the sensor's electrodes and heater to a digital multimeter (Keithley 199 or Keithley 2000) and a power supply (Agilent E 3630A or similar), respectively. The GMS and resistance measurements are controlled by a computer. The sensor's temperature is controlled by adjusting the voltage applied to the heater according to a previously made calibration of the heaters resistance and the temperature of the sensing layer. Resistances up to approximately 300 MΩ can be recorded by a digital multimeter [119], [120]. The simplified resistance measurement circuit is shown in Figure 19 (right). The used digital multimeters determined the resistance of the sensor (R_{Sens}) according to Equation 15 from the measured potential drop over the sensor (U_{Sens}) and a reference resistor (U_{Ref}) with a known resistance (R_{Ref}) at a constant current [120].

$$R_{Sens} = \frac{U_{Sens}}{U_{Ref}} \cdot R_{Ref} \qquad \textbf{Equation 15}$$

The above described resistance measurement setup is also used for all operando measurements.

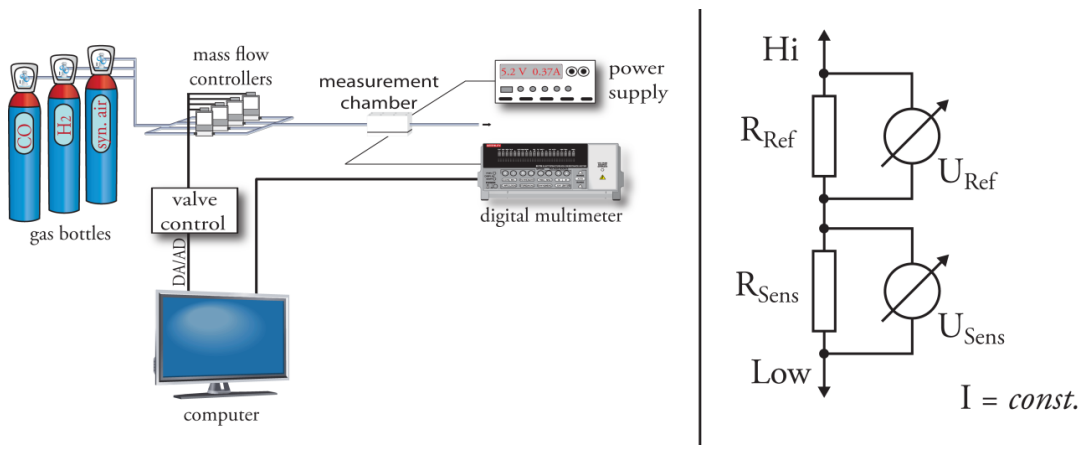

Figure 19. Set-up for resistance measurements (left) and simplified resistance measurement principle of a Keithley 199 digital multimeter (right).

4.2.4. Catalytic Conversion Measurements

The partial or complete oxidation of reducing gases on the sensing material's surface is the essential process of gas reception. Thus, information on the chemical activity of the material provides fundamental insights in the influence of interfering gases as well as noble metal loadings. The catalytic conversion of CO was studied at various temperatures and humidity backgrounds. To avoid an influence of the Pt-heater and electrodes [121] the measurements were performed on powders.

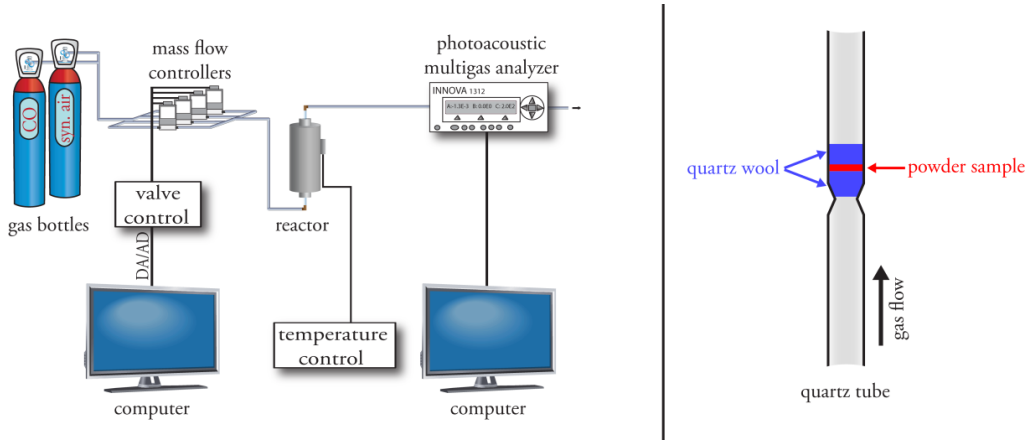

Figure 20. Set-up used for catalytic conversion measurements of powders (left) and drawing of a powder sample deposited in a quartz tube (right).

Therefore, 60 mg of non-diluted sensing material were deposited on quartz wool in a quartz tube and placed in a tube furnace (see Figure 20). Gases were dosed as describe above. The CO and CO_2 concentrations were measured by a photo-acoustic IR gas analyser (INNOVA 1312). Due to the high noise level of the CO_2 signal the catalytic conversion was calculated based on the residual CO concentration using Equation 16.

$$CC_{\%} = \left(1 - \frac{c_{CO,measured}}{c_{CO,reference}}\right) \cdot 100\% \qquad \textbf{Equation 16}$$

4.2.5. Diffuse Reflectance Infrared Fourier-Transform Spectroscopy

In-situ and operando IR spectroscopy was measured in diffuse reflectance using a six-mirror optic (Harrick Praying Mantis Diffuse Reflection Accessory). In-situ DRIFTS were recorded by using a N_2-purged Bruker Equinox55 spectrometer, equipped with an internal mid IR globar and a liquid-N_2-cooled mid-band MCT detector. The non-diluted powders were placed in a commercial in-situ cell (Harrick Praying Mantis High Temperature Reaction Chamber) with KBr windows, which allowed the temperature to be adjusted with a build-in heating system. In-situ DRIFT spectra were recorded with a resolution of 4 cm^{-1} and as an average of 1024 scans. The Operando DRIFT spectra were recorded with a spectral resolution of 1 cm^{-1} (512 Scans) by using an evacuated Vertex70v spectrometer

equipped with an external high performance mid IR globar and a liquid-N_2-cooled mid-band MCT detector. The sensors were placed in a homemade operando cell with a KBr window, gas in and outlet and electrical connectors, which allows the sensors' resistance to be measured and applying a heating voltage to the backside heater. The operando DRIFTS setup is displayed in Figure 21.

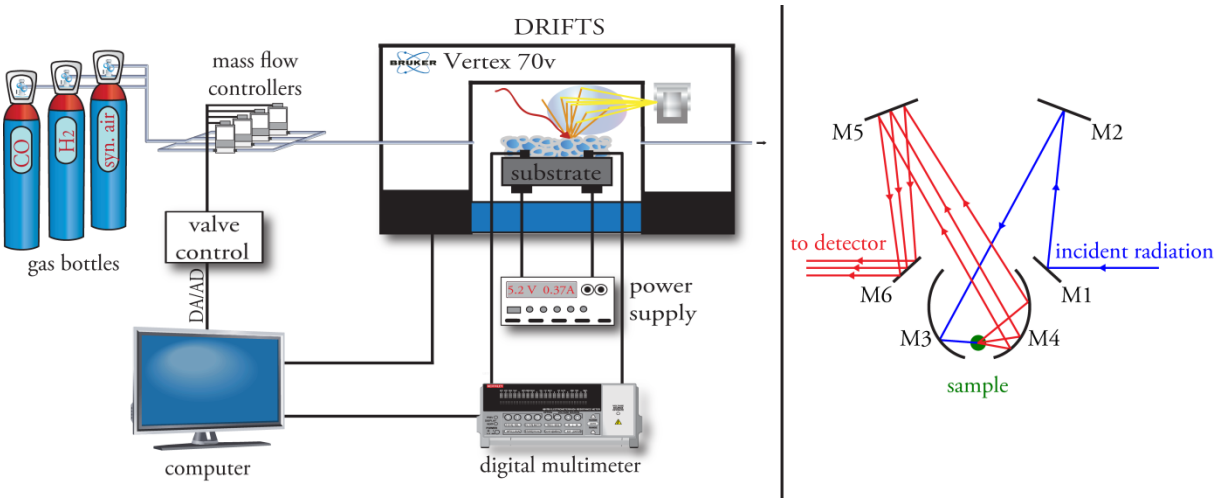

Figure 21. Setup used for operando DRIFT spectroscopy (left) and a schematic drawing of the mirror optic used for in-situ and operando DRIFTS (right). The mirror optic consists of four flat mirrors (M1, M2, M5 and M6) and two parabolic mirrors (M3 and M4).

Operando DRIFT spectra were recorded with a resolution of 1 cm^{-1} and as an average of 512 scans. During the measurements in low oxygen backgrounds or the absence of oxygen the residual oxygen concentration was measured using a Zirox SGM4 oxygen analyser. IR spectra were processed using Bruker's OPUS software and MatLab. To determine the differences in the material caused by changes of the gas atmosphere the absorbance was calculated by taking a spectrum of the sample recorded during exposure to the carrier gas, instead of an external substance, as a reference; this approach is also referred to as apparent absorbance [94], [122]. The absorbance spectra were calculated by using Equation 17.

$$A = -log\left(\frac{I_{gas}}{I_0}\right) \qquad \textbf{Equation 17}$$

4.2.6. UV/vis Diffuse Reflectance Spectroscopy

Ex-situ and operando UV/vis spectra were recorded from sensors in diffuse reflectance geometry using the above mentioned six-mirror optic. A combined deuterium/halogen light source (Ocean Optics DH-2000-BAL) and a CCD UV/vis spectrometer (Ocean Optics Maya 2000) were connected to the mirror optic using optical fibres. In order to avoid an influence of external light the whole setup was placed in a darkened compartment. Spectra were recorded with an integration time of 60 ms as an average of 256 scans. The gas sensor was placed in an operando cell, which similar to the one used for operando DRIFTS, but is equipped with a quartz instead of a KBr window. During the

operando measurements in N_2, the oxygen background was monitored by using a Zirox SGM4 oxygen analyser. All spectra were referenced to sensor coated with a $BaSO_4$ layer. The reflectance is calculated according to Equation 18. The optical band gap of SnO_2 was determined by the method described by V. Kumar et al. [111].

$$R_{\%} = \frac{I_{Sample}}{I_{Ref}} \cdot 100\% \qquad \textbf{Equation 18}$$

4.2.7. X-Ray Absorption Spectroscopy

Ex-situ X-ray absorption spectra of the Pt-doped SnO_2 materials were recorded at the Pt L_3 absorption edge in fluorescence mode using a 7-element Ge detector (Canberra). The measurements were done at the P65 undulator beamline the PETRA III synchrotron light source (DESY, Hamburg/Germany). The incident energy was tuned by a Si (111) double crystal monochromator. XANES and EXAFS spectra were recorded from powders deposited in Kapton tubes, which were place in the X-ray beam (spot size: 1x0.2 mm). X-ray absorption spectroscopy on sensors was done at the undulator beamline ID26 at the ESRF. A pair of Si (111) monochromators was employed to select the incident energy. XANES spectra were recorded in high energy resolution fluorescence detection (HERFD), by measuring the Pt $L_{\alpha 1}$ emission line (9442 eV) as a function of the incident energy, by using an X-ray emission spectrometer with four spherically bent Ge crystal analysers. The operando cell, crystal analysers and an avalanche photodiode for measuring the X-ray intensity were arranged in vertical Rowland geometry. The measured sensor was placed in a homemade operando cell with a Kapton window, gas in and out let and electrical connectors for resistance measurement and heating (see Figure 22) [21]. The X-ray absorption spectra were processed using the ATHENA program from the IFFEFIT software package [123].

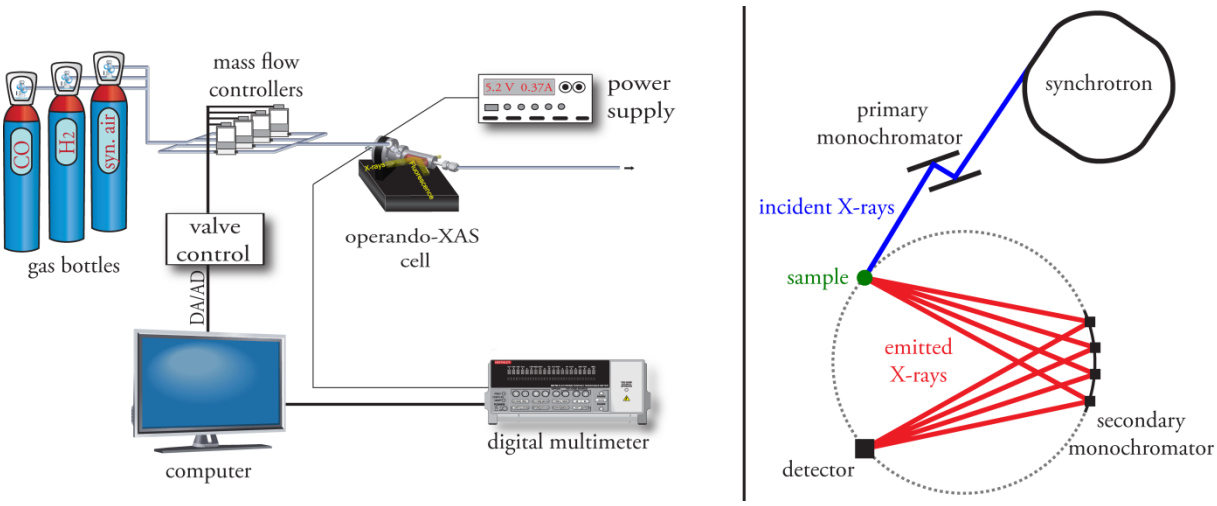

Figure 22. Setup for operando XAS (left) and a simplified image of the beam path for recording HERFD-XANES (right).

5. The Gas Reception Mechanism of Pristine Tin Dioxide

5.1. Basic Characterization of undoped SnO_2

The prepared undoped SnO_2 material was characterized by XRD, SEM, IR and Raman spectroscopy. The X-ray diffraction pattern of the synthesized SnO_2 powder (see Figure 23) matches the ICSD reference of Cassiterite (#41-1445), i.e. the synthesized SnO_2 is present in the tetragonal Rutile structure [10], [28]. The congruent positions of the reflexes for the sample and reference exclude a high inner disorder of the prepared material, which is only observed for materials calcined at lower temperatures [10], [28]. The sharp reflexes of the prepared SnO_2 indicate a high crystal quality and large crystal size, as previously reported for sol-gel derived SnO_2 calcined at 1000 °C for 8 h [10]. The particles size of the SnO_2 material is estimated by SEM. The secondary electron micrographs of undoped SnO_2, present rather large particles with an average diameter of 99±33 nm (see Figure 24). The found grain diameter is in good agreement with the diameter for similarly prepared SnO_2, which was found to be 100-110 nm by TEM [10], [28] and 144 nm by N_2 physisorption [28]. The larger particle size found by N_2 physisorption is attributed to the agglomeration of individual particles, which decreases the surface area of the material [28].

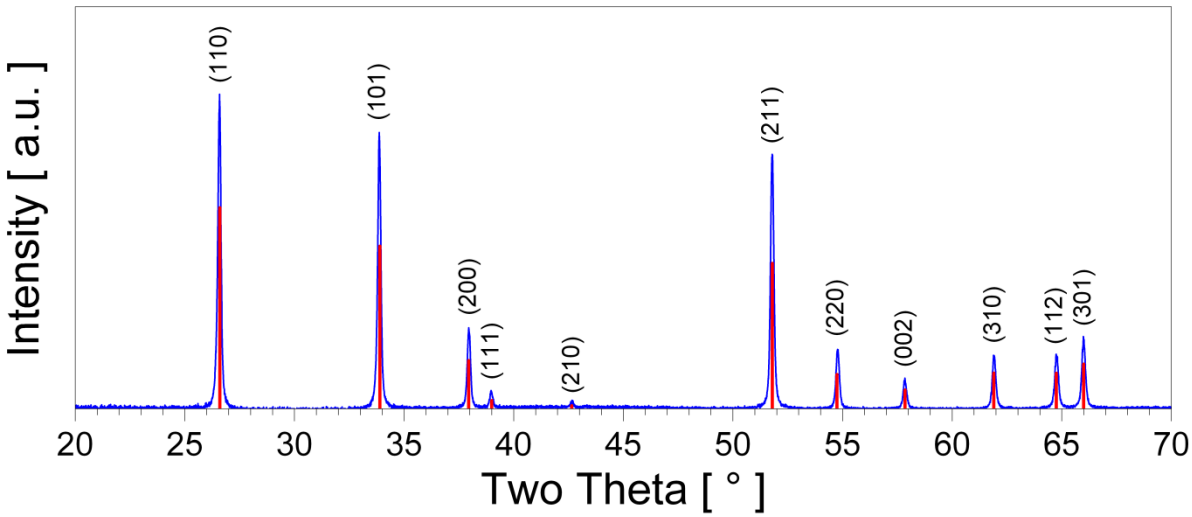

Figure 23. Powder XRD of undoped SnO_2 calcined at 1000 °C for 8h (blue) and the ICSD reference pattern #41-1445 (red).

The transmission IR spectrum of a KBr pellet with 0.5 wt% SnO_2 (Figure 25, left) shows a strong absorption between 450 and 800 cm^{-1}. It can be attributed to the fundamental lattice vibrations of SnO_2 (see Table 1), as well as to fundamental modes of Sn-O and Sn-O-Sn vibrations [76], [124], [125]. In the Raman spectrum (Figure 25, right) of the SnO_2 powder three Raman active fundamental modes are identified, E_g (468 cm^{-1}), A_{1g} (625 cm^{-1}) and B_{2g} (769 cm^{-1}), in agreement with the values reported in Table 1. Additionally, the band found at 686 cm^{-1} is attributed to the disorder activation of the Raman-forbidden A_{2u} mode [34]. The high intensity and sharpness of the bands corresponding to the Raman-active fundamental vibrations and the absence of broad band centred around

550 cm^{-1}, suggests only a low level of oxygen vacancies and low disorder of the prepared SnO_2 material [34], [126]. A direct optical band gap of 3.79 eV was derived from a UV/vis reflectance spectrum (see Supporting Figure 3), which is in line with the value of 3.6 eV reported in literature for nearly ideal SnO_2 single crystals [43]. In summary, the basic material characterization reveals that the prepared SnO_2 material is highly crystalline, has a low oxygen vacancy concentrations and forms grains with a diameter of approximately 100 nm. These material properties are in line with the ones reported for SnO_2 prepared by a similar synthesis route, but different milling procedure [10], [28], [34].

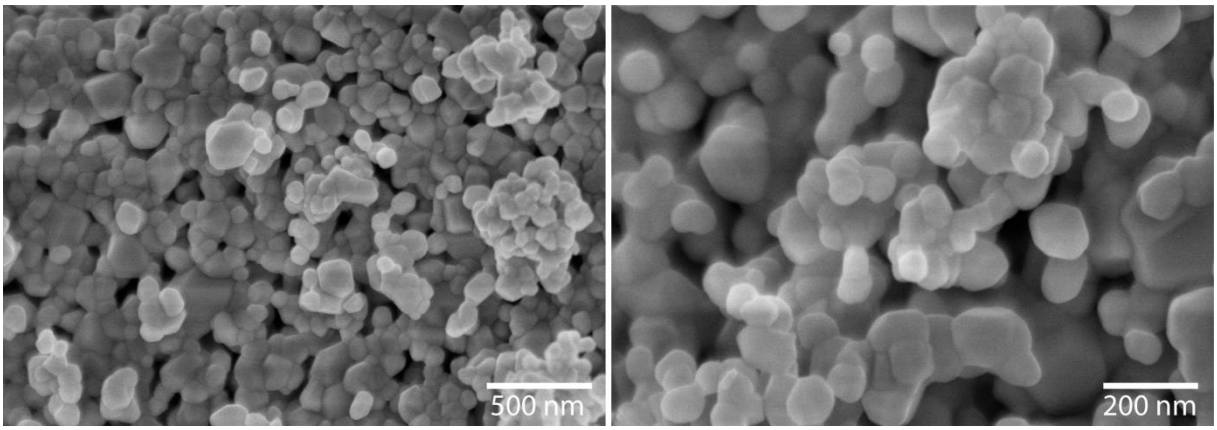

Figure 24. Secondary electron scanning microscopy images of undoped SnO_2 powder with a magnification of 45000x (left) and 100000x (right).

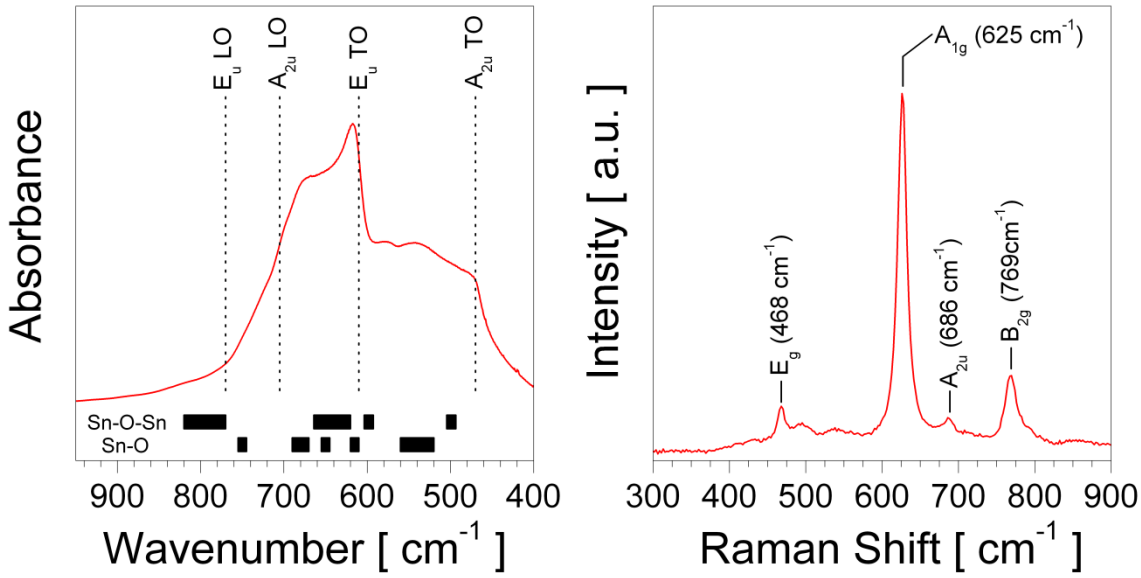

Figure 25. IR spectrum (left) and Raman spectrum of SnO_2 calcined at 1000 °C for 8 h. The dotted vertical lines in the IR spectrum correspond to the IR-active fundamental vibrations reported in Table 1, the horizontal lines to Sn-O and Sn-O-Sn vibration modes reported in literature (see text). The Raman-active fundamental vibrations are marked in the Raman spectrum.

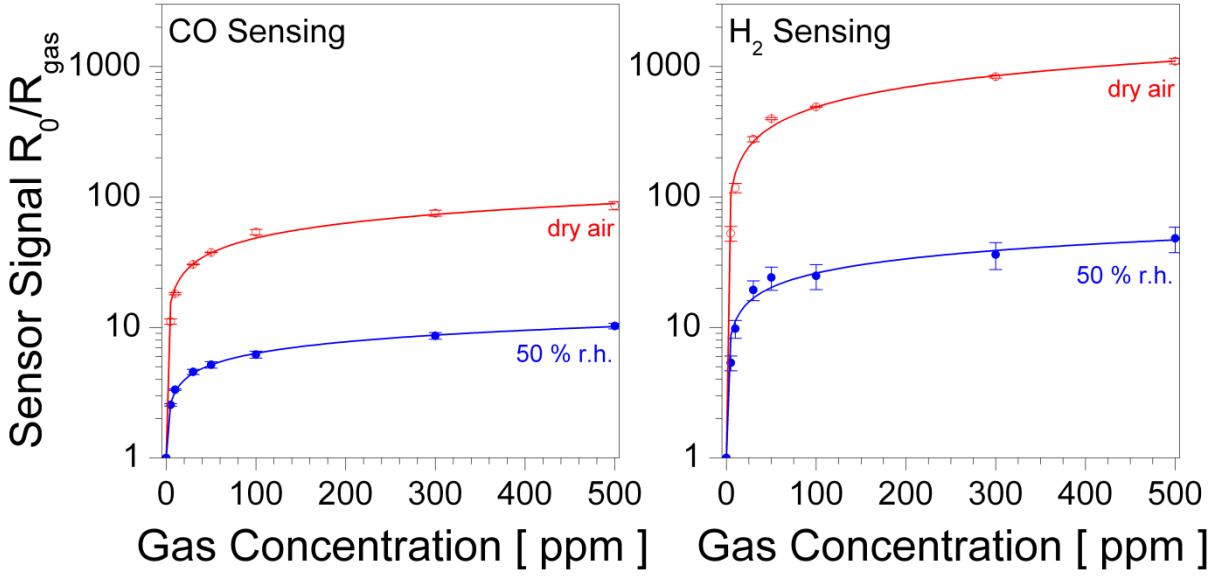

Figure 26. Gas sensing performance of undoped SnO_2 measured at 300 °C in dry air (red) and 50 % r.h. (blue). The calibration curves for 5-500 ppm CO and H_2 of are based on the averaged sensor signal of three independently measured sensors.

The gas sensing performance for CO and H_2 of the sensors is shown in Figure 26. They show the well-known characteristics of undoped SnO_2. The non-linear calibrations curves flatten with increasing test gas concentration, i.e. the sensitivity decreases for high gas concentrations. This power law relation between the test gas concentration and the resistance of the gas sensing layer corresponds to the characteristics expected for gas sensors based on porous thick film layers with large, spherical grains [52], [127]. In the presence of water vapour a distinct decrease of the sensor signals for CO and H_2 is observed, which is typical for undoped SnO_2 and generally ascribed to the competition of H_2O and the reducing gases for the same reactive surface species [20], [94]. In conclusion, this prepared undoped SnO_2 material is a representative and adequate material for further research on SnO_2-based gas sensors.

5.2. Identification of the Reactive Oxygen Species on pristine SnO_2

The nature of the oxygen species on SnO_2, which are involved in the gas sensing process, is one of the most discussed and essential questions related to the understanding of the gas sensing properties of SnO_2 [19], [52]. The commonly accepted model for gas sensing with n-type SMOX like SnO_2, is based on the ionosorption of oxygen, which causes an electron depleted layer at the surface of the SMOX grains. In the presence of a reducing gas a small fraction of the oxygen reacts with CO and is thereby removed from the surface. The lower concentration of ionosorbed oxygen leads to a decrease of the electron depleted layer (see 2.3. Working Principle of Tin Dioxide Based Gas Sensor) [52]. Based on this model, sensing of reducing gases would only be possible in the presence of ionosorbed oxygen species and thus only in the presence of atmospheric oxygen. However, it was found, that in the absence of atmospheric oxygen, i.e. a few ppm of residual O_2, the materials show a reversible response to reducing gases [53], [128], [129]. In the case of CO or H_2 exposure, the sensor signals exceeded the signals measured in air (20.5 vol% O_2); interestingly, for but both gases no oxidation product, i.e. CO_2 or H_2O, was found in the exhaust. Based on these findings the formation of a test gas related donor species, CO^+ or H^+ respectively, was proposed, which injects electrons into the conduction band [53], [128], [129]. The increased electron concentration at the SMOX surface leads to the formation of a narrow electron enriched region, which is denoted as accumulation layer. The formation of such an accumulation layer and the consequent changes in the transduction, were experimentally found in the absence of oxygen [53]. These findings allowed to extend the working model based on ionosorption, summarized as follows: In pure nitrogen, there is no electron donor or acceptor causing an accumulation or depletion layer, respectively. In the presence of oxygen, a depletion layer is formed, which increases the resistance. In air the resistance changes due to exposure to reducing gases are determined by changes of the ionosorbed oxygen concentration. In the absence of oxygen, the adsorption of donor molecules leads to an accumulation layer and a resistance decrease. The extended ionosorption model implies that in application conditions, i.e. in dry and humid air, the resistance is always above the resistance in nitrogen, while during the exposure of reducing gases in the absence of oxygen results in resistance below the resistance in nitrogen [129]. However, it was experimentally shown for pristine SnO_2, that in application relevant conditions, namely in air (20.5 vol% O_2) containing humidity (6 to 50 % r.h.), resistances below the resistance in N_2 were found during CO exposure [130]. Consequently, the formation of an accumulation layer and the associated processes are not limited to special ambient conditions and by that gain a practical relevance besides the existing academic interest. However, in the presence of oxygen, the occurrence of test gas related donor species (CO^+ and H^+) is rather questionable and the experimental evidence is missing. A good starting point to assess possible electron donor species is theory. Theoretical calculations describe two possible interactions of CO with SnO_2 (101) and (110)

surfaces, respectively [56], [57], [131]. One possible interaction is the reaction of CO with 2-fold coordinated lattice oxygen (bridging oxygen) forming a carboxylate intermediate which desorbs as CO_2 and creates an oxygen vacancy (see Reaction 14 and Reaction 15 in 2.2.5.3. Adsorption of Carbon Monoxide and Carbon Dioxide). This process can be considered a reduction of the SnO_2 surface, which involves charge transfer from the formed oxygen vacancy to the solid [56], [57]. The other proposed interaction is the adsorption of CO on a Sn site (Reaction 17). The formation of a carbonyl species bound to Sn is considered to be a possible intermediate during the CO oxidation [56], [57]. If charge is transferred from CO to the solid, this interaction is considered the formation of a test gas related donor species. However, the charge transfer from CO to the solid is 20 times less than the one expected for the reduction of the SnO_2 surface [57]. Based on the differences in the associated charge transfers, a rather high concentration of carbonyls should be present in order to have a similar electronic effect to that of the formation of oxygen vacancies. If one of the models proposed by the theoretical calculations is correct, the corresponding changes of the SnO_2 surface should be measurable by operando spectroscopy. One of the most suitable operando spectroscopic techniques is DRIFTS. The formation of carbonyl species should be associated with the appearance of a C=O stretch vibration in the IR spectrum (2300 to 1800 cm^{-1}) [132]. The formation of an oxygen vacancy, i.e. the removal of lattice oxygen, will cause a decrease of bands involving Sn-O bonds (see Figure 25) and their corresponding overtone bands.

5.2.1. Operando DRIFTS investigation on the reactive oxygen species

To examine the two proposed donor species, a series of DRIFTS experiments was performed in dry and humid (10 % r.h. at 25 °C) conditions. The DRIFT spectra of undoped SnO_2 exposed to 300 ppm CO in dry and humid conditions is shown in Figure 27.

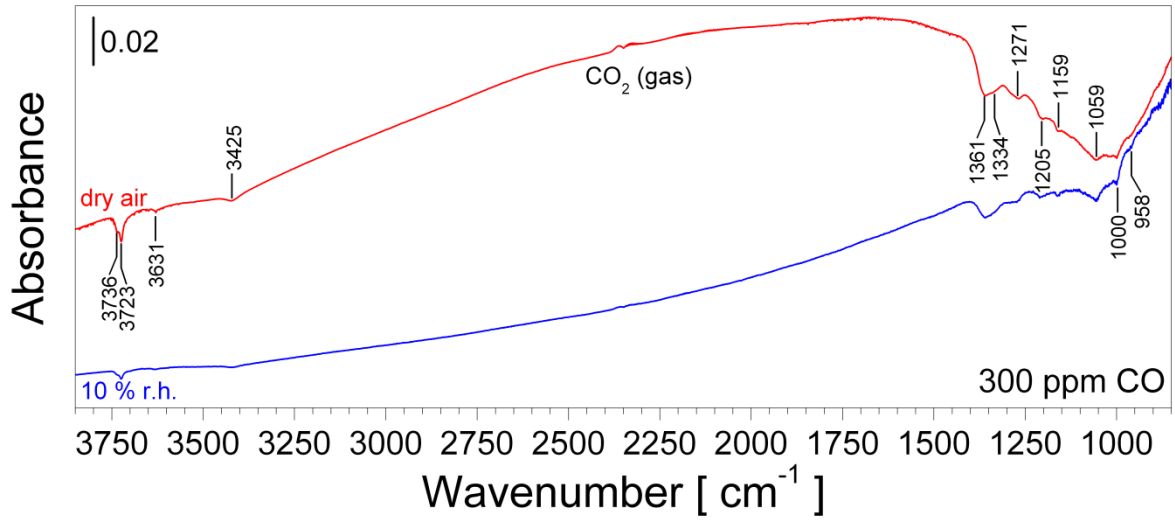

Figure 27. DRIFT spectra of undoped SnO_2 exposed to 300 ppm of CO in dry (red) and humid conditions, 10 % r.h. at 25 °C, (blue). The sensor temperature was 300 °C. The spectra were referenced to spectra recorded in dry or humid conditions, respectively.

According to the previously discussed findings, the resistance in dry air is controlled by a depletion layer, while in humid air, a switch from depletion to accumulation layer controlled conduction is observed [130]. However, in both conditions the exposure of CO affects the same bands, although the observed effects are stronger in dry conditions. Four decreasing bands are observed in the hydroxyl region; the bands at 3736, 3723 and 3631 cm^{-1} are assigned to isolated hydroxyl groups, while the broad band centred around 3425 cm^{-1} is assigned to interacting hydroxyl groups [74], [94]. The presence of gaseous CO_2 in the pores of the sensing layer is indicated by the two bands centred around 2348 cm^{-1} [74]; the bands correspond to the two branches of the antisymmetric stretch vibration of CO_2 [49]. Weak bands of gaseous CO are found at 2142 cm^{-1}; the bands are stronger at higher CO concentrations (see Supporting Figure 4). A series of decreasing bands is observed in the fingerprint region at 1361, 1334, 1271, 1205, 1159, 1059, 1000 and 958 cm^{-1}. Assigning the bands in the fingerprint region is rather complex, since bands of the C=O stretch vibrations of carbonates and carboxylates and hydroxyl deformation vibration of surface hydroxyl groups as well as bands of Sn-O species or their corresponding overtones are found in this spectral range [132]. The single processes responsible for the observed changes and the identification of the different bands in the fingerprint region will be discussed in the following paragraphs.

The decrease of the hydroxyl concentration during test gas exposure is explained by the equilibrium between hydroxyl groups with molecular water and surface oxygen [94]. In Reaction 20 the possible reactions for the formation of surface hydroxyl groups (Reaction 9 to Reaction 12) are simplified and adapted to the notation of Reaction 19.

$$H_2O_{gas} + O^{\alpha-} \leftrightharpoons 2OH_{ads} + \alpha \cdot e^- \qquad \textbf{Reaction 20}$$

$$O^{\alpha-} + CO \rightarrow CO_2 + \alpha \cdot e^- \qquad \textbf{Reaction 19}$$

In the absence of a test gas, an equilibrium between surface oxygen and molecular water with surface hydroxyl is established. An inevitable residual water vapour background of several ppm is present even in dry air. If surface oxygen is removed by a reaction with a test gas (Reaction 19), the equilibrium shown in Reaction 20 will be shifted to the right side (water vapour and surface oxygen). Consequently, the concentration of surface hydroxyl groups decreases due to the exposure to a reducing gas [94]. The appearance of CO_2 is directly associated with the gas reception; CO is oxidized on the SnO_2 surface and the concentration of the reaction product CO_2 increases. Isotopic labelled CO ($^{12}CO/^{13}CO$) and water (H_2O/D_2O) were used to differentiate the bands in the fingerprint region. If surface species contain carbon from CO or any proton, the corresponding isotopic labelling causes a shift of IR band related to this surface species. Bands that are not shifted due to isotopic labelling are related surface species that do not contain the targeted element. For possible species in the

fingerprint region – carbonates/carboxylates, hydroxyls and metal oxygen species – the performed $^{12}CO/^{13}CO$ and H_2O/D_2O exchange experiments the following effects are expected:

- IR bands of carbonates or carboxylates, which are due to reaction of CO with the surface, will be shifted by the $^{12}CO/^{13}CO$ exchange
- IR bands related to hydroxyls, namely OH stretch and OH deformation vibrations, will be shifted by the H_2O/D_2O exchange
- IR bands that decrease during the exposure to a reducing gas and that are neither shifted by the $^{12}CO/^{13}CO$ nor H_2O/D_2O exchange should be a reactive oxygen species

Table 2. Assignment of the IR bands on pristine based on literature and isotopic labelling experiments [42], [76]**.**

Wavenumber [cm^{-1}]	^{12}C-^{13}C exchange	H-D exchange	Assignment
3736	no shift	*shifted*	O-H stretch, isolated/terminal
3723	no shift	*shifted*	O-H stretch, isolated/terminal
3631	no shift	*shifted*	O-H stretch, isolated/terminal
3425	no shift	*shifted*	O-H stretch, interacting
2348	*shifted*	no shift	C=O stretch, CO_2 gas
2142	*shifted*	no shift	C=O stretch, CO gas
1361	no shift	no shift	Sn-O/lattice overtone
1334	no shift	no shift	Sn-O/lattice overtone
1271	no shift	no shift	Sn-O/lattice overtone
1205	no shift	no shift	Sn-O/lattice overtone
1159	no shift	no shift	Sn-O/lattice overtone
1059	no shift	no shift	Sn-O
1000	no shift	*shifted*	Sn-OH deformation*
958	no shift	*shifted*	Sn-OH deformation*

*The H-D exchange causes changes below 1000 cm^{-1} indicating that this region is dominated by Sn-OH deformation vibrations. A detailed assignment of the surface hydroxyls is given in the next chapter (Table 3).

In case of the $^{12}CO/^{13}CO$ exchange (Supporting Figure 4), no shift is observed in the fingerprint region, i.e. none of the IR bands are related to a carbonate or carboxylate species. For other undoped SnO_2 materials, which were prepared by different synthesis routes or prepared by the same aqueous sol-gel route and calcined at lower temperatures, the formation of carbonates is reported in literature [68], [74], [133]. If carbonates were found, their formation is not caused by a direct reaction of CO with the surface. It was shown that CO_2, i.e. the reaction product of the CO oxidation, forms carbonates. These carbonates have a very low impact on the resistance, i.e. carbonates are a spectator species, which are actively not involved in the gas sensing process [133]. Thus, only the bands of CO and CO_2 are affected by the $^{12}CO/^{13}CO$ exchange. The presence of $^{13}CO_2$ (2282 cm^{-1})

proofs that a fraction of ^{13}CO (2094 cm^{-1}) is oxidized, i.e. CO reacts on the SnO_2 surface, but does not form any of the expected reaction intermediates (carbonates/carboxylates).

In case of the H_2O/D_2O exchange, strong effects are observed in the DRIFT spectrum. The four O-H bands (3736, 3723, 3631 and 3425 cm^{-1}) are shifted to the O-D region; the corresponding O-D bands are found at 2754, 2746, 2678 and 2532 cm^{-1}, respectively. The calculated shift factors (0.737 to 0.739) correspond to shift factors reported in literature [94]. Also the bands at 1000 and 958 cm^{-1} are affected by the H_2O/D_2O exchange and thus should be Sn-OH deformation vibrations. The other bands in the finger print region are not affected by the exchange experiment. The bands at 1361, 1334, 1271, 1205, 1159 and 1059 are assigned Sn-O vibrations or respectively their overtones. This assignment is in line with corresponding bands reported in literature [42], [76]. The results of the exchange experiments and assignment of the bands are summarized in Table 2.

Consequently, the oxidation of CO on pristine SnO_2 involves lattice oxygen, i.e. takes place by a Mars-van-Krevelen mechanism [31], [134]. CO reacts with lattice oxygen forming CO_2, which desorbs and leaves an oxygen vacancy at the surface, i.e. the SnO_2 surface is reduced by CO (Reaction 21). For typical operation temperatures of SnO_2 based gas sensors (300 °C), the oxygen vacancy will be fully ionized, releasing the electrons to the conduction band [82]. Thus, the formed oxygen vacancies are considered to be electron donors. The surface is (re-)oxidized by atmospheric oxygen in a subsequent series of reactions. Such a reaction is imperative for a continuous CO_2 formation, which is experimentally observed [53], [121], [135], as well as the recovery of the gas sensor, i.e. the regeneration of the initial state of the surface. The re-oxidation of the surface by atmospheric, i.e. molecular, oxygen requires the adsorption and dissociation of O_2, which subsequently fills the oxygen vacancy and, thus, localizes electrons to form lattice oxygen. In the absence of experimental input, two possible reaction paths for the re-oxidation can be proposed based on the above mentioned theoretical calculations [56], [57]. Both paths start with the adsorption of molecular oxygen on an oxygen vacancy (Reaction 22). In analogy to the discussed reactions for the oxygen adsorption on SnO_2 (see 2.2.5.1. Adsorption of Oxygen, Reaction 2 to Reaction 6), the molecular oxygen dissociates and, by involving an oxygen vacancy and additional electrons, forms two lattice oxygen species (Reaction 23). Another possible reaction path is the reaction of the adsorbed molecular oxygen species with CO, forming CO_2 and lattice oxygen (Reaction 24). However, none of the intermediates of the re-oxidation is observed by DRIFTS.

$$O_O + CO \rightarrow CO_2 + V_O^{\alpha+} + \alpha \cdot e^- \qquad \textbf{Reaction 21}$$

$$V_O^{\alpha+} + \alpha \cdot e^- + O_2 \rightarrow (O_2)_o \qquad \textbf{Reaction 22}$$

$$(O_2)_o + V_O^{\alpha+} + \alpha \cdot e^- \rightarrow 2O_O \qquad \textbf{Reaction 23}$$

$$(O_2)_o + CO \rightarrow CO_2 + O_O$$ **Reaction 24**

DRIFT spectra recorded during the exposure of H_2 in dry and humid conditions (Figure 28) show similar effects on SnO_2 as CO exposure; namely a decrease of the hydroxyl and lattice oxygen species. As expected for H_2 exposure, the bands assigned to CO and CO_2 are not found in the DRIFT spectra. The bands observed in the fingerprint region during H_2 exposure are congruent with the bands observed during CO exposure and, like for CO exposure, the effects are stronger in dry than in humid conditions. Consequently, the oxygen species involved in the CO oxidation are also involved in the reaction with H_2. Analogous to the reception of CO, the reception of H_2 takes place by the oxidation of H_2 to H_2O, which consumes lattice oxygen and leads to the formation of oxygen vacancies (Reaction 25).

$$O_O + H_2 \rightarrow H_2O + V_O^{\alpha+} + \alpha \cdot e^- \quad \textbf{Reaction 25}$$

The re-oxidation of the SnO_2 surface is expected to take place by reaction steps similar to the ones described in case of CO exposure.

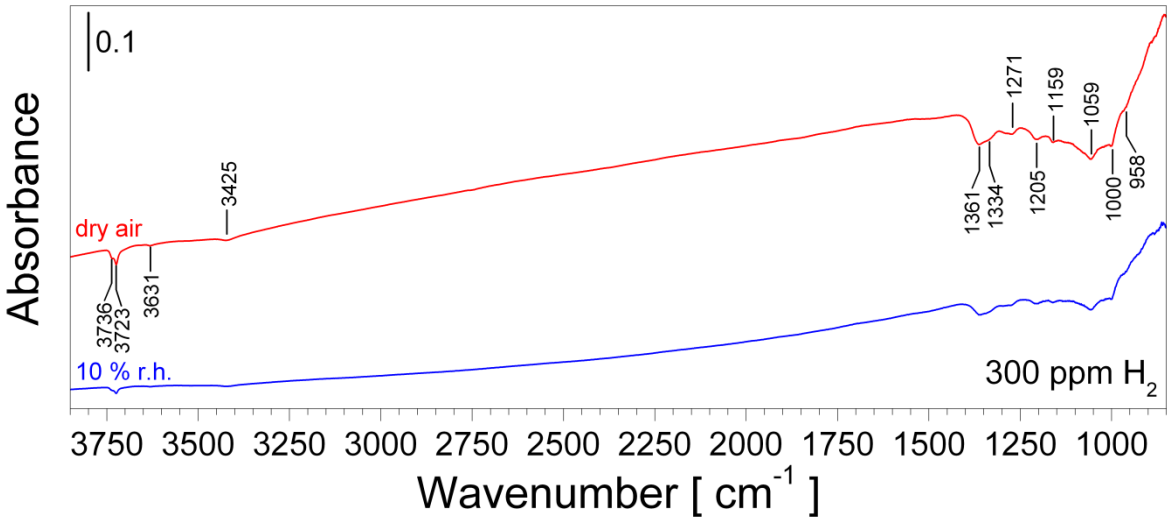

Figure 28. DRIFT spectra of undoped SnO_2 exposed to 300 ppm of H_2 in dry (red) and humid conditions, 10 % r.h. at 25 °C, (blue). The sensor temperature was 300 °C. The spectra were referenced to spectra recorded in dry or humid conditions, respectively.

In the case of CO and H_2 exposure in atmospheres containing ambient-like concentrations of O_2, i.e. 20.5 vol%, the same surface processes are observed in dry and humid conditions. The reception of both gases takes place by the oxidation of the test gases via a Mars-van-Krevelen mechanism, creating oxygen vacancies, which act as electron donors. Whether and how this gas reception mechanism is applicable to test gas exposures in the absence of oxygen is not clear. Experiments performed in the absence of oxygen give insight in the reaction of O_2 or CO dosed in N_2 (Figure 29). The exposure of O_2 causes an increase of the lattice oxygen bands, i.e. the oxygen species that react with CO and H_2, are formed by atmospheric oxygen. The increase of the hydroxyl groups is explained

by the equilibrium described in Reaction 20. Vice versa, the exposure of CO in the absence of oxygen causes a decrease of the IR bands at 1361, 1334, 2171, 1205 and 1059 cm^{-1}. These bands are the same bands that are involved in the reaction of CO and H_2 in air. The CO exposure causes no formation of CO_2 or related surface species, e.g. carbonyls, carboxylates or carbonates. Since the theoretical calculations indicate, that CO adsorbed on a Sn surface site has a rather low electronic impact [57], a high surface concentration of these species would be necessary to cause the strong resistance changes in the absence of oxygen [129]. The absence of any CO-related surface species eliminates the existence of a CO-related electron donor. These observations suggest, that in air and in the absence of oxygen the same reactions take place at the pristine SnO_2 surface; namely a Mars-van-Krevelen-like oxidation of the test gas, which reduces the SnO_2 surface. Thus, the same electron donor species are formed in dry and humid air as well as in the absence of oxygen.

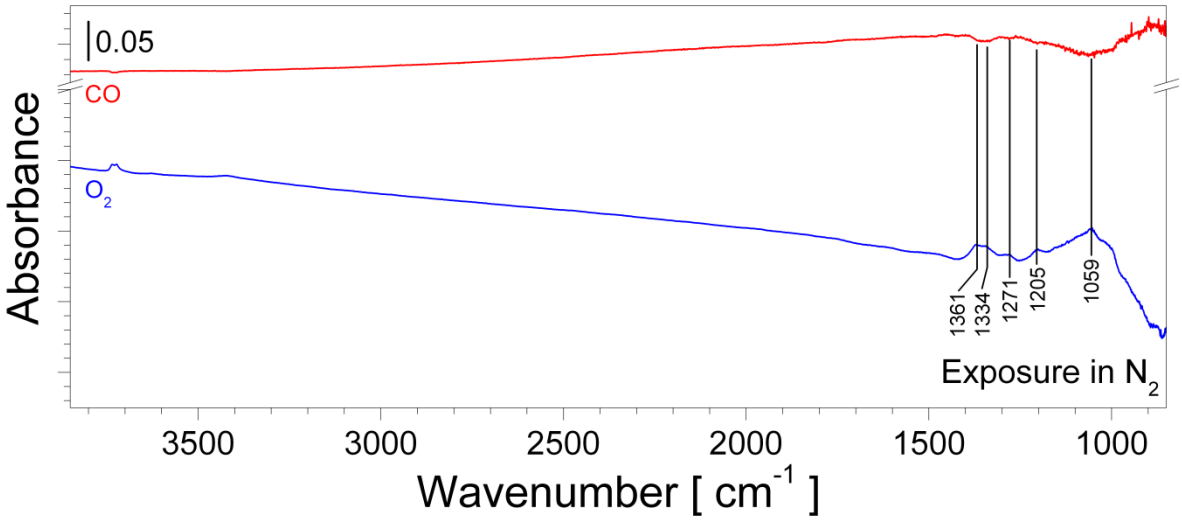

Figure 29. DRIFT spectra of undoped SnO_2 exposed to 300 ppm O_2 (blue) or 300 ppm of CO (red) in pure N_2 (residual oxygen: 2.7 ppm) The sensor temperature was 300 °C. The spectra were referenced to spectra recorded in dry or humid conditions, respectively.

Taking CO as an example, the reduction and re-oxidation of pristine SnO_2 is summarized as a reaction scheme in Figure 30. Reaction step 1 (Reaction 21) is the reduction of SnO_2 – or vice versa the oxidation of CO to CO_2. The subsequent re-oxidation of the surface is expected to proceed in two steps, the adsorption of molecular oxygen (Reaction 22) and subsequent dissociation and ionization forming lattice oxygen (Reaction 23 or Reaction 24). Assuming that the re-oxidation is the rate limiting step of this CO oxidation, a certain concentration of oxygen vacancies will be formed for a given CO and O_2 concentration. Based on this model for the gas reception, the trend observed for the sensor signals in different oxygen backgrounds, namely increased sensor signals with decreasing oxygen concentrations [129], is explained as follows: In air, the oxygen vacancies created by CO oxidation will be easily filled by atmospheric oxygen, i.e. the re-oxidation dominates and only a low oxygen vacancy concentrations is found in equilibrium conditions. If the oxygen concentration is

decreased, the re-oxidation will get less dominant and the oxygen vacancy concentration increases. The increased concentration of electron donors explains the increased sensor signals. In the absence of atmospheric oxygen, the re-oxidation is limited to the residual oxygen concentration and comes almost to a standstill, giving a strong rise to the oxygen vacancy concentration and consequently to the sensor signals. The observed dramatic decrease of reaction products (CO_2, H_2O) in the exhaust gas [129], [133] is in line with this explanation model: During the initial phase of the test gas exposure, the reactive oxygen species are consumed, but not renewed due to the lack of re-oxidation. Consequently, the oxidation of the test gases comes almost to a standstill and formation of reaction products strongly declines.

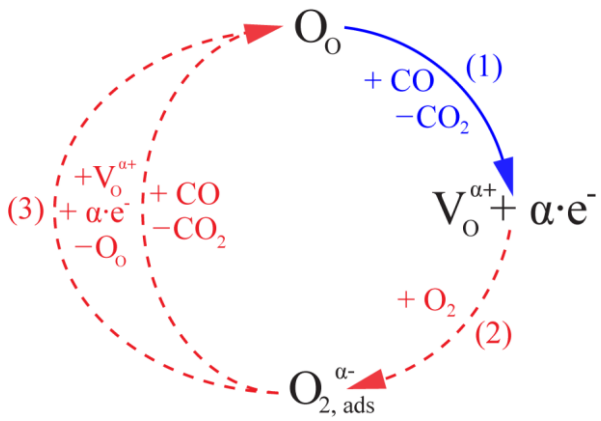

Figure 30. Proposed surface chemistry model for the reception of small reducing gases, e.g. CO, H_2, on pristine SnO_2 surfaces. The formation of oxygen vacancies, i.e. electron donors, depends on the interplay of reduction of the surface (step 1, blue) and the re-oxidation of the surface (step 2 and 3, red).

The above described observations and the proposed gas reception model explain the switch from depletion layer to accumulation layer controlled transduction in application-relevant conditions, namely in humid air. Water vapour, as such, decreases the concentration of reactive oxygen species (Supporting Figure 5), presumably by forming hydroxyl groups [68], [94], [135]. Thus, in humid air, the concentration of reactive oxygen species is initially decreased and a lower fraction of the reducing test gas is able to react with the surface, since less reaction partners (reactive oxygen species) are available. Because the absolute water vapour concentration is typically one order of magnitude higher than the test gas concentration, the interaction of water vapour with the surface inhibits the interaction of the test gas with the surface, i.e. decreasing the reactivity. In conclusion, the interference of water vapour with the gas reception mechanism leads to decreased sensor signal (Figure 26) and less changes of the surface due to test gas exposure in humid air (Figure 27 and Figure 28). If water vapour not only interferes with the reducing test gases but also affects the oxygen adsorption, e.g. by hindering the interaction of molecular oxygen with the surface, the (re-)oxidation will be affected by the presence of water vapour. Assuming, that the interfering effect of H_2O is stronger for O_2 than a reducing gas like CO, the reduction of the surface can cause an oxygen vacancy concentration high enough to cause the formation of an accumulation layer.

However, since the surface is already reduced by the interaction with water vapour, the resulting sensor signal, i.e. relative resistance change, caused by the exposure to a reducing gas is lower than the one in dry conditions.

5.2.2. Operando UV/vis-DRS measurements

The involvement of lattice oxygen in the gas reception raises the question, whether only lattice oxygen of the SnO_2 surface region or also that of the bulk is involved. Extrapolating the oxygen mobility obtained from high temperature measurements (700 to 1000 °C) on single crystal samples to the operation temperature of SnO_2-based gas sensors (300 °C), the characteristic time for the chemical oxygen diffusion is within seconds [136], [137]. In contrast, isotopic labelling experiments utilizing $^{18}O_2$ indicate, that below 425 °C (700 K) bulk oxygen of undoped SnO_2 is not exchanged with atmospheric oxygen, while surface oxygen species are exchanged in this temperature range [63], [138]. Thus, it is not clear whether the whole SnO_2 material or only the surface is reduced by the interaction with a reducing gas at 300 °C.

The reduction of SnO_2 causes an increased absorption in the visible range [139]. This observation was made for very small SnO_2 nanoparticles (average diameter 3 nm) during reduction in vacuum at temperature between 200 and 500 °C; a reversible decrease of the absorption in the visible range is observed during oxygen exposure above 200 °C [139]. In the case of such small nanoparticles a clear-cut separation of surface and bulk region is rather impossible and the reduction of the whole grain is expected. For the SnO_2 material studied in this work (average grain diameter of 99 nm, see Figure 24) the existence of a bulk region is plausible. If oxygen from the bulk region is involved in the oxidation of reducing gases in the absence of atmospheric oxygen, similar changes in the visible range as for the very small nanoparticles should be observed. If only the surface region is affected by this reaction, rather small changes in the visible range are expected. In order to experimentally assess this question, operando UV/vis-DRS experiments were performed, including CO exposure in air as well as O_2 and CO exposure in N_2. The reflectance spectra are shown in Figure 31.

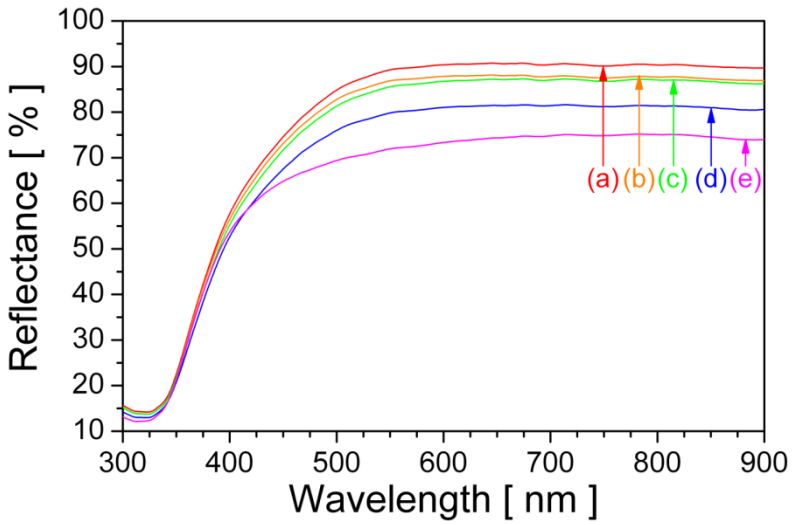

Figure 31. UV/vis reflectance spectra of undoped SnO_2 recorded in different atmospheres at a sensor temperature of 300 °C: Dry air (a), 300 ppm CO in dry air (b), 3000 ppm O_2 in N_2 (c), pure N_2 (d) and 300 ppm CO in N_2 (e).

Indeed, the absorbance in visible range changes due to gas exposure. The lowest absorption is found in dry air, while the highest measured absorption is recorded during CO exposure in N_2. The other atmospheres follow this trend sohe absorption in the visible range increases with more reducing conditions. All observed changes in the absorption are reversible. A strongly pronounced increase of the absorption, as reported for the very small SnO_2 nanoparticles [139], is not observed. However, if the same experiment is done with an undoped SnO_2 material with a grain diameter of approximately 10 nm a strong increase of the absorption in the visible range is observed [98]. The correlation of the surface area, which is reciprocal proportional to the grain diameter, and the absorption increase caused by CO exposure in the absence of oxygen indicates, that at 300 °C the reduction takes place only at the surface region of SnO_2.

The UV/vis-DRS measurements and the above cited isotopic labelling experiments exclude a significant contribution of bulk oxygen to the gas reception process. Consequently, the superficial reduction of SnO_2 will only affect the electron donor concentration at the surface and the transduction model based on depletion and accumulation layer should be valid [52], [53], [80], [130].

5.2.3. Proposed model for the gas reception mechanism on pristine SnO_2

In summary, the gas sensing mechanism of undoped SnO_2 in dry and humid air, as well as in the absence of oxygen is based on the interplay of the reduction of the surface, i.e. reaction of the reducing gas with lattice oxygen of the SnO_2 surface, and the re-oxidation of the surface by atmospheric oxygen. Since the reduction is superficial, solely the electron donor concentration at the surface is influence by the reduction or oxidation reactions. Assuming, that in the absence of reactive gases, like O_2, CO, H_2, H_2O, the compositions of the surface and bulk of the SnO_2 grain are the same, the same concentration of electron donors is found. Thus, in pure nitrogen (Figure 32a) the bands at

the surface are flat. This assumption is in agreement with the experimental determination of the flat band situation, i.e. the transition from a depletion layer (upwards band bending) to an accumulation layer (downwards band bending) [53], [81], [130].

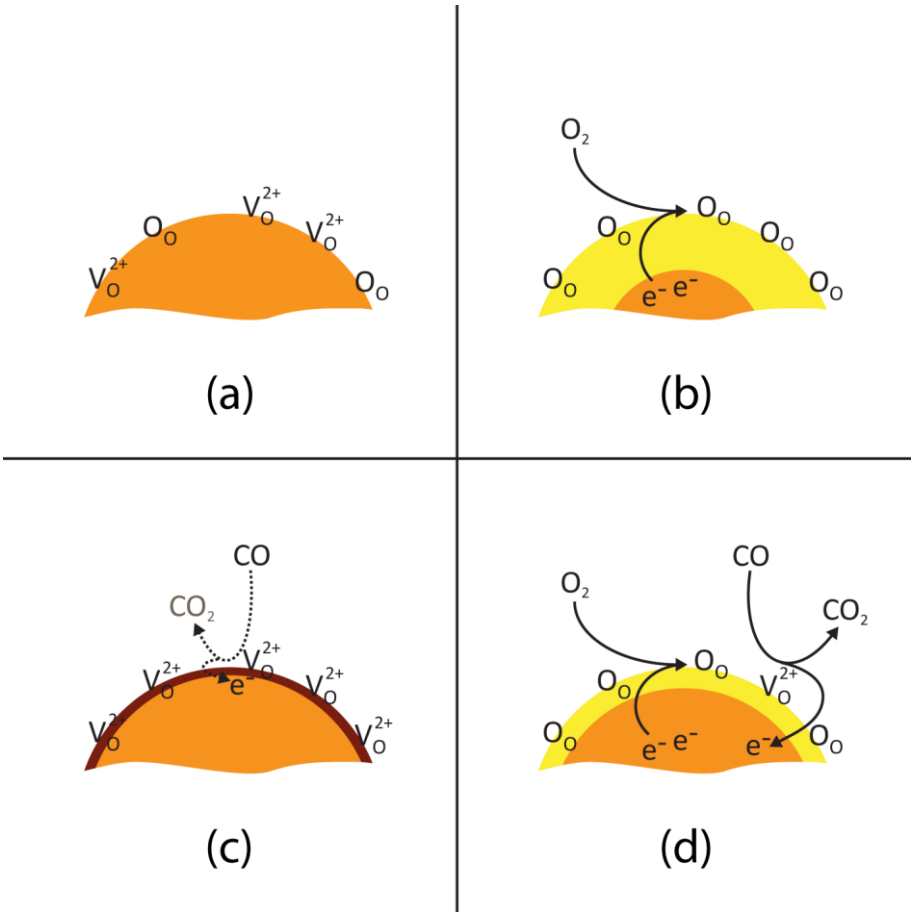

Figure 32. Proposed relation of the SnO_2 surface composition and space charge layer as a function of the atmospheric composition: Pure N_2 (a), O_2-N_2 mixtures or air (b), CO exposure in N_2 (c) and CO exposure in air (d). Depending on the atmospheric composition a depletion layer (yellow) or accumulation layer (brown) is formed; the electronic situation of the bulk is coloured in orange. In order to simplify the representation, only the reactive oxygen sites are shown in the graphics.

For an undoped SnO_2-based gas sensor at an operation temperature of 300 °C the following situation will be found: If oxygen is present in the atmosphere (Figure 32b), oxygen vacancies at the surface are filled and charge is trapped at the formed lattice oxygen species, thus the donor concentration at the surface is lower than the one in the unaffected bulk region. This process causes a depletion layer, i.e. an upwards band bending, and consequently the resistance of the sensing layer increases. If in the absence of atmospheric oxygen CO is present in the atmosphere (Figure 32c), surface oxygen reacts with CO, but due to the lack of re-oxidation the surface gets strongly reduced. The electron donor concentration at the surface is higher than in the bulk and an electron accumulation layer is formed (downwards band bending). If CO and O_2 are present in the atmosphere (Figure 32d), the surface oxygen formed by atmospheric oxygen will be removed during the oxidation of CO to CO_2; due to the continuous re-oxidation of the surface, only a small fraction of oxygen is removed in

equilibrium conditions. Consequently, the dynamic interplay of surface reduction and re-oxidation determines the surface oxygen vacancy concentration. For high oxygen concentration and in the absence of an interfering gas, e.g. in dry air, this will lead to a decrease of the electron depletion layer. However, in lower oxygen backgrounds or due to an interfering gas like H_2O, the surface oxygen vacancy concentration is higher than the one in the bulk, i.e. an accumulation layer is formed (Figure 32c). This interplay of surface reduction and re-oxidation should be valid for reducing gases with a rather simple surface chemistry like CO or H_2, which do not form reaction intermediation at the surface. However, for reducing gases with a complex surface chemistry, e.g. volatile organic compounds, the formation of intermediate species at surface is expected. If these intermediates have to be further oxidized to be removed from the surface, the situation may differ and this model is no longer applicable.

5.3. Surface Chemistry of Water Vapour and Hydroxyl Groups

Water vapour is an omnipresent interfering gas in ambient conditions. A great deal of research has been dedicated to understand the interaction of water vapour with SMOX [12], [52], [59], [68], [94], [140], and to create materials with a gas sensing performance, which is less influenced by the water vapour concentration [8], [9], [11], [20], [102], [141], [142]. Water vapour as such is a reducing gas and the common model assumes, that water reacts with surface oxygen forming hydroxyl groups and oxygen vacancies [12], [52]. Indeed, the DRIFT spectrum recorded during H_2O exposure (Supporting Figure 5) indicates a decrease of the Sn-O species. However, instead of an increase of the hydroxyl concentration, a decrease of the overall hydroxyl group bands is also observed. Nevertheless, for differently prepared SnO_2 gas sensing materials measured under the same conditions, an increase of the IR bands assigned to rooted and interacting hydroxyl groups is observed. Also, the intensities of pre-existing, isolated hydroxyl groups decrease, presumably due to the interaction of the formed hydroxyl groups with the pre-existing ones [68], [133]. This indicates the formation of additional hydroxyl groups on these materials. Thus, the question arises why the hydroxyl band intensity decreases for this material due to the exposure to water vapour and which factors influence the adsorption of water vapour.

The effect of temperature on the adsorbed water vapour species is well reported in literature and is likely to influence the adsorption of H_2O on SnO_2 [52], [59], [64]. To study the effect of temperature on the chemistry of water vapour on SnO_2, a series of DRIFT spectra was recorded at different temperatures: room temperature, 150 °C, 250 °C, 300 °C and 400 °C. The DRIFTS experiments are complemented by additional in-situ DRIFTS, CO sensing and CO conversion measurements between 100 and 400 °C, measured in 50 °C steps. Freshly prepared sensors were measured to avoid effects of measurement history, especially during the measurements at lower temperatures.

5.3.1. DRIFTS study on the temperature dependence of water adsorption

The DRIFT spectrum recorded during H_2O exposure at room temperature (Figure 33, red spectrum) shows a decrease of all isolated OH groups (see highlighted bands in Figure 33), while the broad band (3700-2600 cm^{-1}), which is related to interacting OH groups, increases. Corresponding to the decreased OH stretch vibrations, the Sn-OH deformation vibrations at 979, 963 and 895 cm^{-1} are also decreased. Furthermore, the increase of a band at 1637 cm^{-1} indicates the formation of physisorbed water at the SnO_2 surface [66]. Additional information on the hydroxyl composition of the surface is obtained from the D_2O spectrum referenced to dry air (Figure 33, blue spectrum). The exchanged, i.e. decreasing, bands in the hydroxyl region reflected the hydroxyl composition in dry air while the bands formed in the OD range correspond to the hydroxyl bands present in humid conditions. The additional benefit of the D_2O spectrum, besides the verification of the OH band assignments due to

the shift values, is the identification of OH bands that are only weakly influenced by water vapour. They are, in this case the O-H stretch vibration at 3480 cm^{-1} and the presumed corresponding Sn-OH deformation mode at 1264 cm^{-1}. Combining the information from the H_2O and D_2O spectra, the following situation is found at room temperature: In dry air, the surface is already covered with various isolated as well as interacting hydroxyl groups. If water vapour is present in the atmosphere, the bands of the isolated hydroxyl groups decrease, due to the interaction with molecular water, which attenuates the OH vibrations [143], [144], thus causing an increase of the broad band assigned to interacting hydroxyl groups. The massive increase of this broad band and the band at 1637 cm^{-1} are caused by physisorbed water. In conclusion, at room temperature the adsorption of molecular water dominates; molecular adsorption involves weakly bound physisorbed species and water molecules which coordinate via H-bonds with surface hydroxyl or oxygen species, referred as associative water adsorption.

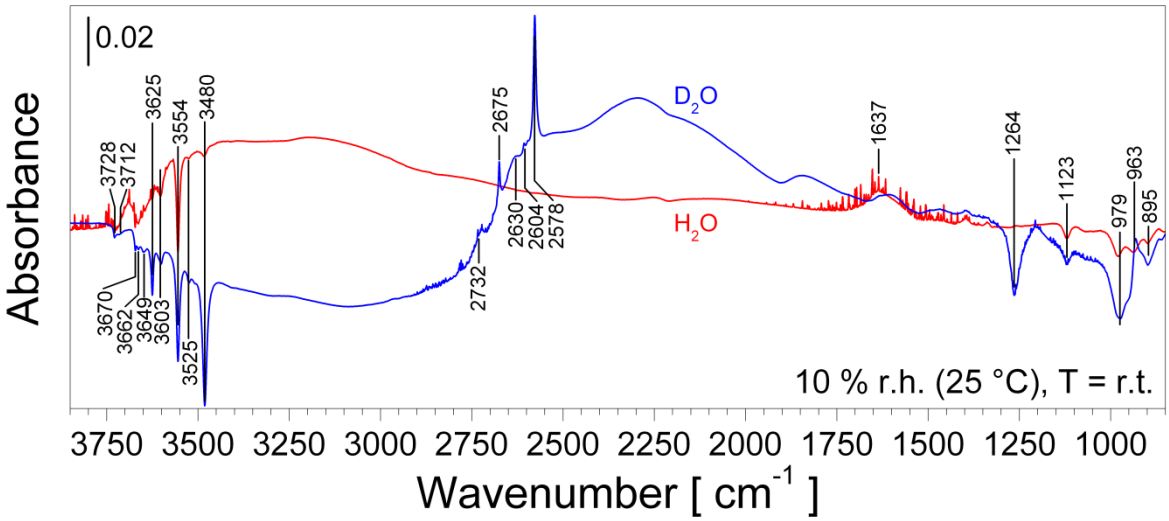

Figure 33. DRIFT spectra of undoped SnO_2 exposed to H_2O in dry (red) and D_2O (blue) recorded at room temperature. The water concentration was 10 % r.h. at 25 °C. The spectra were referenced to a spectrum recorded in dry. The corresponding isotopic exchange spectrum is shown in Supporting Figure 6.

The spectra recorded at 150 °C (Figure 34) and 250 °C (Figure 35) show a decrease of the hydroxyl bands in dry air with increasing temperature. At both temperatures, the exposure of water vapor causes a decrease of the isolated hydroxyl groups at 3726, 3671, 3595, 3555 and 3479 cm^{-1}. The bands at 3711, 3626 and 3522 cm^{-1} appear not to be affected by the presence of water vapour. The spectra show no indication of water physisorption. The H_2O spectrum recorded at 150 °C shows no noticeable change of the broad adsorption band related to interacting hydroxyl groups. However, it is not clear whether there is no change in the concentration of interacting hydroxyl groups, or the formation of additional interacting hydroxyl groups is compensating it. The spectrum recorded at 250 °C shows a low decrease of the band related to interacting hydroxyl groups. However, at both

temperatures, the D_2O spectra clearly show an exchange of interacting OH groups, i.e. interacting OH groups are present in dry air and in sum not (150 °C) or little (250 °C) affected by water vapour.

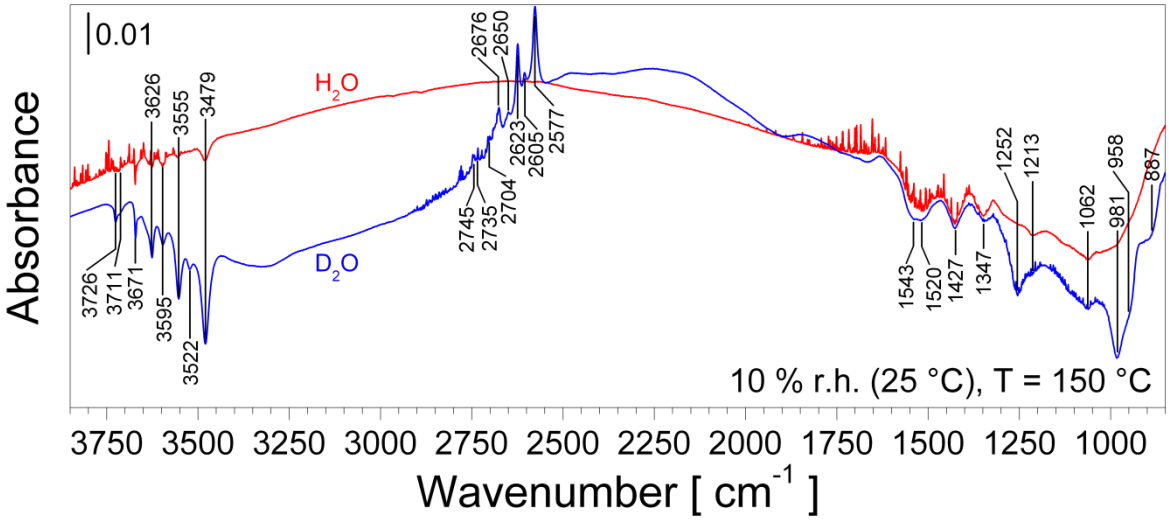

Figure 34. DRIFT spectra of undoped SnO_2 exposed to H_2O in dry (red) and D_2O (blue) recorded at an operation temperature of 150 °C. The water concentration was 10 % r.h. at 25 °C. The spectra were referenced to a spectrum recorded in dry. The corresponding isotopic exchange spectrum is shown in Supporting Figure 7.

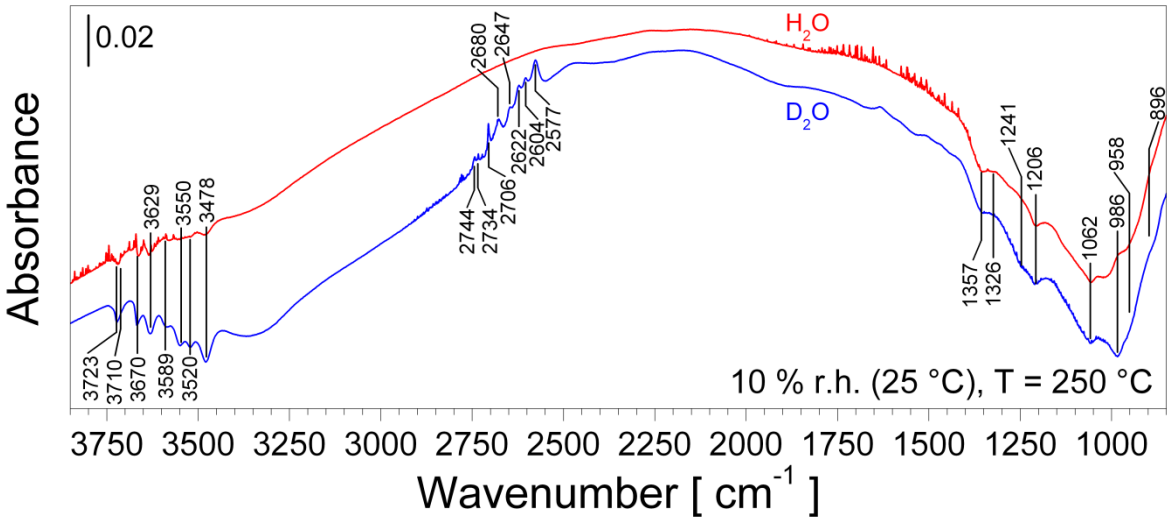

Figure 35. DRIFT spectra of undoped SnO_2 exposed to H_2O in dry (red) and D_2O (blue) recorded at an operation temperature of 250 °C. The water concentration was 10 % r.h. at 25 °C. The spectra were referenced to a spectrum recorded in dry. The spectra were referenced to a spectrum recorded in dry. The corresponding isotopic exchange spectrum is shown in Supporting Figure 8.

A series of decreased Sn-O related bands (1357-1326, 1213-1206 and 1062 cm^{-1}) is found in the fingerprint region. Since no formation of additional hydroxyl groups is observed, the decrease is assumed to be rather related to the formation of H-bonds (Reaction 8) than to a reaction with H_2O forming hydroxyl groups (Reaction 9 to Reaction 12). At 150 °C a series of additional decreasing bands is observed at 1543, 1520 and 1427 cm^{-1}; these bands are not exchanged by D_2O and are assigned to overtones of Sn-O-Sn species [76]. The D_2O exposure reveals Sn-OH deformation vibrations at 1252, 981, 958 and 887 cm^{-1} for 150 °C and at 1241, 986, 958 and 896 cm^{-1} for 250 °C.

The absence of physisorption is in agreement with previous TPD and IR studies, which determined that maximum of the desorption of physisorbed water is at 100 °C [59], [64], [66]. The decrease of OH and Sn-O bands at the same time, suggests rather an associative adsorption of molecular water by the formation of H-bonds than the formation of new hydroxyl groups. In literature, the range of molecular water adsorption is reported up to 200 °C [52], i.e. associative adsorption at 250 °C is still likely.

The spectra recorded at 300 °C (Figure 36) show distinct differences to the previous temperatures. The D_2O spectrum reveals a strong decrease of the hydroxyl groups present in dry air; the bands at 3589 and 3550 cm^{-1} are missing and the band at 3668 cm^{-1} is only visible as a weak shoulder. In the presence of water vapour the hydroxyl bands present in dry air are either decreasing (3723 and 3627 cm^{-1}) or remain unaffected (3520 and 3478 cm^{-1}). However, the bands that were found to be removed at 300 °C, 3668, 3589 and 3550cm^{-1}, show an increase in the presence of water vapour. The broad band related to interacting hydroxyls is almost not affected by water vapour; the increased band centred around 3325 cm^{-1} indicates a possible low increase of interacting hydroxyls. The formation of hydroxyl bands, which are not present in dry air, clearly shows a dissociative adsorption of H_2O, i.e. the reaction of H_2O with surface oxygen to form hydroxyl groups. The attenuation of the bands of the pre-existing OH groups is related to an interaction with water molecules as well as the new formed hydroxyl groups.

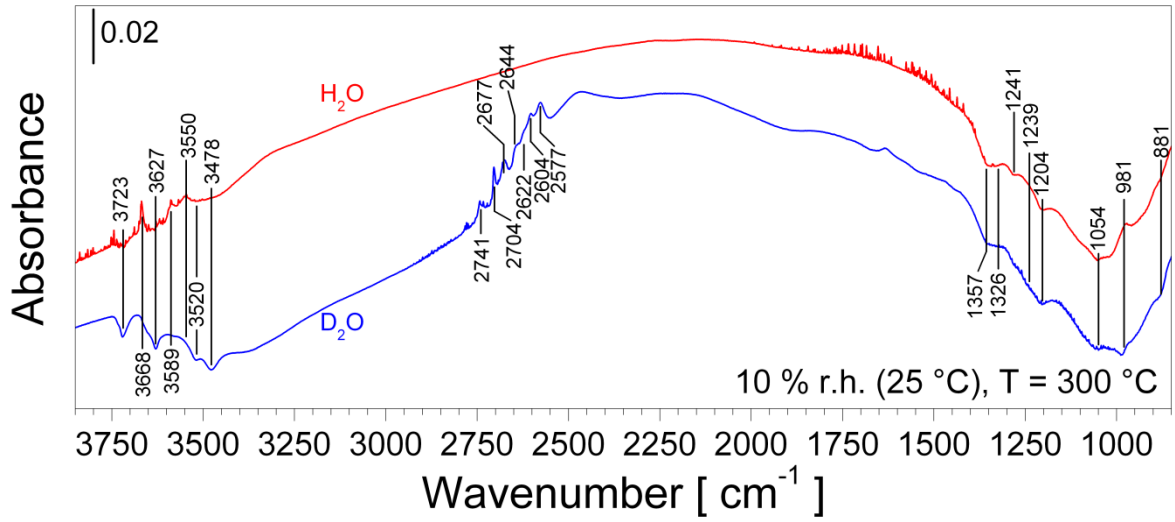

Figure 36. DRIFT spectra of undoped SnO_2 exposed to H_2O in dry (red) and D_2O (blue) recorded at an operation temperature of 300 °C. The water concentration was 10 % r.h. at 25 °C. The spectra were referenced to a spectrum recorded in dry. The spectra were referenced to a spectrum recorded in dry. The corresponding isotopic exchange spectrum is shown in Supporting Figure 9.

The differences of the spectra recorded at 300 °C during the temperature study of water adsorption (Figure 36) and recorded during the study to determine the donor species (Supporting Figure 5) is clearly seen in the trends observed for H_2O exposure, as well as in the composition of hydroxyl

groups: the previously discussed spectrum (Supporting Figure 5) does not show OH bands at 3589, 3550, 3520 and 3478 cm^{-1}. The differences are most likely related to an aging effect because in experiments to determine the nature of the donor species the used sensor was previously measured several times in various conditions. For the temperature study a set of new sensors was used. This explanation is confirmed by the comparison of spectra of the older sensor batch measured at different points of time (Supporting Figure 10). Initially, the spectrum recorded from an old sensor is similar to the one recorded from a freshly prepared sensor. The spectra recorded afterwards show less OH bands and correspond to the spectrum in Supporting Figure 5. Thus, an aging of the undoped SnO_2 surface has a strong effect on the hydroxyl composition and reaction with water vapour; however, a systematic study of the aging effect is beyond the scope of this work.

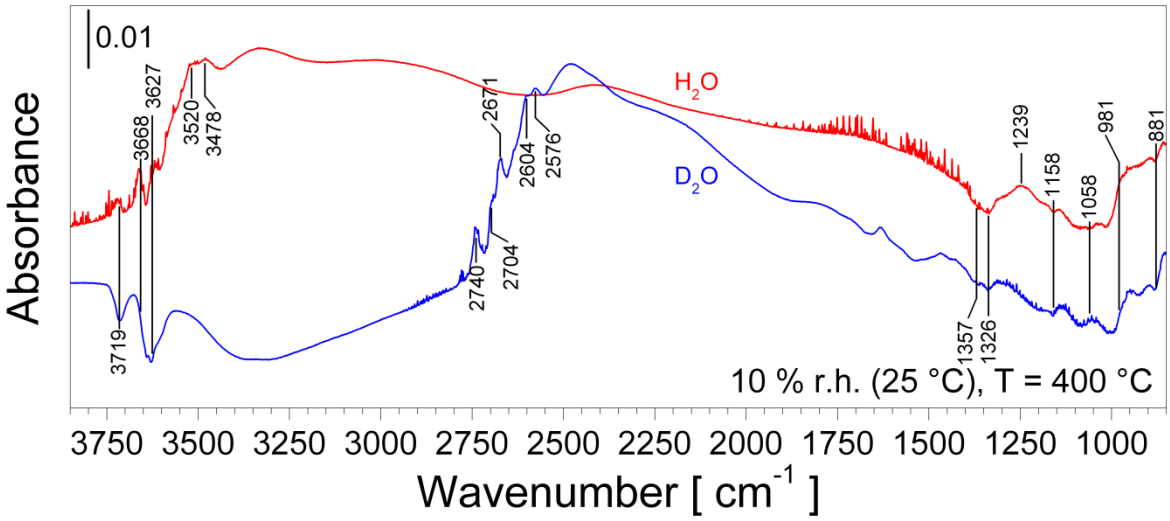

Figure 37. DRIFT spectra of undoped SnO_2 exposed to H_2O in dry (red) and D_2O (blue) recorded at an operation temperature of 400 °C. The water concentration was 10 % r.h. at 25 °C. The spectra were referenced to a spectrum recorded in dry. The corresponding isotopic exchange spectrum is shown in Supporting Figure 11.

At 400 °C the spectra reveal a situation, which is very different from the one found at lower temperatures (T ≤ 250 °C). In dry air the number of isolated hydroxyl groups strongly decreases and only two bands are found at 3719 and 3627 cm^{-1}. Compared to lower temperatures the broad band related to interacting hydroxyl also decreases. In the presence of water vapour a strong increase of the interacting hydroxyl groups and the formation of hydroxyl bands at 3668, 3520 and 3478 cm^{-1} (OH stretching vibration), and 1239 cm^{-1} (Sn-OH deformation vibration) is observed. Since the OH stretching modes at 3520 and 3478 cm^{-1} and the Sn-OH deformation mode (1239 cm^{-1}) are absent in dry air but increase in the presence of water vapour, it can be deduced that these bands belong to the same hydroxyl species, which are, according to the position of OH stretch vibration band, rooted hydroxyls. The intensity of the pre-existing OH bands (3719 and 3627 cm^{-1}) decreases due to water vapour exposure. The effect of water vapour exposure at 400 °C is dominated by the dissociative adsorption of water, which causes a strong increase of hydroxyl groups. The spectrum recorded

during H_2O exposure at 400 °C (Figure 37) shows a similar increase of hydroxyl groups, as reported for different SnO_2 materials measured at 300 °C [68], [133]. Based on this observation it can be concluded, that the properties of SnO_2 and the operation temperature of the gas sensor have a strong influence on the interaction of water vapour with the SnO_2 surface.

Table 3. Assigned hydroxyl related absorption bands found at different temperatures in dry air and the effect of water vapour. The hydroxyl bands were assigned according to literature [68], [76], [94], [108], [122]**.**

Wavenumber [cm^{-1}]	r.t.	150 °C	250 °C	300 °C	400 °C	Assignment
3728-3719	P, -	P, -	P, -	P, -	P, +	terminal hydroxyl group
3712	P, -					terminal hydroxyl group
3671-3668	P, -	P, -	P, -	P, +	P, -	terminal hydroxyl group
3662	P, -					terminal hydroxyl group
3649	P, -					terminal hydroxyl group
3627-3625	P, -	P, -	P, -	P, -	P, -	terminal hydroxyl group
3603	P, -					terminal hydroxyl group
3589				N, +		terminal hydroxyl group
3554	P, -	P, =	P, -	N, +		rooted hydroxyl group
3525-2520	P, -	P, =	P, -	P, -	N, +	rooted hydroxyl group
3480-3478	P, -	P, -	P, -	P, -	N, +	rooted hydroxyl group
3600-2500	P, +	P, =	P, -	P, +	P, +	Interacting hydroxyl groups
1637	N, +					H_2O (physisorbed)
1264-1239	P, =	P, =	P, =	P, =	N, +	Sn-OH (rooted)
986-979	P, -	P, =	P, +	P, +	P, +	Sn-OH
963-958	P, -	P, =	P, =			Sn-OH
896-881	P, -	P, =	P, +	P, =	P, -	Sn-OH

P: pre-existing group, N: not pre-existing group
- : decreased during water exposure, = : apparently not affected by water vapour, + : increased during water exposure

The results of the DRIFT spectra recorded at different temperatures are summarized in Table 3. Depending on the temperature, the following trends can be identified:

- Physisorbed water is only observed at room temperature in humid conditions. The absence of physisorbed water for T ≥ 150 °C is supported by TPD measurements, which report the corresponding desorption peak around 50 to 100 °C [59], [64].
- With increasing temperature, the number of hydroxyl groups decreases. The strong decrease of hydroxyls above 250 °C, best observed in dry air, correlates well with the onset of the second water desorption peak observed in TPD measurements, which has a maximum between 400 to 450 °C [59], [64]. This desorption peak is explained by the desorption of

dissociativly adsorbed water, i.e. the combination of two hydroxyls forming molecular water and surface oxygen (see Reaction 9) [65].

- At 150 and 250 °C the presence of water vapour attenuates the hydroxyl stretching vibration. This effect is best explained by the formation of H-bonds between the water molecules and the surface hydroxyl groups [143], [144].
- At 300 °C and 400 °C the exposure of water vapour causes an increase of hydroxyl groups on the surface. The effect gets stronger if less pre-existing hydroxyl groups are present, i.e. at higher temperatures.

5.3.2. Proposed model for the interaction of water with the SnO_2 surface

According to the DRIFT spectra recorded at different temperatures, there are three different regions of interaction between water vapour and the SnO_2 surface (see Figure 38). At low temperatures (T < 100 °C) the physisorption of water dominates. If the temperature is too high for physisorption, but too low to remove surface hydroxyl groups, water forms H-bonds with the surface hydroxyl groups and the associative adsorption of water dominates. If the temperature is high enough to remove hydroxyl groups, an increase of the water vapour concentration results in the formation of hydroxyl groups, i.e. the dissociative adsorption of water dominates and the concentration of surface hydroxyl groups depends on the concentration of water vapour in the atmosphere.

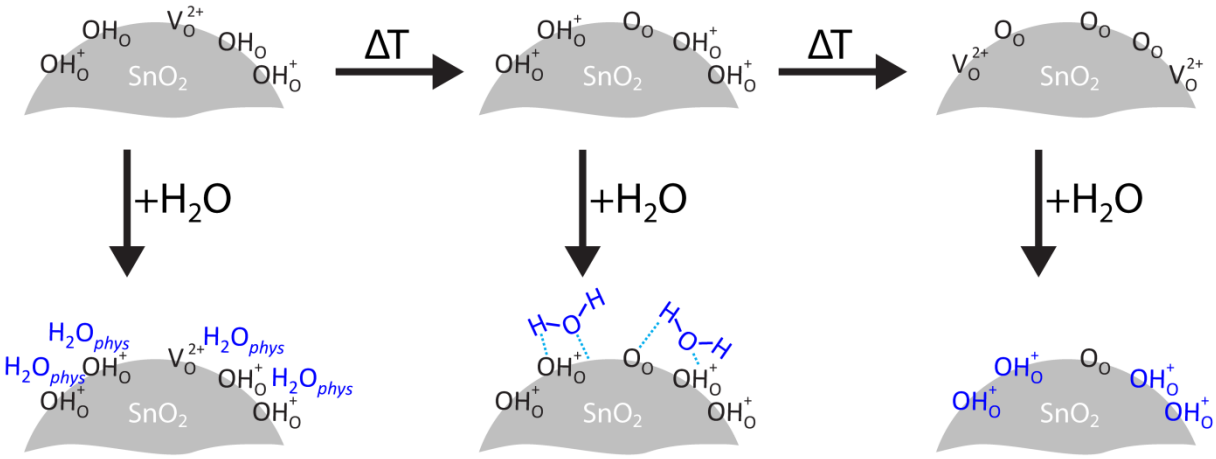

Figure 38. Schematic representation of possible interactions of water vapour with the SnO_2 surface chemistry at different temperatures: Dominant physisorption at low temperatures (left), associative adsorption of water due to H-bond formation at intermediate temperatures (middle) and dissociative adsorption of water forming hydroxyl groups at high temperatures (right). The situation of the surface in dry air is shown in the top row, the situation in the presence of water vapour in the bottom row.

In addition to temperature itself, there are further parameters that influence the adsorption of water. In particular, the properties of the SnO_2 surface itself have a strong influence on associative and dissociative water adsorption. Theoretical and experimental works on (101) and (110) surfaces describe the role of surface oxygen, oxygen vacancies and pre-existing hydroxyl groups [71]–[73]. Theoretical calculations for the (101) surface (see Figure 6 d and e) show, that on a fully reduced, i.e.

Sn-terminated, surface water is only adsorbed weakly as water molecules; while on the stoichiometric, i.e. Sn- and O-terminated, surface dissociative water adsorption is preferred [73]. Experimental investigations on H_2O adsorption on (101) surfaces, which utilize Ultraviolet Photoelectron Spectroscopy (UPS), reveal that water has a stronger influence on the stoichiometric surface and corroborates the differences between reduced and stoichiometric surfaces found by theoretical calculations [73]. A similar trend is found for the (110) surface; theoretical calculations for the stoichiometric, partially oxidized and partially reduced (110) surface show a dependency of associative or dissociative water adsorption on the surface oxygen coverage [71]. The comparison of the water adsorption on the stoichiometric surface and the partially oxidized surface – 50 % of a monolayer of atop oxygen species added – shows an increase of associative water adsorption due to an increased formation of H-bonds between water molecules and surface oxygen. Oppositely, for a partially reduced surface – removal of 50 % of the bridging oxygen species – an increase of dissociative water adsorption is observed [71]. The observed dependency of the surface oxygen coverage, is corroborated by experimental results, obtained by UPS and TPD studies, which show an increased associative adsorption of water on SnO_2 (110) surfaces with a low oxygen vacancy concentration [72]. However, in line with the observation for the reduced SnO_2 (101) surface, for high oxygen vacancy concentrations, a decrease of the dissociative adsorption is found for the SnO_2 (110) surface, too [72]. Regarding the effect of the pre-existing surface hydroxyl groups on the water adsorption on the SnO_2 surface, fewer results are reported in literature. According to theoretical calculations, pre-existing hydroxyl groups have a stabilizing effect on associatively adsorbed water, thus increasing associative water adsorption on SnO_2 [71]. The above described surface properties depend on temperature [52], e.g. as demonstrated by the evolution of the hydroxyl groups in dry air (see Figure 38) and on the basic material properties, which ultimately are determined by the material preparation process. In fact, the different effects of water vapour on two differently prepared SnO_2 materials, measured under the same conditions, are explained by the material/surface composition: Comparing the less oxygen deficient SnO_2 material studied in this work with a more defect rich SnO_2 [10], [34], [98], obtained by the same sol-gel route but calcined at 450 °C (8 h), the transition from dominant associative water adsorption, indicated in the DRIFT spectra by an attenuation of pre-existing hydroxyl groups, to dissociative water adsorption, indicated by an overall increase of the hydroxyl groups in the DRIFT spectra, occurs at different temperatures: For the material calcined at 1000 °C (8 h) the transition is found around 300 °C (Figure 39), while for the material calcined at 450 °C (8 h) the transition already occurs at 250 °C (Figure 40). Below the corresponding transition temperatures, water vapour causes a strong attenuation of the hydroxyl vibrations on both materials; while above the transition temperatures a clear increase of hydroxyl groups is observed. These results obtained from in-situ DRIFTS on SnO_2 powders not only highlight the role of the

material properties on the adsorption of water, but also demonstrate that same processes occur on both samples, although the temperature dependence of these processes is different.

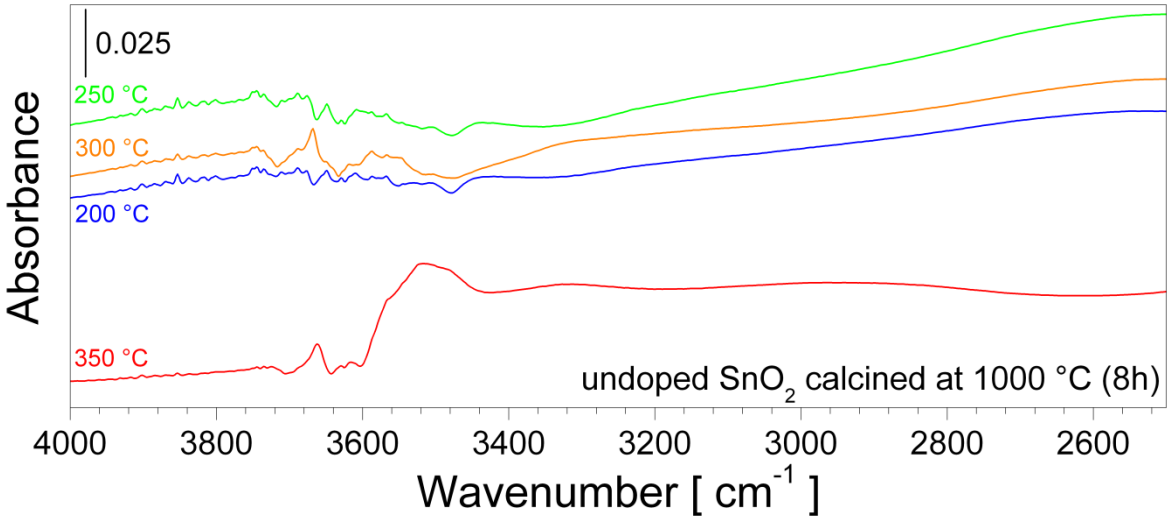

Figure 39. In-situ powder DRIFT spectra of SnO_2 calcined at 1000 °C (8 h) during the exposure to 10 % r.h. (25 °C) at different operation temperatures: 200 °C (blue), 250 °C (green), 300 °C (orange) and 350 °C (red). The spectra are referenced to spectra recorded in dry air at the corresponding operation temperature.

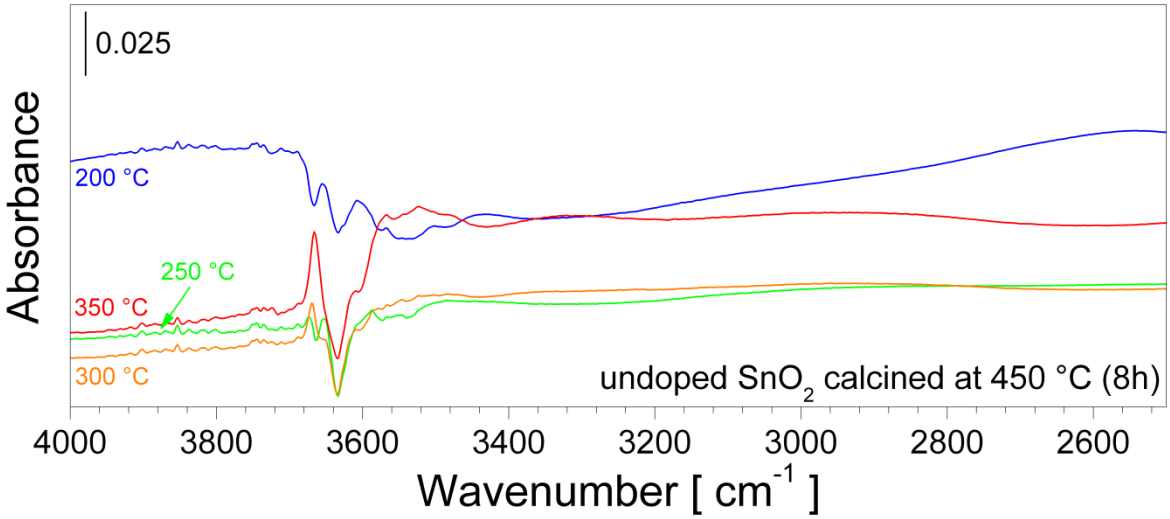

Figure 40. In-situ powder DRIFT spectra of SnO_2 calcined at 450 °C (8 h) during the exposure to 10 % r.h. (25 °C) at different operation temperatures: 200 °C (blue), 250 °C (green), 300 °C (orange) and 350 °C (red). The spectra are referenced to spectra recorded in dry air at the corresponding operation temperature.

The presented operando and in-situ DRIFT spectra of SnO_2 reveal that the interaction of water vapour with the SnO_2 surface changes significantly within the operation temperature range of SnO_2-based gas sensors (200 to 400 °C) and depends on the surface properties of the SnO_2 material.

5.3.3. Electrical impact of the different adsorbed water species

The effect of the differently adsorbed water species on the sensor resistance was investigated by a series of DCR measurements in addition to the one recorded during the operando DRIFTS measurements (Figure 41).

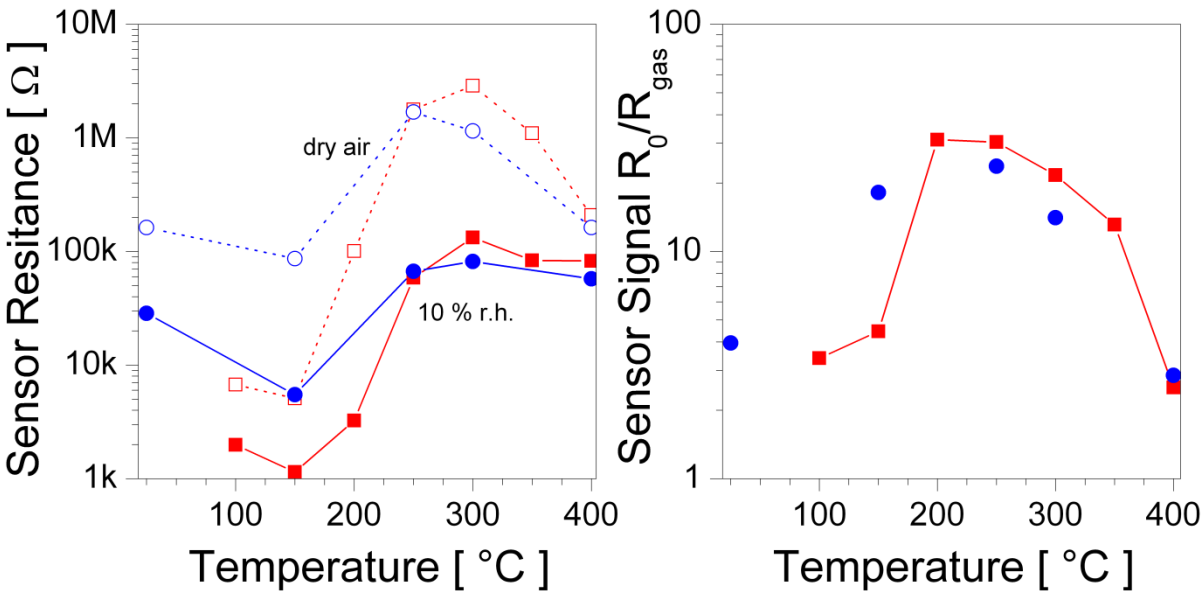

Figure 41. DC resistance measurement of undoped SnO_2 measured in dry and humid air (10 % r.h. at 25 °C) at different operation temperatures (left) and the correspondingly calculated sensor signal of water vapour (right). The DCR measured during operando DRIFTS (r.t., 150, 250, 300 and 400 °C) is shown in blue; the DCR recorded between 100 °C and 400 °C in 50 °C steps are shown in red. The resistance in dry air is represented by empty symbols/dotted lines and the one in 10 % r.h. by filled symbols/straight lines.

Above 200 °C, the measurements match quite well, however, at lower temperatures (150 °C) a strong difference in the measured resistances is found, which is not uncommon for low temperature measurements which tend to show a memory effect of high temperature treatments, namely the annealing during the sensor fabrication or previous measurements at higher temperatures. The latter can be excluded, since fresh samples were used. Both samples belong to the same batch, but were measured at different points in time, thus a decaying effect of the sensor annealing is a possible reason for the differences below 200 °C. However, regarding the temperature dependency of the sensor resistances in dry and humid air both measurements show the same qualitative trends. In both cases a distinct increase of the resistance is observed around 200 °C. Generally, the resistance of a semiconductor decreases with increasing temperature; in the case of SnO_2 the distinct resistance increase is assigned to the ionosorption of oxygen, which causes a depletion layer [19], [52]. The onset of the formation of active oxygen species at the SnO_2 surface is corroborated by CO sensing and CO oxidation measurements in the same temperature range (Supporting Figure 12), which show no CO conversion and only extreme weak sensor signal below 250 °C. Therefore, it can be assumed that the surface is not reactive below 250 °C. Regarding the effect of water vapour two general observations are made: in humid conditions the resistance is always lower than in dry air, i.e. the effect of water vapour is always a reducing one, and this reducing effect is observed for the whole temperature range measured - with a maximum around 250 °C. It is remarkable that the reducing effect occurs even in the absence of reactive oxygen species. According to the DRIFT spectra (Figure 34 and Figure 39) associative adsorption of water dominates at low temperatures. At room-

temperature, i.e. in the case of physisorption of water, ionic conduction, e.g. by protons, cannot be excluded. However, above 100 °C a contribution of ionic conduction is not likely, and due to the lack of experimental evidence for hydroxyl formation, it is also not likely that the reducing effect is causes by the formation of hydroxyl groups by a reaction with lattice oxygen creating hydroxyl groups (Reaction 10 and Reaction 11) [12]. The absence of reactive oxygen species also excludes a reducing effect due to the displacement of reactive oxygen by water vapour [52]. Thus, the resistance decrease observed below 200 °C only can explained by adsorbed water molecules acting as electron donors [69]. Between 200 and 300 °C the associative adsorption of water is still the dominant process (Figure 34 and Figure 39) and the donor effect of the water molecules still contributes to the resistance decrease caused by water vapour. Surprisingly, water vapour has the strongest impact in this temperature region, although the surface concentration of water molecules, i.e. the electron donor, is actually expected to decrease with increasing temperature. However, the displacement of ionosorbed oxygen due to water molecules, which block the surface and thus hinder the adsorption of oxygen, is in line with the observed surface reduction in DRIFTS (Figure 35 and Figure 36). Above 300 °C the dissociative adsorption of water dominates, resulting in a restoration of desorbed hydroxyl groups. The rise in dissociative adsorption correlates with a distinct decrease of the reducing effect (Figure 41); since the hydroxylation caused by water vapour exposure increases with temperature, while the reducing effect decreases, the reaction of water vapour with the surface is charge neutral (Reaction 12) [68] instead of reducing (Reaction 10 and Reaction 11) [12]. The progressive decrease of the reducing effect with increasing temperature is attributed to a decrease of associatively adsorbed water species, due to the reaction, i.e. dissociative adsorption, and desorption. Based on the experiments presented in this work three different (temperature) regions are found for the interaction of water vapour with the surface and the resulting resistance changes:

- At low temperatures, i.e. below the onset of the oxygen ionosorption, associative adsorbed water acts as an electron donor and causes a resistance decrease
- At temperature above the onset temperature of oxygen ionosorption at which associative water adsorption is still the dominant process, the adsorbed water molecules still act as a donor, but additionally displace some of the ionosorbed oxygen, causing a strong change of the sensor resistance
- At high temperatures, more precisely after the partial desorption of hydroxyl groups, dissociative water adsorption dominates and water vapour restores some of the desorbed hydroxyl groups. Overall, the dissociative adsorption of water is found to have low impact on the resistance and is related to the charge neutral reaction

5.3.4. Conclusions on the interaction of water vapour with the SnO_2 surface

In conclusion, the results of the in-situ/operando DRIFTS and DCR investigations on the interaction of water vapour with the SnO_2 surface revealed that the nature of the dominant interaction – physisorption, associative or dissociative adsorption – depends on the operation temperature as well as the properties of the SnO_2. The electronic effect of water strongly depends on the nature of the interaction. Associatively adsorbed water acts as an electron donor and displaces surface oxygen, i.e. indirectly reduces the surface. The dissociative adsorption of water has a low impact on the resistance. In the above discussed results, no correlation is found between hydroxyl formation and a strong reducing effect, thus it is deduced that dissociative water adsorption proceeds preferentially by a charge neutral reaction. However, associative and dissociative adsorption of water affect the reactive oxygen species, i.e. lower the reactivity of the surface and interfere with the gas reception.

6. The Impact of Platinum on the Gas Sensing Mechanism

The enhanced gas sensing properties of noble metal loaded SMOX are well reported in literature [84], [86], but the role of noble metal dopants in the reception and transduction is still matter of debate. Especially in the case of Pt, which is found in a large number of possible structures, the identification of structure-function-relationships is rather challenging and current experimental evidence linking the structure of the Pt loading and gas sensing is fragmentary. One exception are the investigations on atomic Pt sites in SnO_2, which combine the determination of the Pt structure – including the one in operation conditions, operando spectroscopic studies of Pt-related changes in the surface chemistry and the evaluation of the impact on the electronic properties of SnO_2 [20], [22], [23]. If Pt is homogenously distributed in the SnO_2 lattice, the surface chemistry is changed due to an additional activation of lattice oxygen bound to Pt [20], [145]. In case of CO sensing, Pt offers specific adsorption sites for CO improving the CO sensing performance in humid conditions by separating the interaction of CO with the surface from the interaction of water vapour with SnO_2 [20]. Furthermore, Pt acts as an electron acceptor, shifting the Fermi level to lower energies and creating an additional surface band bending; the determined initial band bending by Pt is much smaller than the one of Al or Pd incorporated in the SnO_2 lattice [23]. These studies demonstrate the complex role of noble metal dopants. In the case of inhomogeneously dispersed Pt, i.e. if Pt forms a separate phase, comparable systematic studies are missing even if this is mostly the case for commercial sensors. Already the determination of the Pt structure is controversial. In case of high Pt loadings, TEM pictures show the presence of metallic Pt [146], [147], while X-ray photon electron spectroscopy indicates oxidized Pt for low loadings [11], [148]. The results presented in the following chapter systematically describe the structure of different Pt-loadings on SnO_2 introduced by the powder impregnation method, the resulting chemical and electronic changes of the material and their impact on the gas sensing process.

6.1. Structure of the Platinum Loading

The samples were prepared by the powder impregnations process described above (see 4.1.1. Powder Preparation). The Pt content of the prepared materials was analysed by ICP-OES. For the samples with the nominal loadings of 0.2 wt% and 2.0 wt%, Pt contents of 0.0568±0.0008 wt% and 0.2030±0.0010 wt% were found, respectively. Assuming that all Pt is located on the surface of SnO_2 grains with a diameter of 100 nm (Figure 24), the approximated surface concentrations of Pt are 1.4 wt% and 5.1 wt%, respectively. For the sake of simplicity, the nominal loadings will be used to identify the samples in the following discussion.

Knowing the exact structure of the Pt loading is fundamental in order to understand and describe its role in the gas sensing process, i.e. its impact on the gas reception and transduction. Determining the structure of noble metals dopants is rather challenging, since common techniques like XRD are not suitable due to the lack of large and well-ordered noble metal structures [90]. Electron microscopic techniques can provide essential information on size and dispersion of noble metals [25]; however, the information is gathered under conditions far from realistic application conditions. A suitable method to study the structure and oxidation state, even of small and amorphous, noble metal loadings in gas sensing materials is XAS [116]. The ex-situ XANES of 0.2 wt% and 2.0 wt% Pt-doped SnO_2 are shown in Figure 42 (left). For comparison, additional XANES spectra of reference substances (Pt foil and PtO_2) are shown. The position of the whiteline (first absorption maximum after the edge step) depends on the oxidation state of the absorbing element and is shifted to higher energies with increasing oxidation state [118]. The XANES spectra of the two Pt-doped SnO_2 materials match with the PtO_2 reference, i.e. Pt is present in +4 oxidation state. The visual inspection of the Fourier-transformed EXAFS (Figure 42, right) shows similar features for the Pt-doped SnO_2 materials and the PtO_2 reference. The first coordination shell of the Pt-doped SnO_2 samples and PtO_2 is found to be the same. However, especially the contributions corresponding to the 2nd and 3rd coordination shells (R > 2 Å) show differences. In case of other Pt-doped SnO_2 materials these differences are attributed to a contribution of Sn backscatters [22], [92]. The quantitative analysis of the EXAFS reveals a contribution of Pt and Sn backscatters in the 2nd and 3rd coordination shell of Pt-doped SnO_2 [149], [150]. Thus, the structure of the Pt loading is similar to the one of PtO_2 and the formed PtO_2-like oxide phase in close contact to SnO_2. The proposed structural model for the Pt loading on SnO_2 is the formation of small Pt oxide clusters on the SnO_2 surface, as shown in Figure 43. Due to the strong contribution of Sn backscatters in the outer coordination shells, it is concluded that the Pt oxide clusters are rather flat.

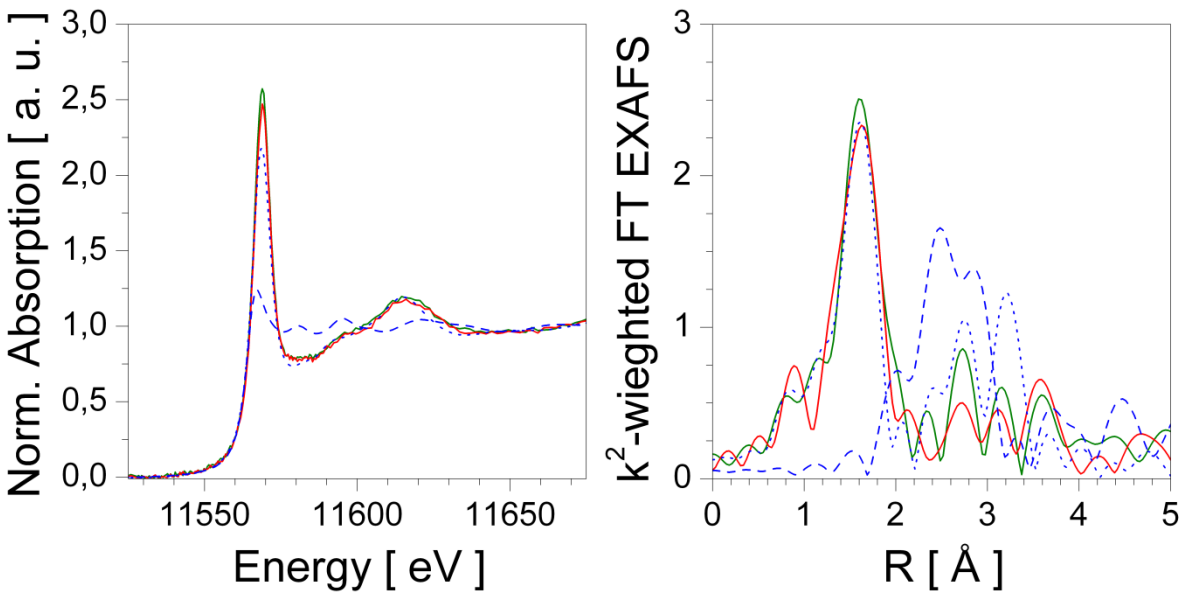

Figure 42. Normalized XANES spectra (left) and the baseline subtracted and Fourier-transformed EXAFS (right) of ex-situ X-ray absorption spectra recorded from 0.2 wt% (green) and 2.0 wt% (red) Pt-doped SnO_2. The corresponding reference substances are shown in blue, Pt foil as a dashed line and PtO_2 as a dotted line.

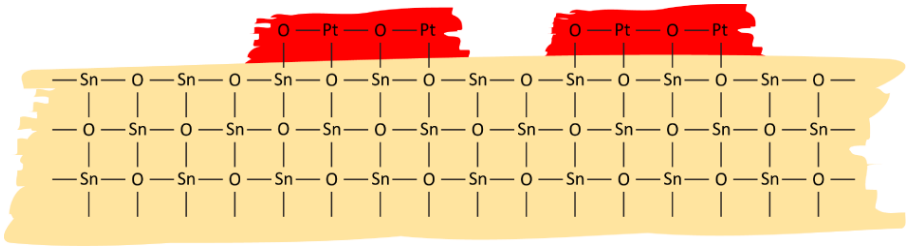

Figure 43. Proposed structure of the Pt oxide clusters formed on SnO_2. In order to avoid the impression of a refined structural model obtained by theoretical calculations, the structure is shown in a simplified two-dimensional cross-section instead of a ball-stick model of a single crystal surface.

To study the size and dispersion of the Pt dopant the samples were studied by TEM. The HAADF-STEM image of 2.0 wt% Pt-doped SnO_2 (Figure 44, left) shows only a few metallic clusters (3-5 nm) on the SnO_2 grains. A detailed analysis of the surface by HR-TEM (Figure 44, right) shows in addition to the metallic clusters the presence of very small (< 1 nm) amorphous oxide clusters on the surface of the SnO_2 grains. Regarding the results from the ex-situ XAS, the amorphous clusters are identified as very small Pt oxide clusters in close contact with the SnO_2 surface. The presence of metallic Pt is in contradiction with the results from XAS, but if the same image section is observed for a longer period of time (Figure 45), the amount of metallic Pt clusters increases, i.e. metallic Pt is formed due to the exposure to the electron beam, which reduces the Pt oxide clusters. Thus, the presence of metallic Pt is attributed to the measurement conditions so Pt actually is present as Pt oxide clusters. The formed metallic clusters (Figure 44, right) demonstrate the high and even dispersion of the Pt on SnO_2, i.e. the Pt doping homogeneously affects the SnO_2 surface and thus the whole sensing layer.

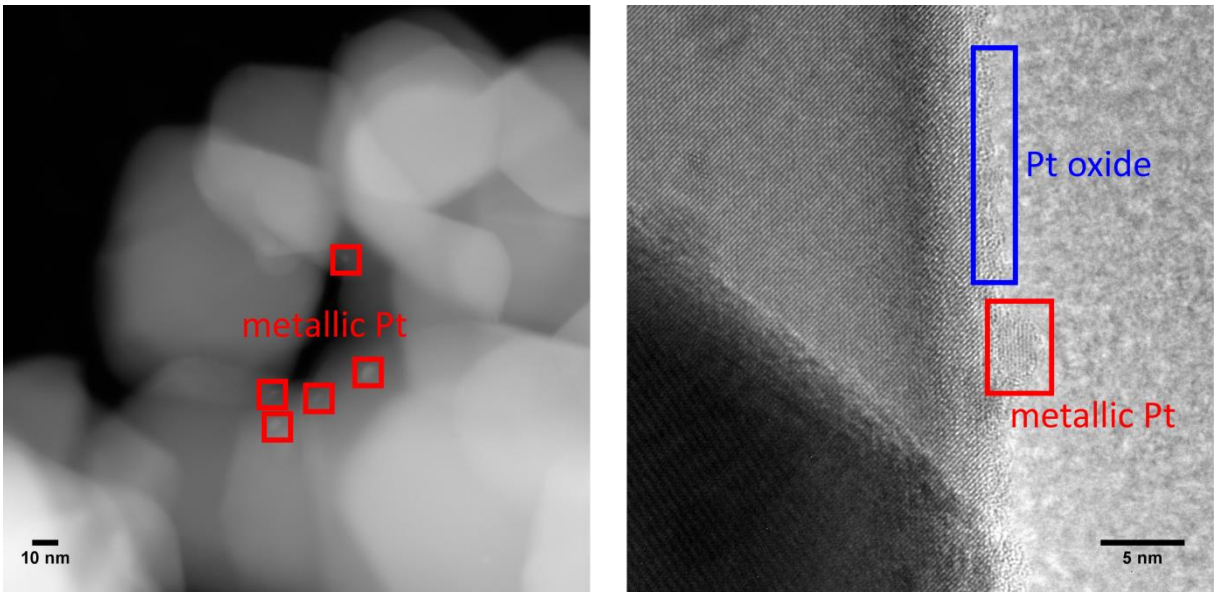

Figure 44. HAADF-STEM (left) and HR-TEM (right) imanges of 2.0 wt% Pt-doped SnO_2. The identified Pt oxide or metallic clusters are highlighted in blue or red, respectively.

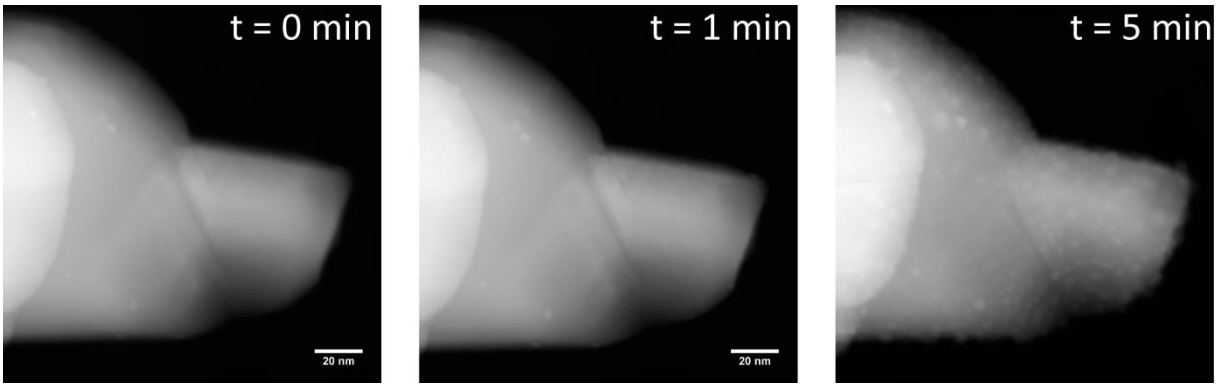

Figure 45. HAADF-STEM images of 2.0 wt% Pt-doped SnO_2 after 0, 1 and 5 min exposure to the electron beam (see annotations in the top right corner).

The reducibility of the Pt oxide clusters is also observed during temperature programmed reduction (TPR) in 0.5 %vol H_2/He. As shown in Figure 46, a shift of the whiteline towards lower energies, i.e. the reduction of oxidized Pt, is already observed at room temperature when changing from inert gas (He) to reducing conditions (0.5 %vol H_2/He) and rapidly proceeds with increasing temperature. A reduction of Pt by the high brilliance X-ray beam is unlikely since no reduction is observed in pure He. This experiment corroborates the trend observed by TEM (Figure 45). Based on this experiment one can state, that Pt is not strongly incorporated in the SnO_2 lattice itself, as Pt strongly incorporated in SnO_2 is not reduced, even in much harsher conditions (2 vol% H_2/He at 600 °C) [22]. Furthermore, the facile reduction of Pt proves that Pt easily interacts with gases, i.e. is solely present at the surface of SnO_2. The reduced Pt is easily re-oxidized when switching gas flow from the H_2/He mixture to air as (see Figure 46). Thus, it can be assumed that the oxidation state of Pt is dynamic and depends on the atmospheric composition. The facile reduction and re-oxidation of the Pt oxide clusters brings forth the question whether metallic or oxide clusters are found in typical gas sensing conditions, i.e. at 300

°C in air, in the absence and in the presence of small amounts of reducing gases. Normalized XANES spectra recorded during a H_2 sensing experiment in dry air are shown in Figure 47. The exposure of the reducing gas does not cause a shift of the whiteline, i.e. Pt remains oxidized, but the decreased intensity of the whiteline indicates a decreased density of empty d-states due to H_2 exposure [151].

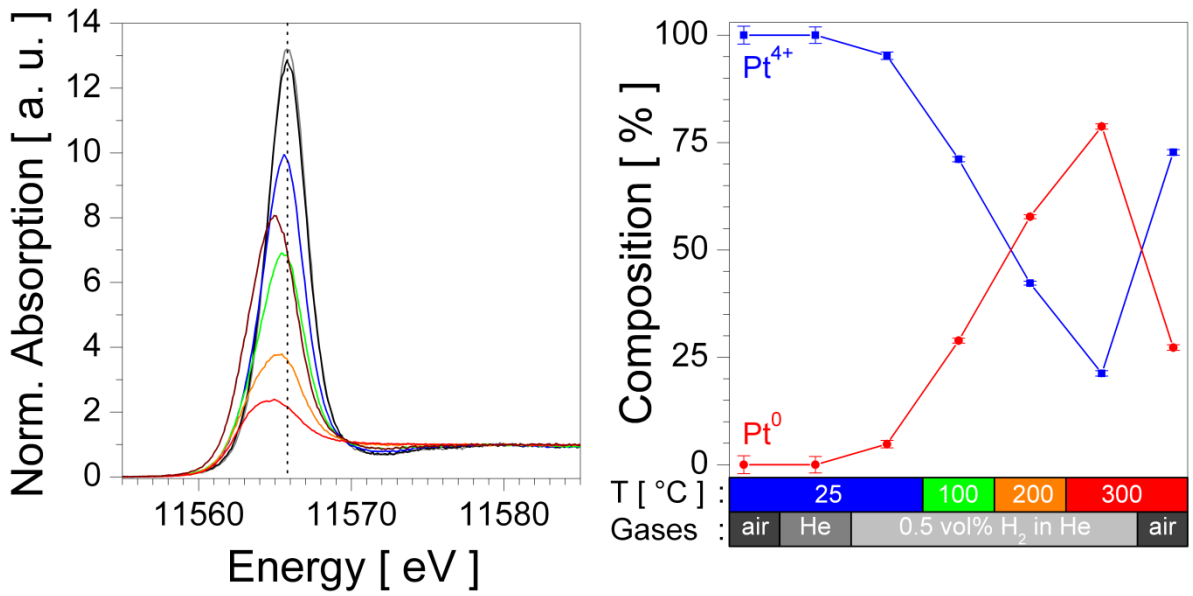

Figure 46. Normalized HERFD-XANES spectra recorded during TPR experiment of a 0.2 wt% Pt-doped SnO_2 gas sensor (left): 25 °C in air (gray), 25 °C in He (black), 25 °C in 0.5 %vol H_2/He (blue),100 °C in 0.5 %vol H_2/He (green), 200 °C in 0.5 %vol H_2/He (orange), 300 °C in 0.5 %vol H_2/He (red) and 300 °C in 0.5 %vol H_2/He (dark red). The corresponding composition of Pt^0 and Pt^{4+} derived by linear combination fitting of the XANES in shown in the graph on the right.

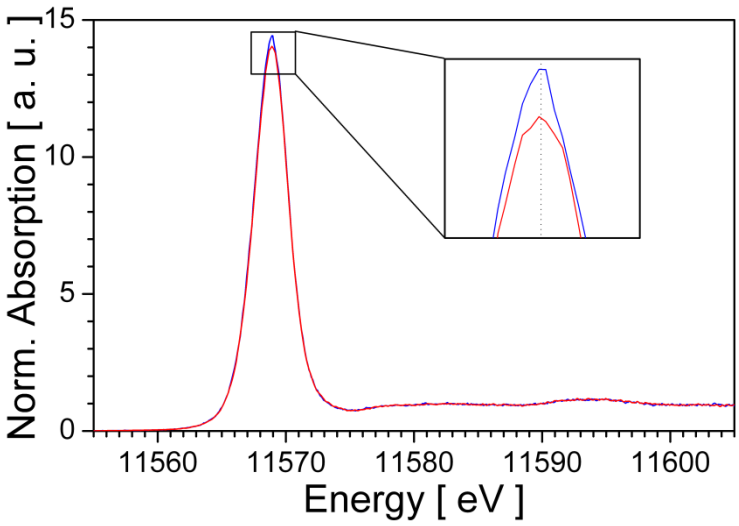

Figure 47. Normalized HERFD-XANES spectra of a 0.2 wt% Pt-doped SnO_2 gas sensor recorded at 300 °C in dry air (blue) and during the exposure of 50 ppm H_2 in dry air (red). The inlay shows the magnified maximum of the whiteline.

The XAS and TEM measurements carried out to investigate the structure of the Pt loadings provide a conclusive picture. Pt is present as very small oxide clusters on the surface of the SnO_2 grains and in close contact with SnO_2. The facile interaction of the clusters with the atmosphere causes a dynamic dependency of the oxidation state on the atmospheric composition: In the absence of oxygen Pt is

easily reduced to metallic Pt, either by a reducing gas or an electron beam. In excess of oxygen, i.e. in air, Pt is oxidized and not reduced by the exposure to reducing gases, although the decreased intensity of the whiteline indicates changes in the unoccupied d-states of Pt.

6.2. Gas Sensing Performance and Catalytic Activity of Pt-doped SnO_2

Introducing noble metals like Pt onto the SnO_2 surface is generally found to enhance the reactivity of the material, especially when compared to a corresponding undoped SnO_2 [152]–[154]. Thus, the relationship between the sensor signals and the catalytic activity and the effect of interfering gases, like water vapour, are studied by comparing CO sensor signals and CO conversion in different humidity backgrounds (Figure 48). In case of CO sensing the Pt-doped materials show decreased sensor signals in dry air while the sensor signals in humid air increase. For undoped SnO_2 the opposite trend is observed. Regarding the role of the Pt concentration, it is found that the higher Pt loading shows lower sensor signals in dry and humid air. These trends are confirmed by CO and H_2 sensing measurements of all three materials in dry air and 50 % r.h., which were performed over a larger concentration range (see Supporting Figure 13), one should note that in the case of H_2 the effect of humidity on the sensor signals of the doped materials is depending on the H_2 concentration.

The CO oxidation measurements show significant differences between the undoped and the two Pt-doped samples. Generally, the Pt-doped SnO_2 materials show increased CO conversion, which reaches almost 100 %. The increased reactivity of the Pt-doped SnO_2 is in agreement with CO oxidation studies on Pt-loaded SnO_2 [152], [154]. In the case of undoped SnO_2, a strong decrease of the CO conversion is observed when comparing dry and humid conditions (10 %r.h. at 25 °C); with further increasing humidity (above 10 % r.h. at 25 °C) a lower influence and a gradual decrease of the CO conversion are observed. This decrease correlates with the decreasing sensors signals and is caused by the interference of water vapour with the reactive oxygen species reported in the previous chapters. In the case of the Pt-doped SnO_2 materials, no abrupt decrease of the CO conversion is observed when changing from dry to humid conditions; the CO conversion of the Pt-doped SnO_2 materials shows only a minor and gradual decrease with increasing humidity, which is more pronounced for the lower Pt-loading. The differences in the decrease of the CO conversion in humid conditions suggest that the higher Pt-loaded material is generally more reactive than the one with the lower loading. By comparing the CO sensor signals and the CO conversion it is observed that in dry air the sensor signals decrease with an increasing reactivity of the materials while in humid air the situation changes: The undoped SnO_2 shows the lowest sensor signals and the lowest CO conversions. In case of the Pt-doped samples, the less reactive material still shows higher sensor signals than the more reactive one. In dry air, the correlation of the sensor signals and CO conversion of the Pt-loaded SnO_2 materials suggests that, on the one hand, the oxidation of CO proves a strong and efficient oxidation of CO on the Pt-doped SnO_2 surface but, on the other hand, this interaction is not transformed into changes of the electronic properties of SnO_2, i.e. a sensor signal. In humid conditions, there is still a considerable interaction of CO with the surface, which now is transformed

into a sensor signal. Therefore, it is likely that the observed effects are related to changes in the surface chemistry of SnO_2.

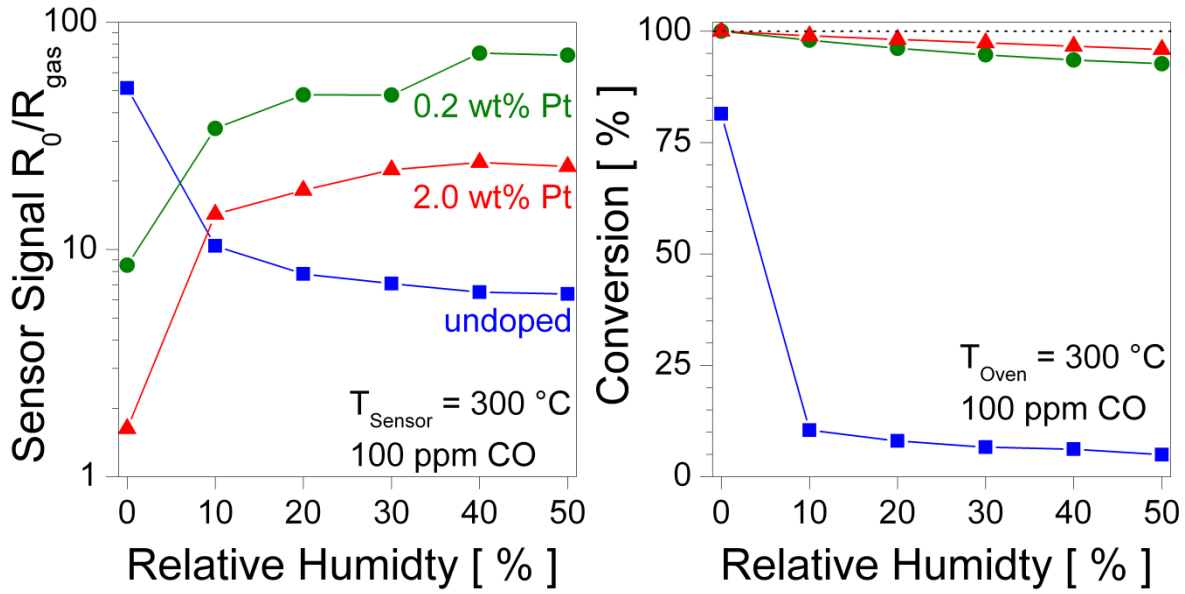

Figure 48. CO sensing (left) and catalytic conversion of CO (right) of undoped SnO_2 (blue squares), 0.2 wt% (green circles) and 2.0 wt% (red triangles) Pt-loaded SnO_2 measured at 300 °C in different humidity backgrounds.

6.3. Impact on gas reception

In order to study the surface chemistry of the Pt-doped SnO_2 materials, operando DRIFT spectra were recorded during CO exposure in dry and humid air. The spectra for 0.2 wt% and 2.0 wt% Pt-doped SnO_2 are shown in Figure 49 and Figure 50, respectively. Comparing the DRIFT spectra of the Pt-doped materials with undoped SnO_2 (Figure 27) several differences are found. The spectra of the Pt-doped samples show the formation of carbonyl species at 2148 and 2125 cm^{-1}, which are assigned to CO bound to oxidized Pt [132], [155]. Both carbonyl species differ from that reported for Pt incorporated in the SnO_2 lattice, which is found at 2124 cm^{-1} [20]. The different carbonyl species corroborate the structural differences between the homogeneously dispersed Pt (gel impregnation) and the inhomogeneous Pt dispersion (powder impregnation). The two carbonyl species found on powder impregnated Pt-doped SnO_2 indicate an involvement of Pt-related reaction sites in the CO oxidation and/or gas reception. However, the two carbonyls show different stabilities; the band at 2135 cm^{-1} quickly decreases after stopping the CO exposure, while the band 2148 cm^{-1} is still well observed in the DRIFT spectra (see Supporting Figure 14). Therefore, the latter band is considered to be a spectator species, since the carbonyl is not oxidized to CO_2 at 300 °C in air and still present after the recovery of the sensor resistance; i.e. this carbonyl is assumed not to be involved in the CO oxidation or the gas sensing process. Another striking difference between undoped and Pt-doped SnO_2 is found in the fingerprint region. On undoped SnO_2 the two Sn-O bands at the highest wavenumber are found at 1361 and 1334 cm^{-1}, while on the 0.2 wt% and 2.0 wt% Pt-doped the two bands in this region are found at 1380 and 1349 cm^{-1} or 1389 and 1349 cm^{-1}, respectively. Isotopic labelling experiments with $^{12}CO/^{13}CO$ (Supporting Figure 15 and Supporting Figure 16) exclude the superposition of a formed carbon containing species with the decreasing Sn-O bands as the reason for the observed changes, and H_2O/D_2O exchanges (Supporting Figure 17 and Supporting Figure 18) exclude the assignment of these bands to Sn-OH deformation vibrations. Thus, the observed changes in the fingerprint region are attributed to the presence of additional metal oxygen bond, which are related to the presence of Pt oxide clusters at the SnO_2 surface. The existence of Pt-O-Sn as well as Pt-O-Pt bonds is shown by the quantitative analysis of the EXAFS of powder impregnated Pt-doped SnO_2 materials [149], [150]. Comparing the impact of CO exposure in dry and humid conditions on the metal oxygen bonds, or on the spectra, in general, a stronger decrease of the metal oxygen bonds, i.e. reduction of the material, is observed in humid air. Furthermore, it is observed, that relative to the Sn-O bands (1271, 1205 and 1059 cm^{-1}) the decrease of the bands at 1380 or 1389 cm^{-1}, respectively, is stronger in dry air than in humid air. Since these bands are assigned to the Pt oxides phase, it is concluded that in dry air the reaction dominantly takes place at sites related to the Pt oxide clusters and not on the undoped SnO_2 surface, i.e. at sites that are not related to the reception and transduction on the pristine SnO_2 surface. Indeed, in case of 2.0 wt% Pt-doped SnO_2,

CO exposure in dry air causes only a low sensor signal (Figure 48, left) and almost no reduction of the surface, only a weak decrease of the metal oxygen bond assigned to the Pt oxide clusters (1389 cm^{-1}) is observed. In the case of 0.2 wt% Pt-doped SnO_2, a higher sensor signal and a clear reduction of the whole surface is observed during CO exposure in dry air.

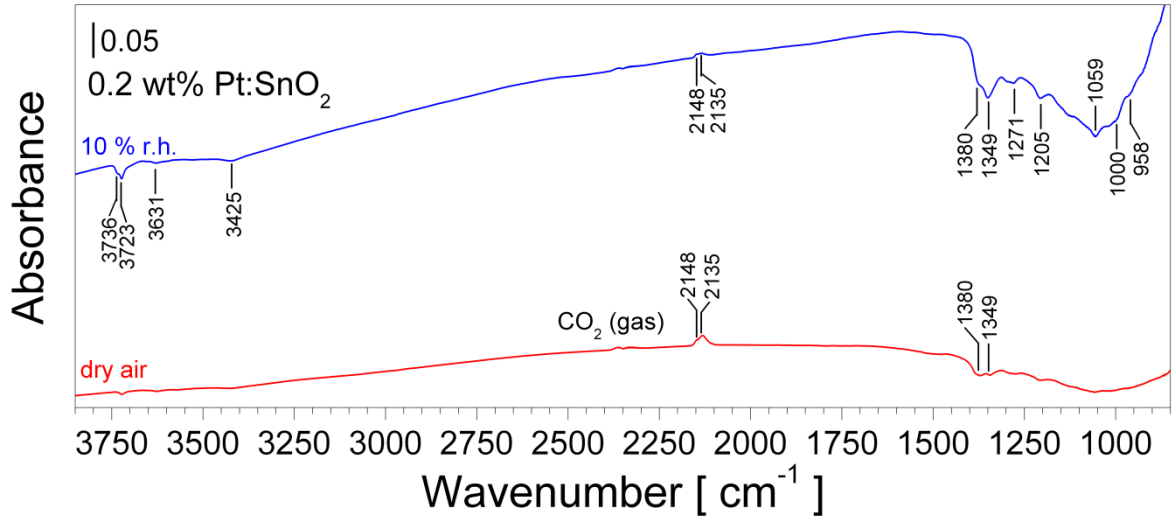

Figure 49. DRIFT spectra of 0.2 wt% Pt-doped SnO_2 exposed to 300 ppm of CO in dry (red) and humid conditions, 10 % r.h. at 25 °C, (blue). The sensor temperature was 300 °C. The spectra were referenced to spectra recorded in dry or humid conditions, respectively.

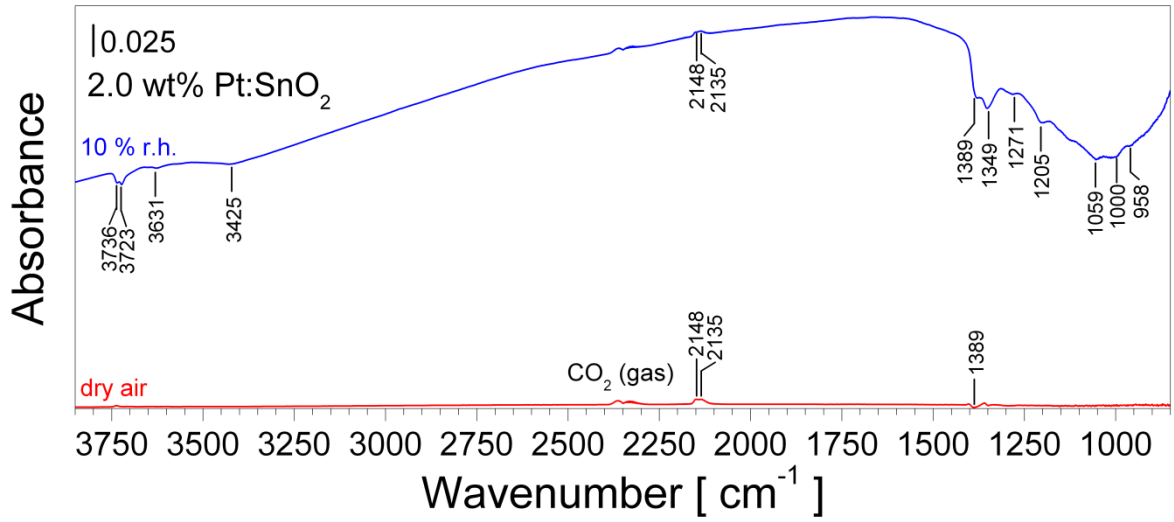

Figure 50. DRIFT spectra of 2.0 wt% Pt-doped SnO_2 exposed to 300 ppm of CO in dry (red) and humid conditions, 10 % r.h. at 25 °C, (blue). The sensor temperature was 300 °C. The spectra were referenced to spectra recorded in dry or humid conditions, respectively.

A high CO oxidation activity of platinum oxides is reported in literature and it is generally expected that this reaction takes place by a Mars-van-Krevelen mechanism [156]–[160]. Thus, the oxidation of CO on the Pt oxide clusters involves two major steps: The oxidation of CO by oxygen from the Pt oxide, i.e. the reduction of Pt oxide, and the re-oxidation of the Pt oxide. If the re-oxidation is facile, there will be no or only small changes of the Pt oxide cluster stoichiometry. However, if the re-

oxidation is hindered, e.g. by the presence of an interfering gas like water vapour or the lack of atmospheric oxygen, the stoichiometry of the Pt oxide clusters will be changed. In order to verify a Mars-van-Krevelen mechanism for the CO oxidation on the Pt oxide clusters, the undoped and Pt-doped SnO_2 materials were exposed to different CO concentration in a low oxygen background of about 64 ppm. Referring the CO concentrations to the ideal stoichiometry of the CO oxidation by atmospheric oxygen ($CO:O_2$ ratio of 2:1), three different regions are distinguished: Oxygen rich mixtures for low CO concentrations (20 and 50 ppm), a gas mixture close to the stoichiometric value (100 ppm CO) and oxygen lean conditions for high CO concentrations (200 and 500 ppm CO). In the case of undoped SnO_2 a steady increase of the surface reduction is observed in all three regions (see Supporting Figure 19). In the case of Pt-doped SnO_2 the spectra reveal strong differences between oxygen rich and oxygen lean conditions: In oxygen rich conditions Pt is oxidized, while the formation of carbonyls bound to metallic Pt and the disappearance of carbonyls bound to oxidized Pt are observed in oxygen lean conditions (Figure 51). The presence of solely oxidized Pt in oxygen rich conditions as well as the reduction of the Pt oxides clusters in oxygen lean conditions is in agreement with the operando and TPR-XANES (Figure 46 and Figure 47). Furthermore, close to or above the stoichiometric mixture a strong increase of the surface reduction of the materials is observed for 0.2 wt% ors 2.0 wt% Pt-doped SnO_2, respectively (see Supporting Figure 20 and Supporting Figure 21). The experiment demonstrates a preferential reaction of CO with the Pt oxide clusters. However, if a re-oxidation of the clusters by atmospheric oxygen is no longer possible oxygen from SnO_2 is involved in the reaction; the consumption of oxygen from oxides supporting noble metals was recently demonstrated for $Pt:CeO_2$ [161]. The involvement of oxygen from the supporting SnO_2 oxide is observed in oxygen lean atmospheres as well as in the presence of water vapour. It is, thus, concluded that water vapour hinders the re-oxidation of the Pt oxide clusters. Since the re-oxidation of the Pt oxide clusters as well as the SnO_2 surface is hindered in humid air, the oxidation of CO on Pt-doped SnO_2 causes a strong overall reduction of the surface.

The changes in the gas reception of Pt-doped SnO_2 are summarized as follows: In dry air, and with increasing Pt loading, Pt-doped SnO_2 is found to be rather a catalyst than a sensing material, i.e. the oxidation of CO proceeds more facile (Figure 48, right) but the surface is not changed by the reaction (Figure 49 and Figure 50). The lack of a reduction of the surface during CO exposure implies that there is no effective gas reception resulting in no or a strongly decreased sensor signal in dry air (Figure 48, left). The catalytic enhanced CO oxidation on Pt-doped SnO_2 is less affected by water vapour than the CO oxidation on undoped SnO_2. This is the essential difference between the materials; on undoped SnO_2 the interaction of CO with the surface is inhibited by water vapour, while CO still reacts with the Pt-doped SnO_2 surface in the presence of water vapour. In humid air the DRIFT spectra of the Pt-doped SnO_2 materials reveal a stronger overall reduction of the surface,

which involves metal oxygen species assigned to SnO_2 and to the Pt oxide clusters (Figure 49 and Figure 50). This increased reduction of the surface during CO exposure implies an effective gas reception and therefore leads to considerable sensor signals (Figure 48, left).

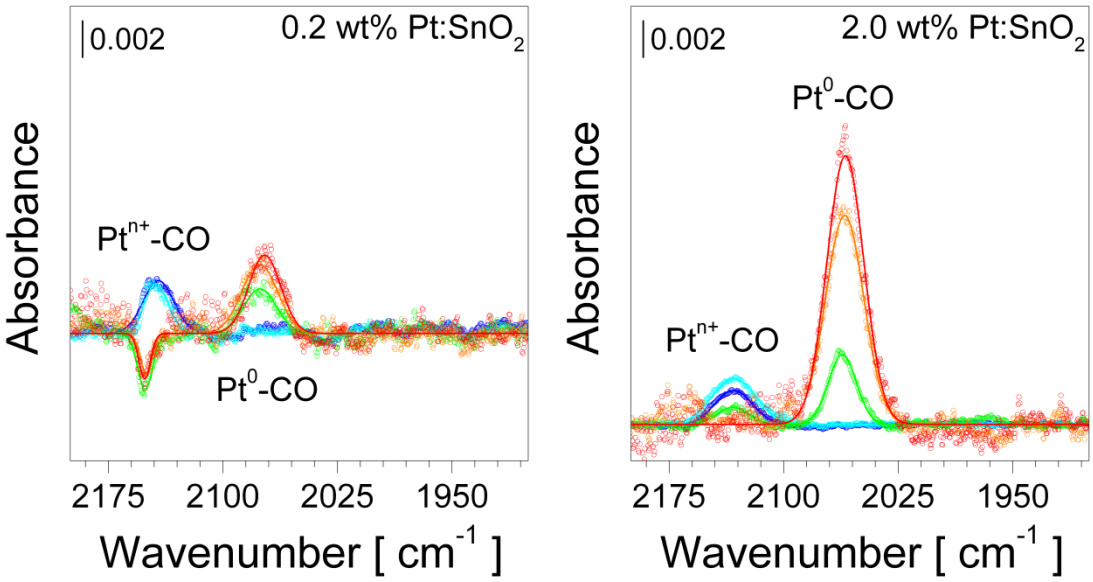

Figure 51. Baseline corrected carbonyl region of the DRIFT spectra recorded from 0.2 wt% (left) and 2.0 wt% (right) Pt-doped SnO2 during CO exposure in a O_2/N_2 mixture: 20 ppm CO (blue), 50 ppm CO (cyan), 100 ppm CO (green), 200 ppm CO (orange) and 500 ppm CO (red). The sensor temperature was 300 °C. The spectra were referenced to a spectrum recorded in in the pure O_2/N_2 mixture. The negative Pt^{n+}-CO band in case of 0.2 wt% Pt:SnO_2 is caused by the stable carbonyl species (2148 cm^{-1}), which desorbs extremely slow and is still present due to previous experiments.

6.4. Impact on transduction

A possible impact of the Pt oxide clusters on the transduction requires an electronic interaction of the clusters with SnO_2 [84]. The structural investigations suggest a strong interaction of the Pt oxide clusters and SnO_2 (see 6.1. Structure of the Platinum Loading). Such an electronic interaction, e.g. due to the presence of electronic surface states related to surface structures or the alignment of the Fermi level of two solids with different work functions, generates space charge layers independent of the ionosorption of gases, i.e. an initial band bending [50], [89]. In the absence of any reactive gases, e.g. in pure N_2, undoped SnO_2 does not show an initial band bending [53]; an upwards band bending induced by the Pt oxide clusters would lead to an increased resistance of the sensor in N_2. In order to evaluate the existence of an electronic interaction of the Pt oxide clusters with SnO_2, the resistances undoped and Pt-doped SnO_2 sensors were measured in pure N_2 (see Table 4).

Table 4 - Sensor resistances in N_2, and the corresponding residual oxygen concentration during the measurement. The approximated band bending caused by the Pt doping (Equation 19) is shown in the right column.

sample	sensor resistance [Ω]	oxygen background [ppm]	initial band bending [meV]
undoped SnO_2	468	2.8	--
0.2 wt% Pt-doped SnO_2	19047	2.9	183
2.0 wt% Pt-doped SnO_2	129960	2.7	278

By taking the resistance of undoped SnO_2 in N_2 as reference (R_0), one can approximated the initial upwards band bending using the resistances of the Pt-doped materials in N_2 (R) by the following equation [53]:

$$eV_S = k_B T \cdot ln\left(\frac{R}{R_0}\right) \qquad \textbf{Equation 19}$$

The estimated initial band bending is found to be 183 meV and 278 meV for 0.2 wt% and 2.0 wt% Pt-doped SnO_2, respectively. The treatments during the doping procedure as such should have no impact on the bulk properties, layer morphology and grain size of SnO_2 [90]. Thus, the band bending should solely be caused by the electronic interaction of the Pt oxide clusters and SnO_2. The Pt oxide clusters most likely cannot be described as a bulk phase with a Fermi level, thus the electronic interaction is described as the formation of an electronic acceptor state at the surface. Nonetheless, the formation of a surface acceptor state and the alignment of the Fermi levels have the same consequence, namely a pinning of the electronic properties of the SnO_2 surface in the vicinity of the Pt oxide clusters. In case of a sufficient and well-dispersed loading, as it is found for the studied Pt-doped SnO_2 (Figure 45), the space charge layer and thus the resistance of the sensor are controlled

by the electronic interaction of the Pt oxide clusters and SnO_2 [52], [84], [89]. Consequently, the resistance depends on the composition of the Pt oxide clusters, which are responsible for the electron acceptor state. Indeed, large resistance changes are observed during the reduction of the Pt oxide clusters in oxygen lean conditions (see Figure 51), as shown in Figure 52. Undoped SnO_2 shows a uniform increase of the sensor signal in oxygen rich and oxygen lean conditions, which is in line with the steadily increasing reduction of the surface observed in DRIFTS (Supporting Figure 19). On the opposite, both Pt-doped SnO_2 materials show a sudden increase of the sensor signal close to stoichiometric reaction conditions. In both cases this effect correlates with the transition of oxidized to metallic Pt, i.e. the ultimate change of the Pt oxide cluster composition.

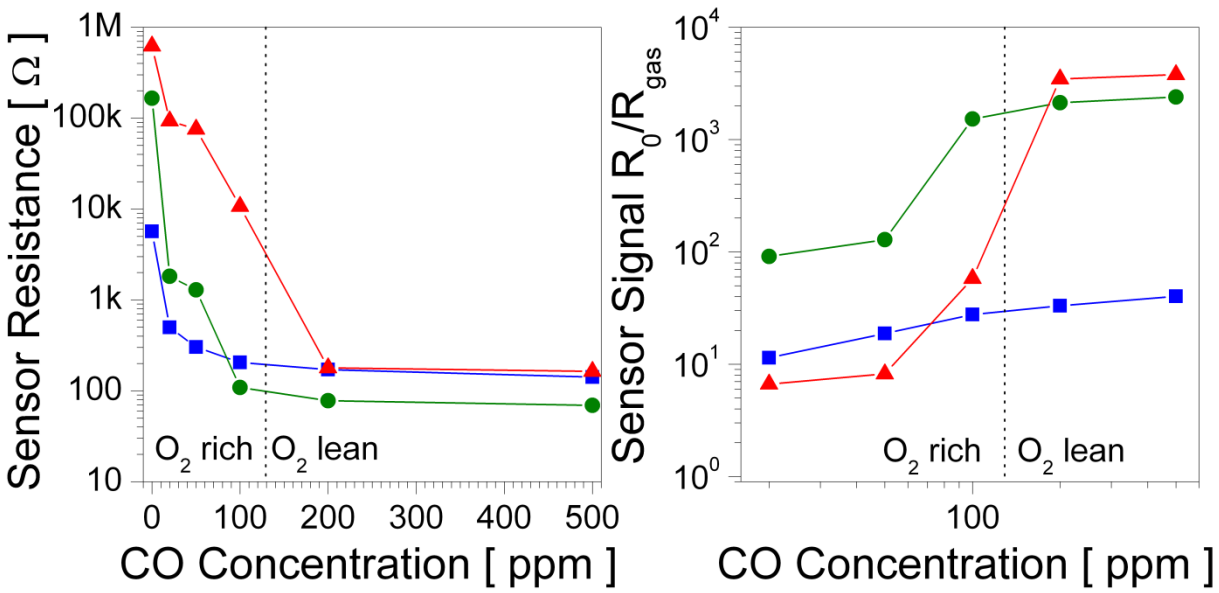

Figure 52. Sensor resistance (left) and calculated sensor signals (right) of undoped SnO_2 (blue squares), 0.2 wt% (green circles) and 2.0 wt% (red triangles) Pt-doped SnO_2 during the exposure to CO in the O2/N2 mixture. The corresponding carbonyl regions of the simultaneously recoreded DRIFT spectra are shown in Figure 51.

The electronic interaction of the Pt oxide clusters and SnO_2 as well as the dependence of the sensors signals on the composition of the Pt oxide clusters imply that the gas sensing effect of the Pt-doped SnO_2 materials is governed by the chemistry which takes place on the Pt oxide clusters and the resulting compositional changes of the Pt oxide clusters. Accordingly, the transduction takes place by a Fermi-level control mechanisms and is no longer linked to the reduction and re-oxidation of the pristine SnO_2 surface.

6.5. Summary of the changes in gas reception and transduction

The presence of Pt oxide clusters has a strong impact on the gas reception and on the transduction. The reactivity of the Pt-doped materials is strongly increased, since the oxidation of CO is largely shifted to the Pt oxide clusters. Unlike for undoped SnO_2, the oxidation of CO in humid air is still facile on the Pt-doped materials. Due to electronic coupling of the Pt oxide clusters and SnO_2, the depletion layer at the SnO_2 surface is controlled by the composition of the Pt oxide clusters. Thus the band bending depends on changes in the composition of the Pt oxide clusters.

In dry air or oxygen rich gas mixtures, the oxidation of CO, i.e. reduction of the surface, and the re-oxidation of the surface are improved and in sum the surface composition is less affected by the reaction. Consequently, there is no change in the Pt oxide clusters' composition and the surface band bending. Thus, only minor changes of the sensor resistance are observed in these conditions.

If the re-oxidation of the clusters by atmospheric oxygen is hindered, either due to a low oxygen concentration in the atmosphere or the interference of water vapour with the oxygen adsorption, the composition of the Pt oxide is changed and CO oxidation in maintained by involving oxygen from the supporting SnO_2. But since the composition of the Pt oxide clusters now changes, the band bending decreases and a distinct change of the sensor resistance is observed. However, in typical applications conditions, i.e. in humid air, the Pt oxide clusters remain oxidized; a change of the oxidation state is only observed in oxygen lean atmospheres, although changes in the occupation of d-states are observed by operando XANES (Figure 47).

The described effects are more pronounced on the 2.0 wt% Pt-doped SnO_2 material, and one can distinguish the three following situations summarized in Figure 53.

(a) If the re-oxidation of the Pt oxide clusters is not hindered, the composition is not changed due to CO oxidation. Thus, the electronic interface of the Pt oxide clusters and SnO_2, and consequently the sensor resistance are not changed.

(b) If the re-oxidation is hindered, the composition of the Pt oxide clusters is changed, affecting the electron interaction of Pt oxide clusters and SnO_2. As a result of the changed stoichiometry of the Pt oxide clusters, fewer electrons are trapped on the corresponding acceptor state and resulting decrease of the surface band bending causes a sensor signal.

(c) If the re-oxidation is no longer possible, a reduction of the Pt oxide clusters to metallic Pt is observed and the electronic acceptor state and the corresponding band bending disappears. This causes a strong sensor signal. There is no longer an electronic interaction of the Pt oxide clusters and SnO_2, and the effect of CO on the SnO_2 is similar to that on an undoped surface, i.e. the surface gets reduced and an accumulation layer is formed.

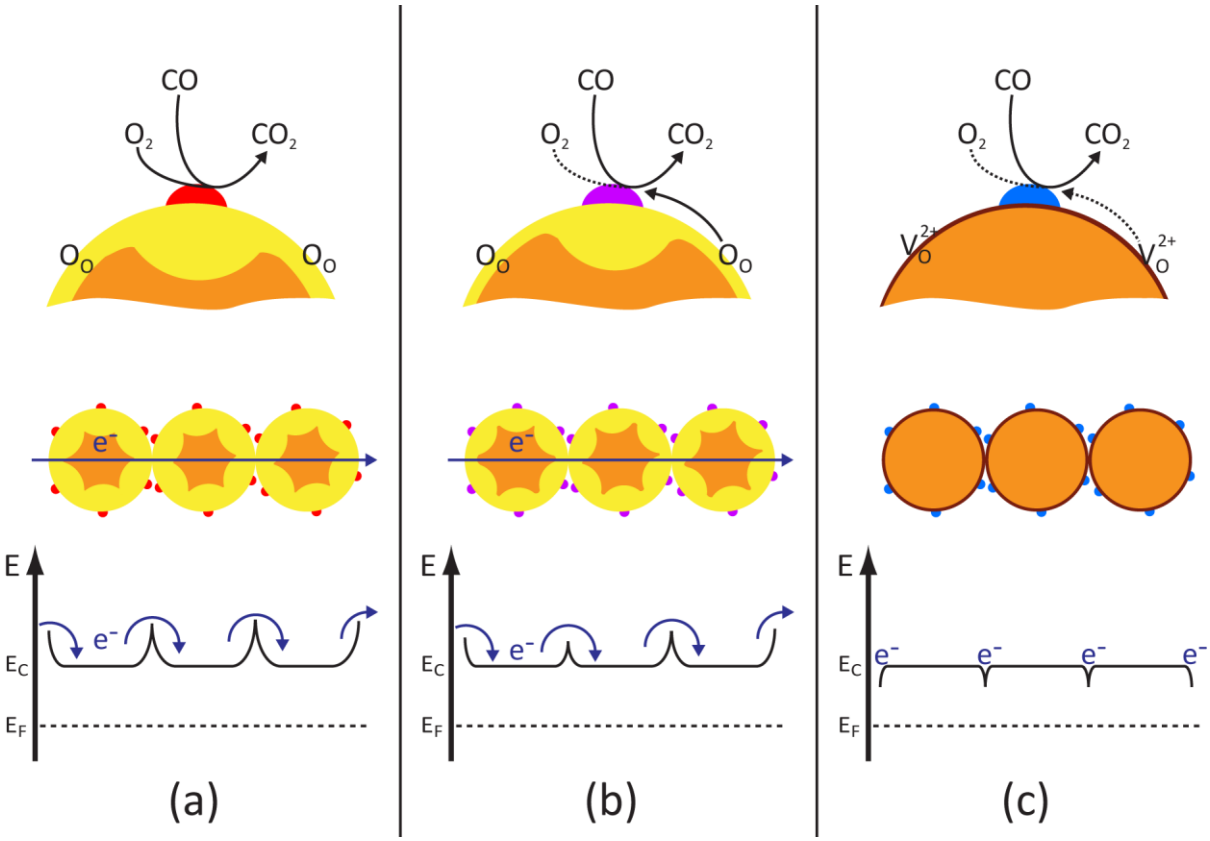

Figure 53. Proposed model for the gas reception and transduction mediated by Pt oxide clusters on the SnO_2 surface. The schematic surface reactions are shown in the top row. The dotted arrows indicate a decrease or inhibition of the corresponding reaction step. Fully oxidized Pt oxide clusters are shown in red, a change of the composition (increased oxygen deficiency) is indicated by a purple colouring of the cluster and metallic Pt is shown in blue. The lower section illustrates the impact of the surface processes on the space charge layers - depletion layer (yellow) , accumulation layer (brown) and unaffected bulk (orange) and the consequences for the back to back Schottky barriers. A description of the three different situations is found in the text.

7. Summary

The first part of this work focuses on gas reception on pristine SnO_2, namely the nature of the active oxygen and electron donor species, as well as the interfering effect of water vapour. Earlier concepts assumed that in dry air ionosorbed oxygen acts as an electron acceptor while in the absence of oxygen adsorbed target gases act as electron donors. This model was fundamentally questioned, since the observed electronic properties of pristine SnO_2 suggested the formation of such donor species in humid air, i.e. in a high oxygen background. By using operando spectroscopies, namely DRIFTS and UV/vis-DRS, this work demonstrated that in dry and humid air or in the absence of oxygen the same surface species are involved in the reception of target gases, namely lattice oxygen. The electronic properties of SnO_2 are controlled by the surface concentration of oxygen vacancies, which act as an electron donor. The situation at the pristine SnO_2 surface is determined by the interplay of reduction and (re-)oxidation reactions, which depends directly on the atmospheric composition:

- In dry air the oxidation of the surface dominates and a low oxygen vacancy concentration is found. In the presence of a reducing gas like CO or H_2, surface oxygen is consumed due to the oxidation of the gas, forming CO_2 or H_2O, respectively. A massive reduction of the surface is countered by the simultaneous re-oxidation of the surface by atmospheric oxygen.
- In the absence of oxygen, the exposure of reducing gases causes a reduction of the surface but, due to the lack of atmospheric oxygen, a re-oxidation of the surface is not possible. As a consequence, the oxidation of CO or H_2 comes almost to a standstill and the high concentration of oxygen vacancies on the reduced surface causes a strong decrease of the sensor resistance.
- In humid air, the oxidation of the surface is hindered by the presence of water vapour leading to an initially decreased concentration of reactive oxygen species at the surface. The oxidation of CO or H_2 is still possible, but is strongly decreased. Thus, less oxygen vacancies are formed compared to a similar gas exposure in dry air and, as a result, a lower resistance change is observed.

Due to its relevance for gas sensing in ambient conditions and not yet fully understood chemistry, the effect of water vapour on pristine SnO_2 was further studied by in-situ and operando DRIFTS at different operation temperatures. On the studied pristine SnO_2 three regions with different dominant water adsorption processes were found depending on the operation temperature. At temperatures below 100 °C the physisorption of water dominates. In an intermediate temperature range up to 300 °C water is associatively adsorbed by forming H-bonds with pre-existing hydroxyl groups and/or surface oxygen species. With the onset of desorption of pre-existing hydroxyl groups

above 300 °C, dissociative water adsorption is found to be dominant, by regenerating the desorbed hydroxyl groups. The onset of the hydroxyl groups desorption and the transition between associative and dissociative adsorption depends strongly on the composition of the SnO_2 surface, namely on the concentration of oxygen vacancies, or, respectively, surface oxygen, and of pre-existing hydroxyl groups. These surface properties are determined by the preparation of the material but are also changed due to aging effects. Regarding their effect on the electronic properties of SnO_2 the following conclusions are made:

- In the range of associative water adsorption a reducing effect of water is observed, which is explained by an electronic donor of the adsorbed water molecules. Above the onset of oxygen ionosorption the displacement of surface oxygen, also described as inhibition of ionosorption, causes a strong additional reducing effect.
- With increasing dissociative water adsorption a decreased reducing effect of water is observed. This is explained by a strong decrease of the associatively adsorbed water, which now forms surface hydroxyl groups (dissociative adsorption) by a, in sum, charge neutral reaction with surface oxygen.

The second part of this work is dedicated to the impact of Pt on the gas reception and transduction mechanism of SnO_2. As a first step, the structure of the Pt loadings was investigated using XAS and TEM. The Pt loadings form small Pt oxide clusters, which are well dispersed and in close contact with the SnO_2 surface. TPR-XAS shows that the Pt oxide clusters are easily reduced in the absence of atmospheric oxygen indicating that Pt is only present at the surface and not strongly incorporated in the SnO_2 lattice; at an operation temperature of 300°C the Pt oxide clusters are easily reduced and re-oxidized depending on the gas atmosphere. During gas sensing, i.e. in a high oxygen background (20.5 vol%), Pt remains oxidized, although the recorded operando XANES spectra reveal a decrease in the population of unoccupied d-states of Pt. As shown by CO oxidation measurements the presence of Pt strongly enhances the reactivity of the material and, unlike undoped SnO_2, sustains a high level of CO oxidation in humid air. However, the evaluation of the gas sensing performance shows that the sensor signals decrease with increasing Pt loading, and that only in humid air this increased reactivity results in higher sensor signals than on pristine SnO_2. In fact, these observations imply that there is an impact of Pt on the surface chemistry and consequently the gas reception. In order to further examine the changes in the surface chemistry the Pt-doped SnO_2 samples were studied by operando DRIFTS. It was found that CO is oxidized on the Pt oxide clusters by a Mars-van-Krevelen mechanism. In dry air the Pt oxide clusters are easily re-oxidized and the oxidation of CO does not change the surface, i.e. there are no changes that can be transduced into a sensor signal. In humid air it was found that the oxidation of CO causes clear changes of the surface of both oxides - Pt oxide clusters and SnO_2. All or some of these changes cause a change of the electronic properties of the surface, i.e.

a sensor signal. A more detailed image was obtained by DRIFTS measurements done in low oxygen backgrounds, which verified a Mars-van-Krevelen mechanism for the CO oxidation on the Pt oxide clusters but also showed a strong electronic coupling of the Pt oxide clusters and SnO_2. Consequently, not only the gas reception is changed by the Pt oxide cluster but also the transduction changes: Due to the electronic coupling the space charge layer is no longer determined by the concentration of oxygen vacancies on SnO_2 but rather by the electronic coupling of the two oxides, which depends on the composition of the Pt oxide clusters. In conclusion, the found effect of the Pt dopant is the one described by the Fermi-level control model.

In sum the presented results on undoped and Pt-doped SnO_2 show a clear correlation of the reactivity of the material and the obtained sensor signals. Based on the definition of a catalyst, the observed correlation can be described as follows:

- If the material shows no or a very low reactivity, e.g. in the case of undoped SnO_2 in the presence of water vapour, the lack of an interaction prevents any gas reception and thus any sensing effect.
- If the material is very reactive, e.g. in the case of Pt-doped SnO_2 in dry air, the material is a typical catalyst, i.e. it facilitates the reaction but is not changed after completing the reaction. Although there is a very strong interaction of the target gas with the surface, the surface remains almost the same and consequently there are no changes that can be transduced into a sensor signal
- In conclusion, a suitable sensor material should have a moderate reactivity. The surface reaction has to cause temporary, i.e. fully reversible, changes of the surface, which are transduced into a sensor signal. Such situations are found in the case of undoped SnO_2 in dry air or Pt-doped SnO_2 samples in humid air, i.e. the suitability of a material is not only determined by its intrinsic properties; in fact, the specific conditions in the environment and the resulting reactivity of a material determine its sensing performance.

8. Outlook

The results presented in this work demonstrate the potential of operando spectroscopies to study gas sensing materials. In the future, already applied operando techniques should be improved by more sophisticated experimental designs, like time-resolved measurements, modulation excitation spectroscopy or the extended use of isotopic labelling, which will allow a refined identification of actively involved and spectator species. The still expanding tool-box of operando techniques for gas sensor research offers new insights into fundamental processes of gas sensors. The rational combination of these techniques will help to establish structure-function-relationships thus providing the basis for knowledge-based design of new sensing materials and sensor devices.

9. References

[1] A. Gurlo, N. Barsan, and U. Weimar, “Gas Sensors Based on Semiconducting Metal Oxides,” in *Metal Oxides - Chemistry and Applications*, J. L. G. Fierro, Ed. CRC Press, 2006, pp. 683–738.

[2] R. Jaaniso and O. K. Tan, *Semiconductor Gas Sensors*. Woodhead Publishing Limited, 2013.

[3] K. Ihokura and J. Watson, *The Stannic Oxide Gas Sensor: Principles and Applications*, First. CRS Press, Inc., 1994.

[4] D. Briand, “Micromachined semicondcutor gas sensors,” in *Semiconductor Gas Sensors*, 1st ed., R. Jaaniso and K. O. Tan, Eds. Woodhead Publishing Series in Electronics and Optical Materials Number 38, 2013, pp. 220–260.

[5] R. A. Potyrailo, “Multivariable Sensors for Ubiquitous Monitoring of Gases in the Era of Internet of Things and Industrial Internet,” *Chem. Rev.*, vol. 116, no. 19, pp. 11877–11923, 2016.

[6] N. Barsan, D. Koziej, and U. Weimar, “Metal oxide-based gas sensor research: How to?,” *Sensors Actuators B Chem.*, vol. 121, no. 1, pp. 18–35, Jan. 2007.

[7] H.-J. Kim and J.-H. Lee, “Highly sensitive and selective gas sensors using p-type oxide semiconductors: Overview,” *Sensors Actuators B Chem.*, vol. 192, pp. 607–627, 2014.

[8] A. Cabot, J. Arbiol, J. R. Morante, U. Weimar, N. Barsan, and W. Göpel, “Analysis of the noble metal catalytic additives introduced by impregnation of as obtained SnO2 sol – gel nanocrystals for gas sensors,” *Sensors Actuators B Chem.*, vol. 70, no. 1–3, pp. 87–100, 2000.

[9] A. Cabot, A. Diéguez, A. Romano-Rodriguez, J. R. Morante, and N. Barsan, “Influence of the catalytic introduction procedure on the nano-SnO2 gas sensor performances Where and how stay the catalytic atoms?,” *Sensors Actuators B Chem.*, vol. 79, no. 2–3, pp. 98–106, 2001.

[10] A. Diéguez, A. Romano-Rodriguez, J. R. Morante, J. Kappler, N. Barsan, and W. Göpel, “Nanoparticle engineering for gas sensor optimization: Improved sol-gel fabricated nanocrystalline SnO2 thick film gas sensor for NO2 detection by calcination, catalytic metal introduction and grinding treatments,” *Sensors Actuators, B Chem.*, vol. 60, no. 2, pp. 125–137, Nov. 1999.

[11] A. Diéguez, A. Vilà, A. Cabot, A. Romano-Rodriguez, J. R. Morante, J. Kappler, N. Barsan, U. Weimar, and W. Göpel, “Influence on the gas sensor performances of the metal chemical states introduced by impregnation of calcinated SnO2 sol-gel nanocrystals,” *Sensors Actuators B Chem.*, vol. 68, no. 1–3, pp. 94–99, 2000.

[12] D. Kohl, “Surface Processes in the Dectection of Reducing Gases with SnO2-based Devices,” *Sensors and Actuators*, vol. 18, pp. 71–113, 1989.

[13] W. Göpel, “Solid-state chemical sensors: atomistic models and research trends,” *Sensors and Actuators*, vol. 16, pp. 167–193, 1989.

[14] W. Göpel and K.-D. Schierbaum, “SnO2 sensors: current status and future prospects,” *Sensors Actuators B Chem.*, no. 26–27, pp. 1–12, 1995.

[15] A. Gurlo and R. Riedel, “In situ and operando spectroscopy for assessing mechanisms of gas sensing.,” *Angew. Chem. Int. Ed. Engl.*, vol. 46, no. 21, pp. 3826–48, Jan. 2007.

[16] M. A. Bañares, “Operando methodology: combination of in situ spectroscopy and simultaneous activity measurements under catalytic reaction conditions,” *Catal. Today*, vol. 100, no. 1–2, pp. 71–77, Feb. 2005.

[17] B. M. Weckhuysen, “Determining the active site in a catalytic process: Operando spectroscopy

is more than a buzzword," *Phys. Chem. Chem. Phys.*, vol. 5, no. 20, p. 4351, 2003.

[18] A. Urakawa, "Trends and advances in Operando methodology," *Curr. Opin. Chem. Eng.*, vol. 12, pp. 31–36, 2016.

[19] A. Gurlo, "Interplay between O2 and SnO2: oxygen ionosorption and spectroscopic evidence for adsorbed oxygen.," *ChemPhysChem*, vol. 7, no. 10, pp. 2041–52, Oct. 2006.

[20] K. Großmann, S. Wicker, U. Weimar, and N. Barsan, "Impact of Pt additives on the surface reactions between SnO2, water vapour, CO and H2; an operando investigation.," *Phys. Chem. Chem. Phys.*, vol. 15, no. 44, pp. 19151–8, Nov. 2013.

[21] D. Koziej, M. Hübner, N. Barsan, U. Weimar, M. Sikora, and J.-D. Grunwaldt, "Operando X-ray absorption spectroscopy studies on Pd-SnO2 based sensors," *Phys. Chem. Chem. Phys.*, vol. 11, no. 38, pp. 8620–8625, Oct. 2009.

[22] M. Hübner, D. Koziej, M. Bauer, N. Barsan, K. O. Kvashnina, M. D. Rossell, U. Weimar, and J.-D. Grunwaldt, "The structure and behavior of platinum in SnO2-based sensors under working conditions.," *Angew. Chemie (International ed. English))*, vol. 50, no. 12, pp. 2841–4, Mar. 2011.

[23] M. Hübner, N. Barsan, and U. Weimar, "Influences of Al, Pd and Pt additives on the conduction mechanism as well as the surface and bulk properties of SnO2 based polycrystalline thick film gas sensors," *Sensors Actuators B Chem.*, vol. 171–172, pp. 172–180, Aug. 2012.

[24] M. Hübner, D. Koziej, J.-D. Grunwaldt, U. Weimar, and N. Barsan, "An Au clusters related spill-over sensitization mechanism in SnO2-based gas sensors identified by operando HERFD-XAS, work function changes, DC resistance and catalytic conversion studies.," *Phys. Chem. Chem. Phys.*, vol. 14, no. 38, pp. 13249–13254, Oct. 2012.

[25] D. Degler, S. Rank, S. Müller, H. W. Pereira de Carvalho, J. Grunwaldt, U. Weimar, and N. Barsan, "Gold-Loaded Tin Dioxide Gas Sensing Materials: Mechanistic Insights and the Role of Gold Dispersion," *ACS Sensors*, vol. 1, no. 11, pp. 1322–1329, 2016.

[26] "Operando Methods," 2017. [Online]. Available: https://weimar.ipc.uni-tuebingen.de/index.php?id=833. [Accessed: 28-Apr-2017].

[27] A. Hulanicki, S. Glab, and F. Ingman, "Chemical sensors: definitions and classification," *Pure Appl. Chem.*, vol. 63, no. 9, pp. 1247–1250, 1991.

[28] J. Kappler, "Characterisation of high-performance SnO2 gas sensors for CO detection by in situ techniques," Eberhard Karls Universität Tübingen, 2001.

[29] J. S. Wilson, *Sensor Technology Handbook*, 1st ed. Burlington (USA), Oxford (UK): Elsevier Inc., 2005.

[30] P. Gründler, *Chemical Sensors - An Introduction for Scientists and Engineers*. Berlin (Ger), Heidelberg (Ger), New York (USA): Springer-Verlag Berlin Heidelberg, 2007.

[31] M. Batzill and U. Diebold, "The surface and materials science of tin oxide," *Prog. Surf. Sci.*, vol. 79, no. 2–4, pp. 47–154, 2005.

[32] Z. Jorzebski and J. Marton, "Physical Properties of SnO2 Materials - I Preparation and Defect Structure," *J. Electrochem. Soc.*, vol. 123, no. 7, p. 199C–205C, 1976.

[33] W. H. Baur, "Über die Verfeinerung der Kristallstrukturbestimmung einiger Vertreter des Rutiltyps: TiO2, SnO2, GeO2 und MgF2," *Acta Cryst.*, vol. 9, no. 6, pp. 515–520, 1956.

[34] A. Diéguez, A. Romano-Rodriguez, A. Vilà, and J. R. Morante, "The complete Raman spectrum of nanometric SnO2 particles," *J. Appl. Phys.*, vol. 90, no. 3, pp. 1550–1557, 2001.

[35] T. Hirata, K. Ishioka, M. Kitajima, and H. Doi, “Concentration dependence of optical phonons in the TiO2-SnO2 system,” *Phys. Rev. B*, vol. 53, no. 13, pp. 8442–8448, 1996.

[36] P. Merle, J. Pascual, J. Camassel, and H. Mathieu, “Uniaxial-stress dependence of the first-order Raman spectrum of rutile. I. Experiments,” *Phys. Rev. B*, vol. 21, no. 4, pp. 1617–1626, 1980.

[37] P. Peercy and B. Morosin, “Pressure and Temperature Dependences of the Raman-Active Phonons in SnO2,” *Phys. Rev. B*, vol. 7, no. 6, pp. 2779–2786, 1973.

[38] G. A. Samara and P. S. Peercy, “Pressure and temperature dependence of the static dielectric constants and raman spectra of TiO2 (Rutile),” *Phys. Rev. B*, vol. 7, no. 3, pp. 1131–1148, 1973.

[39] R. S. Katiyar, “Dynamics of Rutile Structure I. Space group representation and the normal mode analysis,” *J. Phys. C. Solid State Phys*, vol. 3, p. 1087, 1970.

[40] R. S. Katiyar, P. Dawson, M. M. Hargreave, and G. R. Wilkinson, “Dynamics of the rutile structure III. Lattice dynamics , infrared and Raman spectra of SnO2,” *J. Phys. C Solid State Phys.*, vol. 4, pp. 2421–2431, 1971.

[41] R. Summitt, “Infrared absorption in single-crystal stannic oxide: Optical lattice-vibration modes,” *J. Appl. Phys.*, vol. 39, no. 8, pp. 3762–3767, 1968.

[42] R. Summitt and N. F. Borrelli, “Infrared Absorption in Single Crystal Stannic Oxide,” *J. Phys. Chem. Solids*, vol. 26, pp. 921–925, 1965.

[43] Z. Jorzebski and J. Marton, “Physical Properties of SnO2 Materials - III Optical Properties,” *J. Electrochem. Soc.*, vol. 123, no. 10, p. 333C–346C, 1976.

[44] S. Munnix and M. Schmeits, “Electronic structure of tin dioxide surfaces,” *Phys. Rev. B*, vol. 27, no. 12, pp. 7624–7635, 1983.

[45] J. M. Themlin, R. Sporken, J. Darville, R. Caudano, J. M. Gilles, and R. L. Johnson, “Resonant-photoemission study of SnO2: Cationic origin of the defect band-gap states,” *Phys. Rev. B*, vol. 42, no. 18, pp. 11914–11925, 1990.

[46] Z. Jorzebski and J. Marton, “Physical Properties of SnO2 Materials - II Electrical Properties,” *J. Electrochem. Soc.*, vol. 123, no. 9, p. 299C–310C, 1976.

[47] M. Batzill, “Surface Science Studies of Gas Sensing Materials: SnO2,” *Sensors*, vol. 6, pp. 1345–1366, 2006.

[48] K. W. Kolasinski, *Surface Science - Foundations of Catalysis and Nanoscience*, 2nd ed. John Wiley & Sons Ltd., 2008.

[49] P. Atkins and J. de Paula, *Physical Chemistry*, 8th ed. Oxford University Press, 2006.

[50] S. R. Morrison, *The Chemical Physics of Surfaces*. Plenum Press, New York, 1977.

[51] A. Many, Y. Goldstein, and N. B. Grover, *Semiconductor Surfaces*, 2nd editio. North-Holland Publishing Company, Amsterdam London, 1971.

[52] N. Barsan and U. Weimar, “Conduction Model of Metal Oxide Gas Sensors,” *J. Electroceramics*, vol. 7, no. 3, pp. 143–167, 2001.

[53] N. Barsan, M. Hübner, and U. Weimar, “Conduction mechanisms in SnO2 based polycrystalline thick film gas sensors exposed to CO and H2 in different oxygen backgrounds,” *Sensors Actuators B Chem.*, vol. 157, no. 2, pp. 510–517, Oct. 2011.

[54] K. Tabata, T. Kawabe, Y. Yamaguchi, and Y. Nagasawa, “Chemisorbed oxygen species over the (110) face of SnO2,” *Catal. Surv. from Asia*, vol. 7, no. 4, pp. 251–259, 2003.

[55] U. Pulkkinen, T. T. Rantala, T. S. Rantala, and V. Lantto, “Simulation of oxygen exchange of SnO2 surface,” *Comput. Phys. Commun.*, vol. 121--122, p. 720, 1999.

[56] X. Wang, H. Qin, Y. Chen, and J. Hu, “Sensing Mechanism of SnO2 (110) Surface to CO : Density Functional Theory Calculations,” *J. Chem. Phys.*, vol. 118, no. 49, pp. 28548–28561, 2014.

[57] J.-M. Ducéré, A. Hemeryck, A. Estève, M. D. Rouhani, G. Landa, P. Ménini, C. Tropis, A. Maisonnat, P. Fau, and B. Chaudret, “A computational chemist approach to gas sensors: modeling the response of SnO2 to CO, O2, and H2O gases.,” *J. Comput. Chem.*, vol. 33, no. 3, pp. 247–58, Jan. 2012.

[58] S. Saukko, U. Lassi, V. Lantto, M. Kroneld, S. Novikov, P. Kuivalainen, T. T. Rantala, and J. Mizsei, “Experimental studies of O2-SnO2 surface interaction using powder, thick films and monocrystalline thin films,” *Thin Solid Films*, vol. 490, no. 1, pp. 48–53, 2005.

[59] N. Yamazoe, J. Fuchigami, M. Kishikawa, and T. Seiyama, “Interactions of tin oxide surface with O2, H2O and H2,” *Surf. Sci.*, vol. 86, pp. 335–344, 1979.

[60] Davydov Anatoli A., “IR spectroscopic study of oxygen states and its reactivity on the surface of tin dioxide,” *J. Appl. Spectrosc.*, vol. 56, no. 4, pp. 365–371, 1992.

[61] T. A. Gundrizer and Davydov Anatoli A., “IR spectra of oxygen adsorbed on SnO2,” *React. Kinet. Catal. Lett.*, vol. 3, pp. 63–70, 1975.

[62] S.-C. Chang, “Oxygen Chemisorption on tin oxide: Correlation between electrical conductivity and EPR measurements.pdf,” *J. Vac. Sci. Technol.*, vol. 17, no. 1, pp. 366–369, 1980.

[63] A. Marikutsa, M. Rumyantseva, D. Frolov, I. Morozov, A. Boltalin, A. Fedorova, I. Petukhov, L. Yashina, E. Konstantinova, E. Sadovskaya, A. Abakumov, Y. Zubavichus, and A. Gaskov, “Role of PdO x and RuO y Clusters in Oxygen Exchange between Nanocrystalline Tin Dioxide and the Gas Phase,” *J. Chem. Phys.*, no. 117, pp. 23858–23867, 2013.

[64] M. Egashira, M. Nakashima, S. Kawasumi, and T. Selyama, “Temperature programmed desorption study of water adsorbed on metal oxides. 2. Tin oxide surfaces,” *J. Phys. Chem.*, vol. 85, no. 26, pp. 4125–4130, 1981.

[65] S. Lenaerts, J. Roggen, and G. Maes, “FT-IR characterization of tin dioxide gas sensor materials under working conditions,” *Spectrochim. Acta*, vol. 51, no. 5, pp. 883–894, 1995.

[66] E. W. Thornton and P. G. Harrison, “Tin Oxide Surfaces - Part 1.-Surface Hydroxyl Groups and the Chemisorption of Carbon Dioxide and Carbon Monoxide on Tin(IV) Oxide,” *J. Chem. Soc. Faraday Trans. 1 Phys. Chem. Condens. Phases*, vol. 71, pp. 461–472, 1974.

[67] P. G. Harrison and A. Guest, “Tin Oxide Surface Part 17. - An Infrared and Thermogravimetric Analysis of the Thermal Dehydration of Tin(IV) Oxide Gel,” *J. Chem. Soc. Faraday Trans. 1 Phys. Chem. Condens. Phases*, vol. 83, no. 11, pp. 3383–3397, 1987.

[68] S. Wicker, “Influence of humidity on the gas sensing characteristics of SnO2 - DRIFTS investigation of different base materials and dopants Dissertation,” Eberhard Karls Universität Tübingen, 2016.

[69] V. E. Heinrich and P. A. Cox, *Surface Science of Metal Oxides*, 1st ed. Cambridge University Press, 1994.

[70] N. Yamazoe, K. Suematsu, and K. Shimanoe, “Two types of moisture effects on the receptor function of neat tin oxide gas sensor to oxygen,” *Sensors Actuators, B Chem.*, vol. 176, pp. 443–452, 2013.

[71] G. Santarossa, K. R. Hahn, and A. Baiker, “Free energy and electronic properties of water

adsorption on the SnO2 (110) surface," *Langmuir*, vol. 2, no. 110, pp. 5487–5499, 2013.

[72] V. A. Gercher and D. F. Cox, "Water adsorption on stoichiometric and defective SnO2 (110) surfaces," *Surf. Sci.*, vol. 332, pp. 177–184, 1995.

[73] M. Batzill, W. Bergermayer, I. Tanaka, and U. Diebold, "Tuning the chemical functionality of a gas sensitive material: Water adsorption on SnO2(101)," *Surf. Sci.*, vol. 600, no. 4, pp. 29–32, Feb. 2006.

[74] D. Koziej, K. Thomas, N. Barsan, F. Thibault-Starzyk, and U. Weimar, "Influence of annealing temperature on the CO sensing mechanism for tin dioxide based sensors–Operando studies," *Catal. Today*, vol. 126, no. 1–2, pp. 211–218, Aug. 2007.

[75] P. G. Harrison and A. Guest, "Tin Oxide Surfaces Part 18. - Infrared Study of the Adsorption of very low Levels (2&50 ppm) of Carbon Monoxide in Air on to Tin(IV) Oxide Gel," *J. Chem. Soc. Faraday Trans. 1 Phys. Chem. Condens. Phases*, vol. 85, no. 8, pp. 1897–1906, 1989.

[76] D. Amalric-Popescu and F. Bozon-Verduraz, "Infrared studies on SnO2 and Pd/SnO2," *Catal. Today*, vol. 70, no. 1–3, pp. 139–154, 2001.

[77] N. Sergent, P. Gélin, L. Périer-Camby, H. Praliaud, and G. Thomas, "FTIR study of low-temperature CO adsorption on high surface area tin(IV) oxide: Probing Lewis and Bronsted acidity," *Phys. Chem. Chem. Phys.*, vol. 4, no. 19, pp. 4802–4808, Sep. 2002.

[78] N. Barsan, M. Schweizer-Berberich, and W. Göpel, "Fundamental and practical aspects in the design of nanoscaled SnO2 gas sensors : a status report," *Fresenius J. Anal. Chem.*, vol. 365, pp. 287–304, 1999.

[79] M. E. Franke, T. J. Koplin, and U. Simon, "Metal and metal oxide nanoparticles in chemiresistors: Does the nanoscale matter?," *Small*, vol. 2, no. 1, pp. 36–50, 2006.

[80] N. Barsan, M. Hübner, and U. Weimar, "Conduction mechanism in semiconducting metal oxide sensing films," in *Semiconductor Gas Sensors*, 1st ed., R. Jaaniso and O. Kiang Tan, Eds. Cambridge, U.K.: Woodhead Publishing Limited, 2013, pp. 35–63.

[81] N. Barsan, M. Hübner, and U. Weimar, "Conduction meachanism in semiconducting metal oxides sensing films: impact on transduction," in *Semiconductor Gas Sensors*, 1st ed., R. Jaaniso and O. Kiang Tan, Eds. Cambridge, U.K.: Woodhead Publishing Limited, 2013, pp. 35–63.

[82] M. Hübner, "New Approaches for the Basic Understanding of Semiconducting Metal Oxide Based Gas Sensors: Sensing, Transduction and Appropriate Modeling," Eberhard Karls Universität Tübingen, 2011.

[83] S. R. Morrison, "Selectivity in semiconductor gas sensors," *Sensors and Actuators*, vol. 12, no. 4, pp. 425–440, 1987.

[84] N. Yamazoe, "New approaches for improving semiconductor gas sensors," *Sensors Actuators B Chem.*, vol. 5, no. 1–4, pp. 7–19, 1991.

[85] S. Matsushima, Y. Teraoka, N. Miura, and N. Yamazoe, "Electronic Interaction between Metal Additives and Tin Dioxide in Tin Dioxide-Based Gas Sensors," *Jpn. J. Appl. Phys.*, vol. 27, no. 10, pp. 1798–1802, 1988.

[86] N. Yamazoe, Y. Kurokawa, and T. Seiyama, "Effects of Additives on Semiconductor Gas Sensors," *Sensors Actuators B Chem.*, vol. 4, pp. 283–289, 1983.

[87] N. Yamazoe, G. Sakai, and K. Shimanoe, "Oxide semiconductor gas sensors," *Catal. Surv. from Asia*, vol. 7, no. 1, pp. 63–75, 2003.

[88] S. Rank, "The Influence of the Electrode Material on the Sensor Characteristics of SnO2 Thick

Film Gas Sensors," Eberhard Karls Universität Tübingen, 2014.

[89] Z. Zhang and J. T. Yates, "Band bending in semiconductors: Chemical and physical consequences at surfaces and interfaces," *Chem. Rev.*, vol. 112, no. 10, pp. 5520–5551, 2012.

[90] D. Degler, H. W. Pereira de Carvalho, U. Weimar, N. Barsan, D. K. Pham, L. Mädler, and J.-D. Grunwaldt, "Structure-function relationships of conventionally and flame made Pd-doped sensors studied by X-ray absorption spectroscopy and DC-resistance," *Sensors Actuators B Chem.*, vol. 219, pp. 315–323, May 2015.

[91] L. Mädler, T. Sahm, A. Gurlo, J.-D. Grunwaldt, N. Barsan, U. Weimar, and S. E. Pratsinis, "Sensing low concentrations of CO using flame-spray-made Pt/SnO2 nanoparticles," *J. Nanoparticle Res.*, vol. 8, no. 6, pp. 783–796, Sep. 2006.

[92] N. Murata, T. Suzuki, M. Kobayashi, F. Togoh, and K. Asakura, "Characterization of Pt-doped SnO2 catalyst for a high-performance micro gas sensor," *Phys. Chem. Chem. Phys.*, vol. 15, no. 41, p. 17938, 2013.

[93] S. Emiroglu, N. Barsan, U. Weimar, and V. Hoffmann, "In situ diffuse reflectance infrared spectroscopy study of CO adsorption on SnO2," *Thin Solid Films*, vol. 391, pp. 176–185, 2001.

[94] K. Großmann, R. G. Pavelko, N. Barsan, and U. Weimar, "Interplay of H2, water vapor and oxygenat the surface of SnO2 based gas sensors – An operando investigation utilizing deuterated gases," *Sensors Actuators B Chem.*, vol. 166–167, pp. 787–793, May 2012.

[95] T. Simons, P. Chen, D. Rauch, R. Moos, and U. Simon, "Sensing catalytic conversion : Simultaneous DRIFT and impedance spectroscopy for in situ monitoring of NH3– SCR on zeolites," *Sensors Actuators B Chem.*, vol. 224, pp. 492–499, 2016.

[96] S. Sänze, A. Gurlo, and C. Hess, "Monitoring gas sensors at work: operando Raman-FTIR study of ethanol detection by indium oxide.," *Angew. Chem. Int. Ed. Engl.*, vol. 52, no. 13, pp. 3607–10, Mar. 2013.

[97] S. Sänze and C. Hess, "Ethanol Gas Sensing by Indium Oxide: An Operando Spectroscopic Raman-FTIR Study," *J. Phys. Chem. C*, vol. 118, pp. 25603–25613, 2014.

[98] D. Degler, N. Barz, U. Dettinger, H. Peisert, T. Chassé, U. Weimar, and N. Barsan, "Extending The Toolbox For Gas Sensor Research: Operando UV/vis Diffuse Reflectance Spectroscopy On SnO2-Based Gas Sensors," *Sensors Actuators B Chem.*, vol. 224, pp. 256–259, 2016.

[99] O. Hirsch, K. O. Kvashnina, L. Luo, M. J. Süess, P. Glatzel, and D. Koziej, "High-energy resolution X-ray absorption and emission spectroscopy reveals insight into unique selectivity of La-based nanoparticles for CO2," *Proc. Natl. Acad. Sci.*, p. 201516192, 2015.

[100] D. Koziej, N. Barsan, V. Hoffmann, J. Szuber, and U. Weimar, "Complementary phenomenological and spectroscopic studies of propane sensing with tin dioxide based sensors," *Sensors Actuators B Chem.*, vol. 108, no. 1–2, pp. 75–83, Jul. 2005.

[101] A. Oprea, N. Barsan, and U. Weimar, "Work function changes in gas sensitive materials: Fundamentals and applications," *Sensors Actuators B Chem.*, vol. 142, no. 2, pp. 470–493, Nov. 2009.

[102] N. Barsan and U. Weimar, "Understanding the fundamental principles of metal oxide based gas sensors ; the example of CO sensing with SnO2 sensors in the presence of humidity," *J. Phys. Condens. Matter*, vol. 15, pp. R813–R839, 2003.

[103] A. Oprea, A. Gurlo, N. Barsan, and U. Weimar, "Transport and gas sensing properties of In2O3 nanocrystalline thick films: A Hall effect based approach," *Sensors Actuators, B Chem.*, vol. 139, no. 2, pp. 322–328, 2009.

[104] A. Oprea, N. Barsan, and U. Weimar, “Characterization of granular metal oxide semiconductor gas sensitive layers by using Hall effect based approaches,” *J. Phys. D. Appl. Phys.*, vol. 40, no. 23, pp. 7217–7237, 2007.

[105] F. Thibault-Starzyk and F. Maugé, “Characterization of Solid Materials and Heterogeneous Catalysts - Infrared Spectroscopy,” in *Characterization of Solid Materials and Heterogeneous Catalysts, Volume 1 fo 2*, 1st editio., Weinheim (Germany): Wiley VCH, 2012, pp. 3–45.

[106] G. Wedler, *Lehrbuch der Physikalischen Chemie*, 5th editio. Weinheim (Germany): Wiley-VCH Verlag GmbH & Co. KGaA, 2004.

[107] P. G. Harrison and M. J. Willett, “The mechanism of operation of tin(iv) oxide carbon monoxide sensors,” *Nature*, vol. 332, no. 6162. pp. 337–339, 1988.

[108] S. Harbeck, A. Szatvanyi, N. Barsan, U. Weimar, and V. Hoffmann, “DRIFT studies of thick film un-doped and Pd-doped SnO2 sensors: temperature changes effect and CO detection mechanism in the presence of water vapour,” *Thin Solid Films*, vol. 436, no. 1, pp. 76–83, Jul. 2003.

[109] F. C. Jentoft, “Characterization of Solid Materials and Heterogeneous Catalysts - Ultra violet-visible and Near IR Spectroscopies,” in *Characterization of Solid Materials and Heterogeneous Catalysts, Volume 1 of 2*, 1st ed., M. Che and J. C. Védrine, Eds. Weinheim (Germany): Wiley VCH, 2012, pp. 89–140.

[110] D. Oelkrug, “Refkexionsspektroskopie,” in *Untersuchungsmethoden in der Chemie*, 2nd ed., H. Naumer and W. Heller, Eds. Stuttgart (Germany), 1990, pp. 259–268.

[111] V. Kumar, S. K. Sharma, T. P. Sharma, and V. Singh, “Band gap determination in thick films from reflectance measurements,” *Opt. Mater. (Amst).*, vol. 12, pp. 115–119, 1999.

[112] S. P. Tandon and J. P. Gupta, “Measurement of Forbidden Energy Gap of Semiconductors by Diffuse Reflectance Technique,” *Phys. Status Solidi*, vol. 38, pp. 363–367, 1970.

[113] M. Che and J. C. Vedrine, *Characterization of Solid Materials and Heterogeneous Catalysts: From Structure to Surface Reactivity*, 1st ed. Wiley VCH, 2012.

[114] Y. Iwasawa, K. Asakura, and M. Tada, *XAFS Techniques for Catalysts, Nanomaterials, and Surfaces*, 1st ed. Springer International Publishing, 2017.

[115] C. Geantet and C. Pichon, “Characterization of Solid Materials and Heterogeneous Catalysts - X-ray Absorption Spectroscopy,” in *Characterization of Solid Materials and Heterogeneous Catalysts, Volume 1 fo 2*, M. Che and J. C. Védrine, Eds. Wiley VCH, 2012, pp. 511–536.

[116] H. W. Pereira de Carvalho, D. Degler, N. Barsan, and J.-D. Grunwaldt, “Chapter 27: Sensors,” in *XAFS Techniques for Catalysts, Nanomaterials, and Surfaces*, Y. Iwasawa, K. Asakura, and M. Tada, Eds. Springer International Publsihing, 2017, pp. 383–396.

[117] J.-D. Grunwaldt, “Energy-related catalysis (block course),” 2012.

[118] M. Bauer and H. Bertagnolli, “X-Ray Absorbation Spectroscopy – The Method And Its Applications,” *Bunsen-Magazin*, vol. 9, pp. 216–231, 2007.

[119] “Keithley Model 2000 Multimeter User’s Manual,” 1994.

[120] “Keithley Model 199 System DMM Scanner Instruction Manual,” 1988.

[121] J. Kappler, A. Tomescu-Stănoiu, N. Barsan, and U. Weimar, “CO consumption of Pd doped SnO2 based sensors,” *Thin Solid Films*, vol. 391, no. 2, pp. 186–191, 2001.

[122] D. Koziej, “Phenomenological and Spectroscopic Studies on Gas Detection Mechanism of Selected Gases with Tin Dioxide Based Sensors,” Eberhard-Karl-Universität Tübingen, 2006.

[123] B. Ravel and M. Newville, “ATHENA, ARTEMIS, HEPHAESTUS: data analysis for X-ray absorption spectroscopy using IFEFFIT.,” *J. Synchrotron Radiat.*, vol. 12, no. Pt 4, pp. 537–41, Jul. 2005.

[124] M. P. Brown, R. Okawara, and E. G. Rochow, “Infrared spectra of some methyl derivatives of germanium and tin,” *Spectrochim. Acta*, vol. 16, no. 5, pp. 595–601, 1960.

[125] B. Jezowska-Trzebiatowska, J. Hanuza, and W. Wojciechowski, “Infra-red vibrational frequencies oi the X-O-X bonds for the IVth periodic group of elements Germanium compounds,” *Spectrochim. Acta*, vol. 23, no. 1962, p. 2631, 1967.

[126] L. Z. Liu, T. H. Li, X. L. Wu, J. C. Shen, and P. K. Chu, “Identification of oxygen vacancy types from Raman spectra of SnO 2 nanocrystals,” *J. Raman Spectrosc.*, vol. 43, no. 10, pp. 1423–1426, 2012.

[127] J. Rebholz, P. Bonanati, U. Weimar, and N. Barsan, “Grain shape influence on semiconducting metal oxide based gas sensor performance: modeling versus experiment.,” *Anal. Bioanal. Chem.*, vol. 406, no. 16, pp. 3977–83, Jun. 2014.

[128] S. Hahn, N. Barsan, U. Weimar, S. G. Ejakov, J. H. Visser, and R. E. Soltis, “CO sensing with SnO2 thick film sensors: role of oxygen and water vapour,” *Thin Solid Films*, vol. 436, no. 1, pp. 17–24, Jul. 2003.

[129] M. Hübner, R. G. Pavelko, N. Barsan, and U. Weimar, “Influence of oxygen backgrounds on hydrogen sensing with SnO2 nanomaterials,” *Sensors Actuators B Chem.*, vol. 154, no. 2, pp. 264–269, Jun. 2011.

[130] N. Barsan, J. Rebholz, and U. Weimar, “Conduction mechanism switch for SnO2 based sensors during operation in application relevant conditions; implications for modeling of sensing,” *Sensors Actuators B Chem.*, vol. 207, pp. 455–459, Feb. 2015.

[131] Z. Lu, D. Ma, L. Yang, X. Wang, G. Xu, and Z. Yang, “Direct CO oxidation by lattice oxygen on the SnO2 (110) surface: a DFT study,” *Phys. Chem. Chem. Phys.*, vol. 16, no. 24, pp. 12488–12494, 2014.

[132] Davydov Anatoli A., *Molecular Spectroscopy Of Oxide Catalyst Surfaces*. John Wiley & Sons, Inc., 2003.

[133] D. Degler, S. Wicker, U. Weimar, and N. Barsan, “Identifying the active oxygen species in SnO2 based gas sensing materials: an operando IR spectroscopy study,” *J. Phys. Chem. C*, vol. 119, pp. 11792–11799, 2015.

[134] P. Mars and D. W. van Krevelen, “Oxidations carried out by means of vanadium oxide catalysts,” *Chem. Eng. Sci.*, vol. 3, pp. 41–59, 1954.

[135] K. Großmann, “Detection mechanism of reducing gases and influence of water on tin dioxide based gas sensors – differences in surface chemistry between undoped and platinum doped materials,” Eberhard Karsl Universität Tübingen, 2012.

[136] B. Kamp, R. Merkle, R. Lauck, and J. Maier, “Chemical diffusion of oxygen in tin dioxide: Effects of dopants and oxygen partial pressure,” *J. Solid State Chem.*, vol. 178, no. 10, pp. 3027–3039, 2005.

[137] B. Kamp, R. Merkle, and J. Maier, “Chemical diffusion of oxygen in tin dioxide,” *Sensors Actuators B Chem.*, vol. 77, no. 1–2, pp. 534–542, 2001.

[138] D. F. Cox and T. Fryberger, “Peferential Isotopic Labeling of Lattice Oxygen Positions on the SnO2 (110) Surface,” *Surf. Sci. Lett.*, vol. 227, pp. L105–L108, 1990.

[139] D. Amalric-Popescu, J.-M. Herrmann, A. Ensuque, and F. Bozon-Verduraz, “Nanosized tin

dioxide: Spectroscopic (UV-VIS, NIR, EPR) and electrical conductivity studies," *Phys. Chem. Chem. Phys.*, vol. 3, no. 12, pp. 2522–2530, 2001.

[140] R. G. Pavelko, H. Daly, C. Hardacre, A. a Vasiliev, and E. Llobet, "Interaction of water, hydrogen and their mixtures with SnO2 based materials: the role of surface hydroxyl groups in detection mechanisms.," *Phys. Chem. Chem. Phys.*, vol. 12, no. 11, pp. 2639–47, 2010.

[141] K.-I. Choi, M. Hübner, A. Haensch, H.-J. Kim, U. Weimar, N. Barsan, and J.-H. Lee, "Ambivalent effect of Ni loading on gas sensing performance in SnO2 based gas sensor," *Sensors Actuators B Chem.*, vol. 183, pp. 401–410, Jul. 2013.

[142] N. Ma, K. Suematsu, M. Yuasa, T. Kida, and K. Shimanoe, "Effect of Water Vapor on Pd-Loaded SnO 2 Nanoparticles Gas Sensor," *ACS Appl. Mater. Interfaces*, vol. 7, no. 10, pp. 5863–5869, 2015.

[143] W. H. Robertson, E. G. Diken, E. A. Price, J. Shin, and M. A. Johnson, "Spectroscopic Determination of the OH- Solvation Shell in the OH-*(H2O)n Clusters," *Science (80-.).*, vol. 299, no. February, pp. 1367–1373, 2003.

[144] M. Morita, H. Takahashi, and K. Takahashi, "Why does the IR spectrum of hydroxide stretching vibration weaken with increase in hydration?," *Phys. Chem. Chem. Phys.*, vol. 16, pp. 23143–23149, 2014.

[145] S. Li, Z. Lu, Z. Yang, and X. Chu, "The sensing mechanism of Pt-doped SnO2 surface toward CO: A first-principle study," *Sensors Actuators B Chem.*, vol. 202, pp. 83–92, Oct. 2014.

[146] C. Liu, Q. Kuang, Z. Xie, and L. Zheng, "The effect of noble metal (Au, Pd and Pt) nanoparticles on the gas sensing performance of SnO2 -based sensors: a case study on the {221} high-index faceted SnO 2 octahedra," *CrystEngComm*, vol. 17, no. 33, pp. 6308–6313, 2015.

[147] M. Labeau, B. Gautheron, F. Cellier, M. Vallet-Regi, E. Garcia, and J. M. Gonzalez Calbet, "Pt Nanoparticles Dispersed on SnO2 Thin Films: A Microstructural Study," *J. Solid State Chem.*, vol. 102, pp. 434–439, 1993.

[148] J. Kappler, N. Barsan, U. Weimar, A. Diéguez, J. L. Alay, A. Romano-Rodriguez, J. R. Morante, and W. Göpel, "Correlation between XPS, Raman and TEM measurements and the gas sensitivity of Pt and Pd doped SnO2 based gas sensors," *Fresenius. J. Anal. Chem.*, vol. 361, no. 2, pp. 110–114, May 1998.

[149] D. Degler, S. A. Müller, D. Doronkin, D. Wang, J.-D. Grunwaldt, U. Weimar, and N. Barsan, "The Role of the Oxide-Oxide Interface for Gas Sensing with PtOx-loaded SnO2," p. in preparation, 2017.

[150] D. Degler, H. W. Pereira de Carvalho, K. O. Kvashnina, J.-D. Grunwaldt, U. Weimar, and N. Barsan, "Structure and chemistry of surface-doped Pt:SnO2 gas sensing materials," *RSC Adv.*, vol. 6, pp. 28149–28155, 2016.

[151] J. Singh, E. M. C. Alayon, M. Tromp, O. V. Safonova, P. Glatzel, M. Nachtegaal, R. Frahm, and J. A. Van Bokhoven, "Generating Highly Active Partially Oxidized Platinum during Oxidation of Carbon Monoxide over Pt/Al2O3: In Situ, Time-Resolved, and High-Energy-Resolution X-Ray Absorption Spectroscopy," *Angew. Chem. Int. Ed. Engl.*, vol. 47, no. 48, pp. 9260–9264, 2008.

[152] I. Kocemba and J. Rynkowski, "The influence of catalytic activity on the response of Pt/SnO2 gas sensors to carbon monoxide and hydrogen," *Sensors Actuators, B Chem.*, vol. 155, no. 2, pp. 659–666, 2011.

[153] S. R. Morrison, "Semiconductor gas sensors," *Sensors and Actuators*, vol. 2, pp. 329–341, 1982.

[154] Q. Ye, J. Wang, J. Zhao, L. Yan, S. Cheng, T. Kang, and H. Dai, "Pt or Pd-doped Au/SnO2

Catalysts: High Activity for Low-temperature CO Oxidation," *Catal. Letters*, vol. 138, no. 1–2, pp. 56–61, May 2010.

[155] E. Ivanova, M. Mihaylov, F. Thibault-Starzyk, M. Daturi, and K. Hadjiivanov, "FTIR spectroscopy study of CO and NO adsorption and co-adsorption on Pt/TiO2," *J. Mol. Catal. A Chem.*, vol. 274, no. 1–2, pp. 179–184, Sep. 2007.

[156] M. D. Ackermann, T. M. Pedersen, B. L. M. Hendriksen, O. Robach, S. C. Bobaru, I. Popa, C. Quiros, H. Kim, B. Hammer, S. Ferrer, and J. W. M. Frenken, "Structure and Reactivity of Surface Oxides on Pt(110) during Catalytic CO Oxidation," *Phys. Rev. Lett.*, vol. 95, no. 25, p. 255505, Dec. 2005.

[157] E. M. C. Alayon, J. Singh, M. Nachtegaal, M. Harfouche, and J. A. Van Bokhoven, "In situ XAS probes partially oxidized platinum generating high activity for CO oxidation," *J. Phys. Conf. Ser.*, vol. 190, p. 12152, Nov. 2009.

[158] E. M. C. Alayon, J. Singh, M. Nachtegaal, M. Harfouche, and J. A. Van Bokhoven, "On highly active partially oxidized platinum in carbon monoxide oxidation over supported platinum catalysts," *J. Catal.*, vol. 263, no. 2, pp. 228–238, 2009.

[159] B. L. M. Hendriksen and J. W. M. Frenken, "CO Oxidation on Pt(110): Scanning Tunneling Microscopy Inside a High-Pressure Flow Reactor," *Phys. Rev. Lett.*, vol. 89, no. 4, p. 46101, Jul. 2002.

[160] J. Singh, M. Nachtegaal, E. M. C. Alayon, J. Stötzel, and J. A. Van Bokhoven, "Dynamic structure changes of a heterogeneous catalyst within a reactor: Oscillations in co oxidation over a supported platinum catalyst," *ChemCatChem*, vol. 2, no. 6, pp. 653–657, 2010.

[161] R. Kopelent, J. A. Van Bokhoven, J. Szlachetko, J. Edebeli, C. Paun, M. Nachtegaal, and O. V. Safonova, "Catalytically Active and Spectator Ce3+ in Ceria-Supported Metal Catalysts," *Angew. Chemie - Int. Ed.*, vol. 54, no. 30, pp. 8728–8731, 2015.

10. Appendix

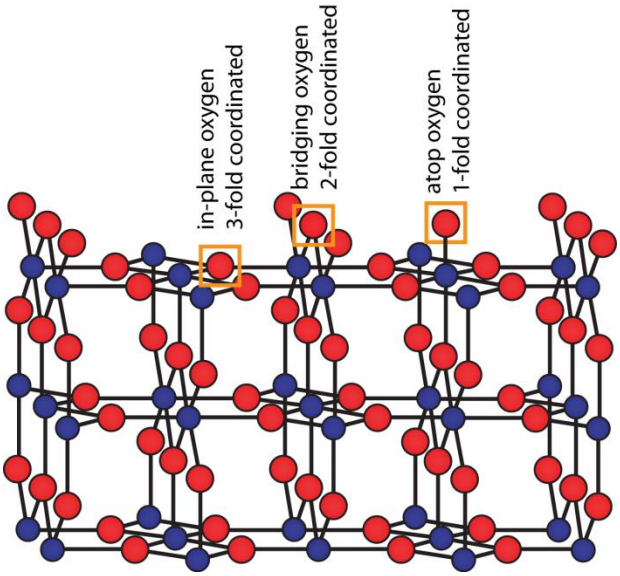

Supporting Figure 1. Ball-stick model of the (110) surface of SnO_2 with one additional atop oxygen added. The different surface oxygen species – in-plane, bridging and atop – are highlighted in the figure. Sn atoms are shown in blue and oxygen atoms in red.

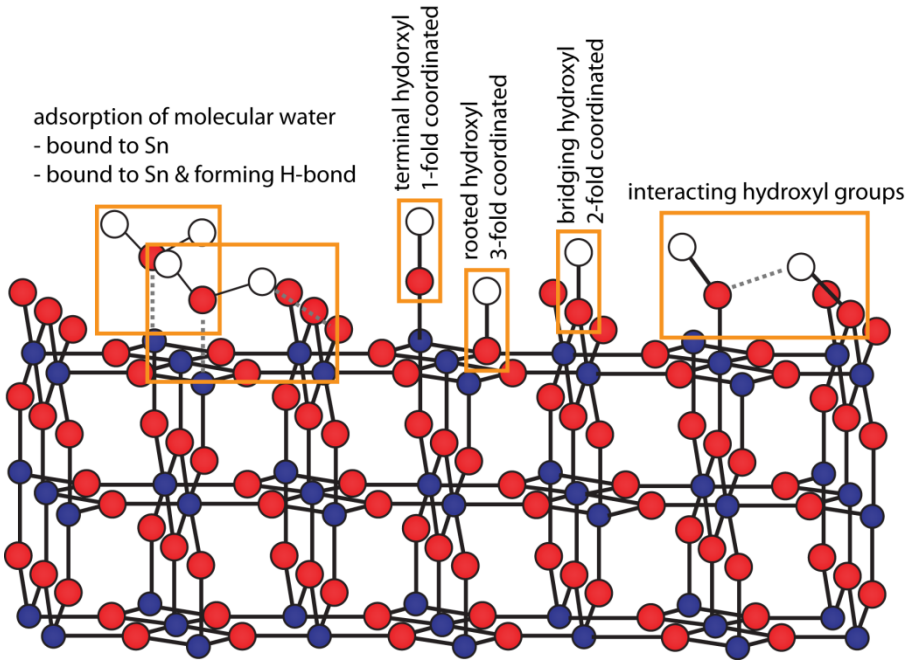

Supporting Figure 2. Ball-stick model of the (110) surface of SnO_2 with different adsorbed water species, including molecular adsorbed water (left), isolated hydroxyl groups (middle) and interacting hydroxyl groups (right). Three different isolated hydroxyl groups are found on the (110) surface: terminal, bridging and rooted, which are coordinated with one, two or three Sn atoms, respectively. Sn atoms are shown in blue, oxygen atoms in red and hydrogen atoms in white.

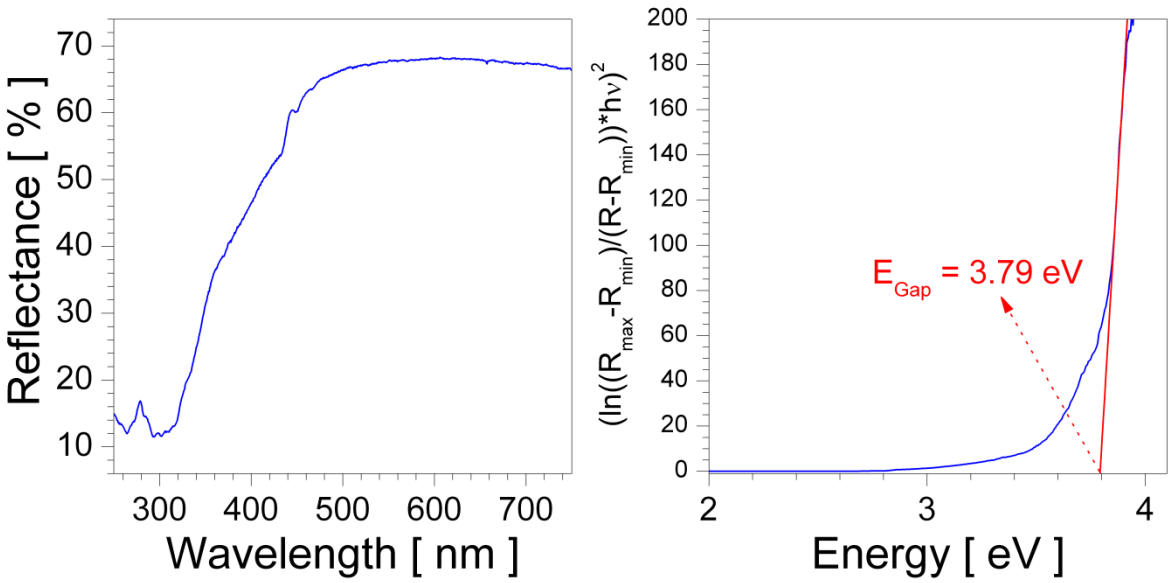

Supporting Figure 3. UV/vis diffuse reflectance spectra of pristine SnO2 recorded on a gas sensor at room-temperature (left) and the corresponding plot to estimate the optical band gap.

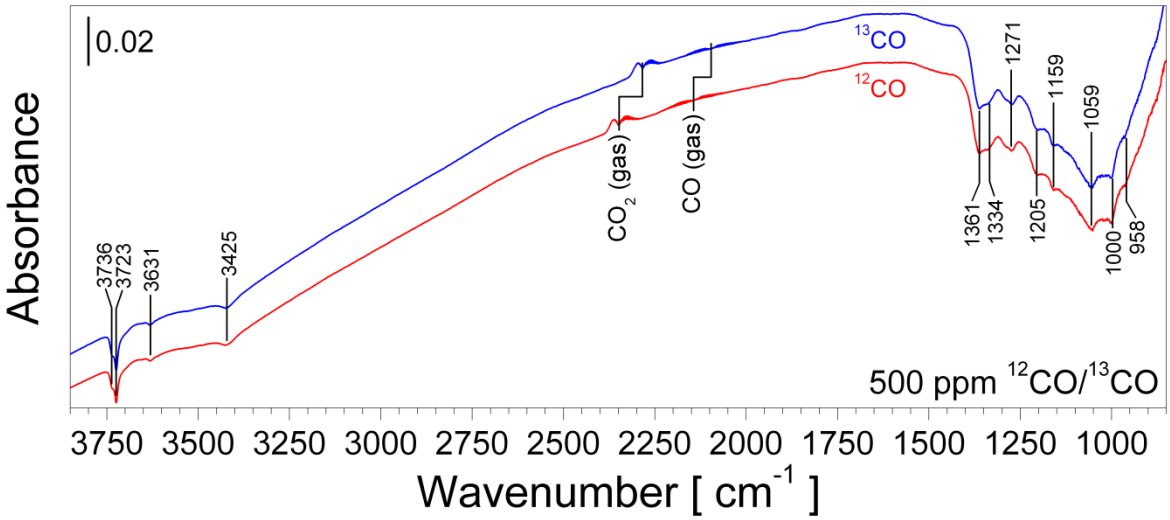

Supporting Figure 4. DRIFT spectra of undoped SnO_2 exposed to 500 ppm of ^{12}CO in dry (red) and ^{13}CO (blue) in dry air. The sensor temperature was 300 °C. The spectra were referenced to a spectrum recorded in dry.

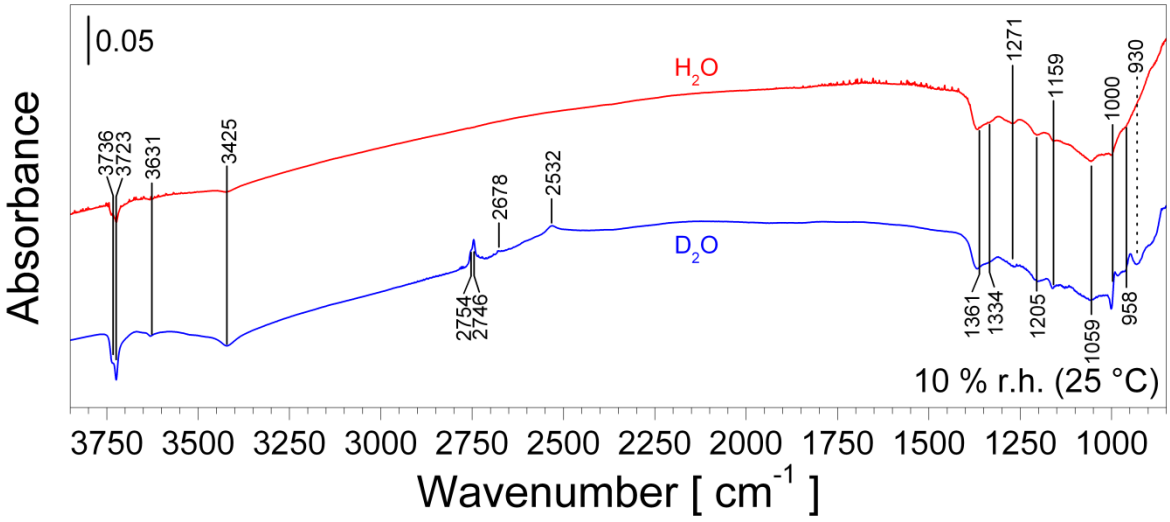

Supporting Figure 5. DRIFT spectra of undoped SnO_2 exposed to H_2O in dry (red) and D_2O (blue). The water concentration was 10 % r.h. at 25 °C. The sensor temperature was 300 °C. The spectra were referenced to a spectrum recorded in dry.

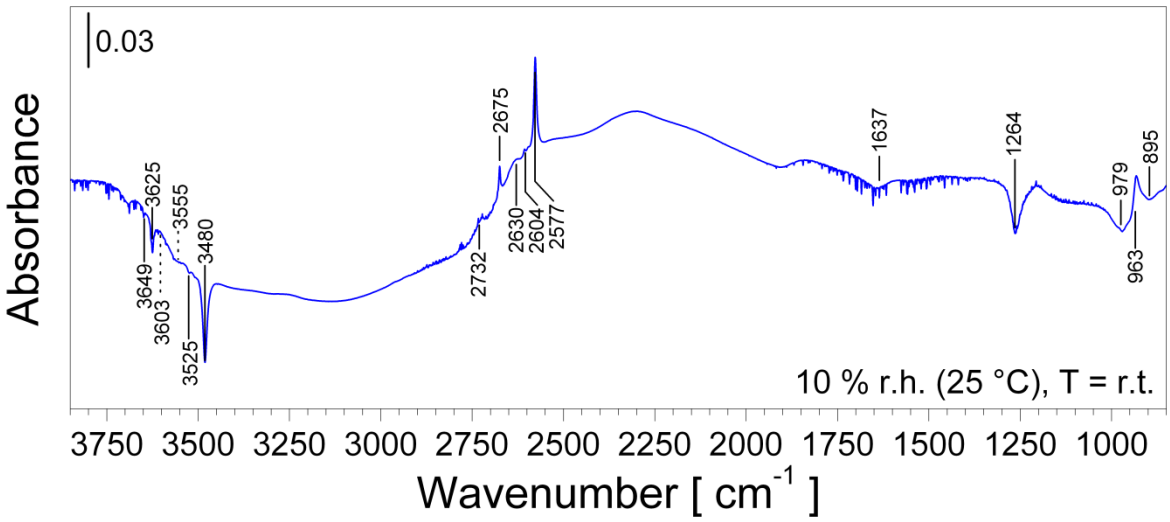

Supporting Figure 6. H_2O-D_2O exchange spectra of undoped SnO2 recorded at room temperature. The water concentration was 10 % r.h. (25 °C).

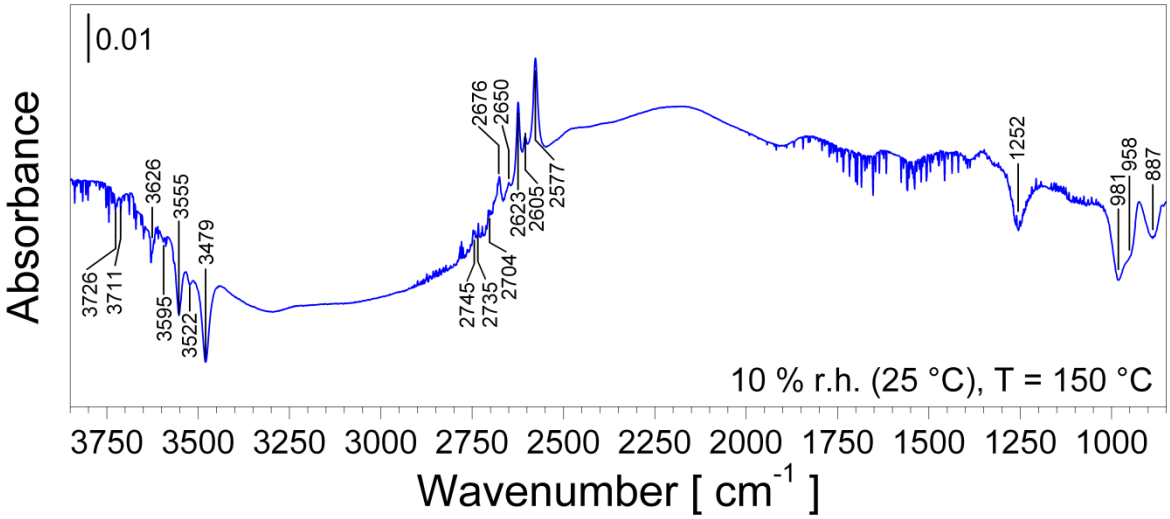

Supporting Figure 7. H_2O-D_2O exchange spectra of undoped SnO2 recorded at 150 °C. The water concentration was 10 % r.h. (25 °C).

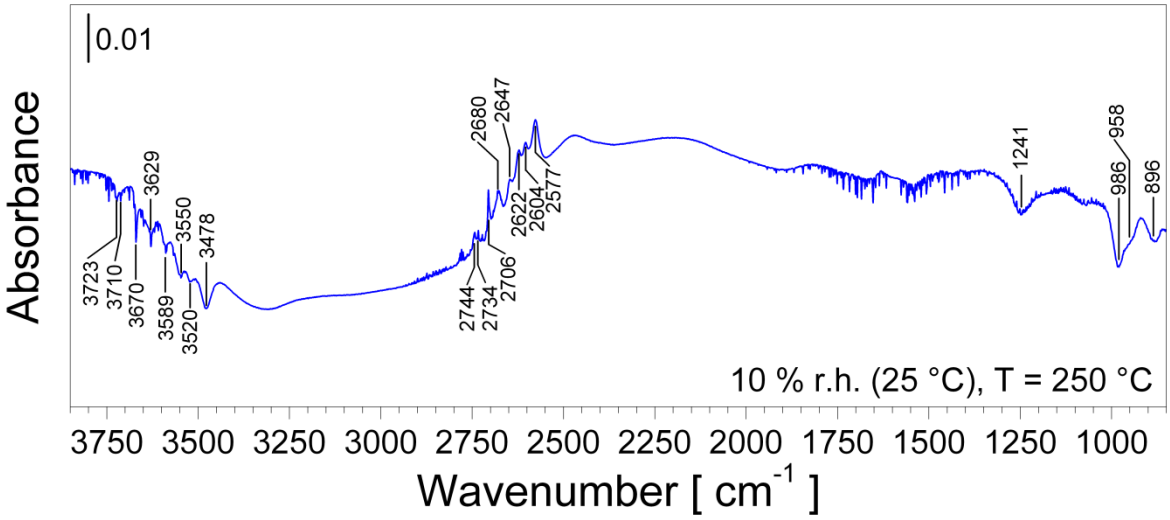

Supporting Figure 8. H_2O-D_2O exchange spectra of undoped SnO2 recorded at 250 °C. The water concentration was 10 % r.h. (25 °C).

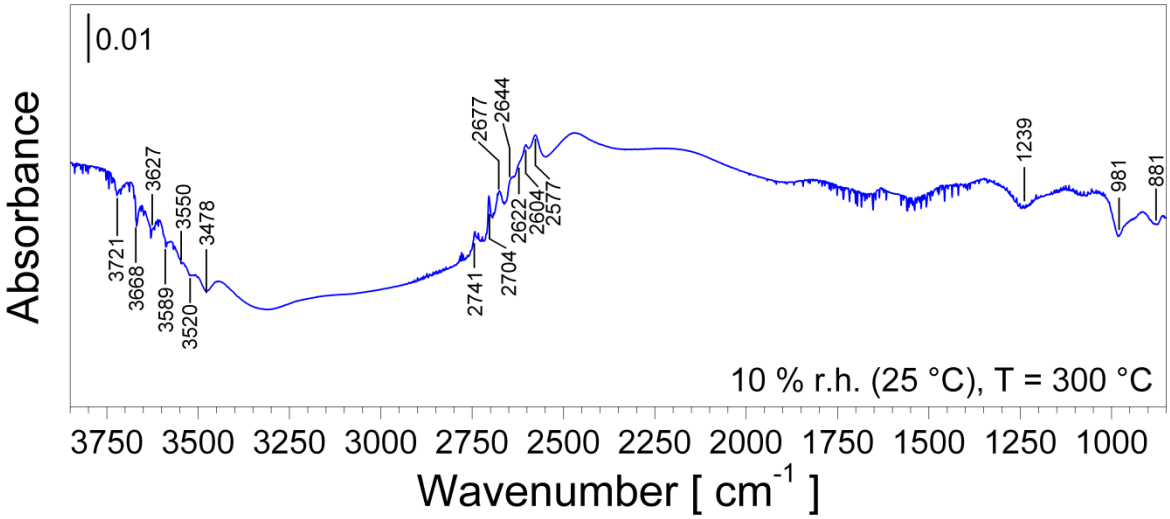

Supporting Figure 9. H_2O-D_2O exchange spectra of undoped SnO2 recorded at 300 °C. The water concentration was 10 % r.h. (25 °C).

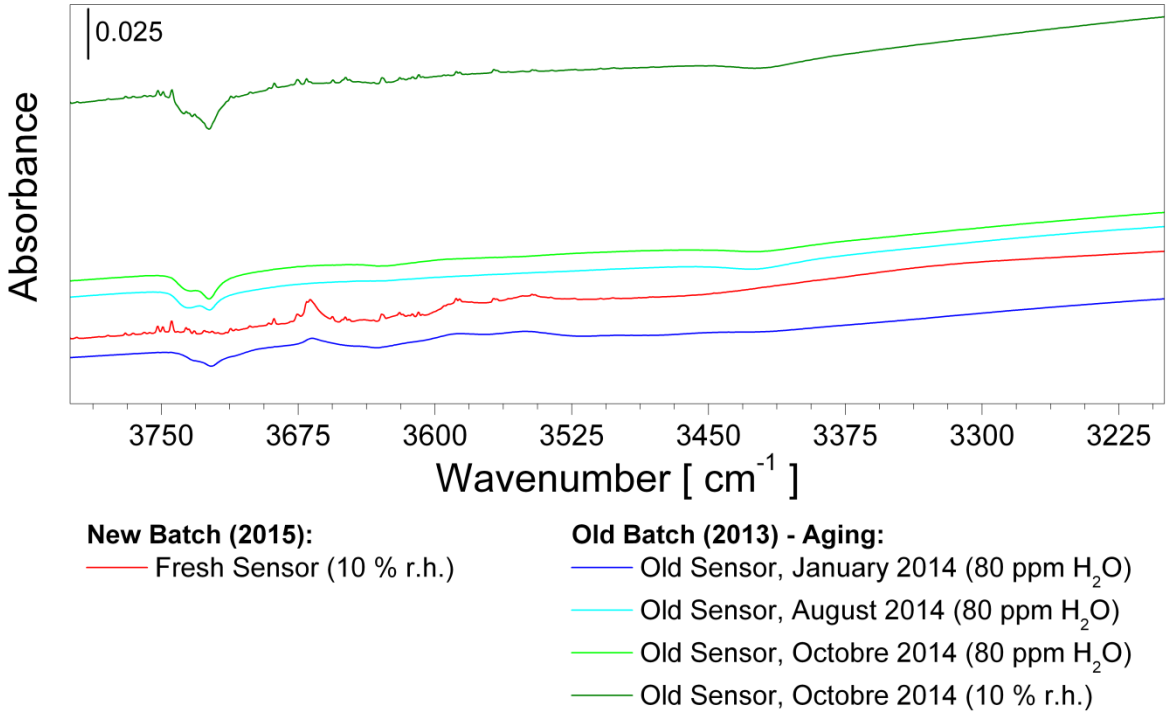

Supporting Figure 10. Comparison of the hydroxyl region during H_2O exposures on a fresh undoped SnO_2 gas sensors (red) and aged sensors from the same batch after several measurements (blue and green colours). The spectra show clear changes with time, i.e. an aging of the undoped SnO_2 material.

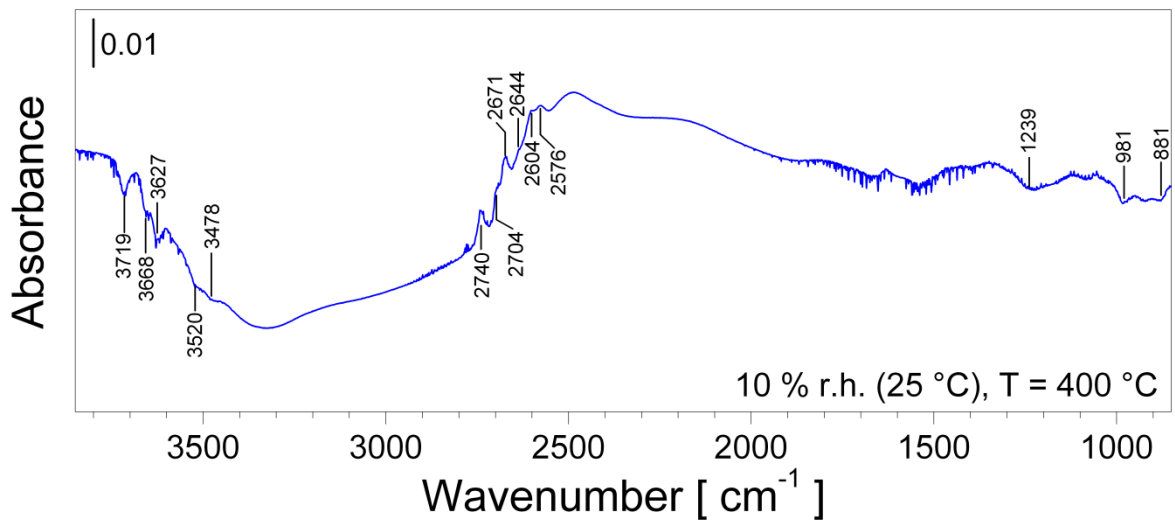

Supporting Figure 11. H_2O-D_2O exchange spectra of undoped SnO2 recorded at 400 °C. The water concentration was 10 % r.h. (25 °C).

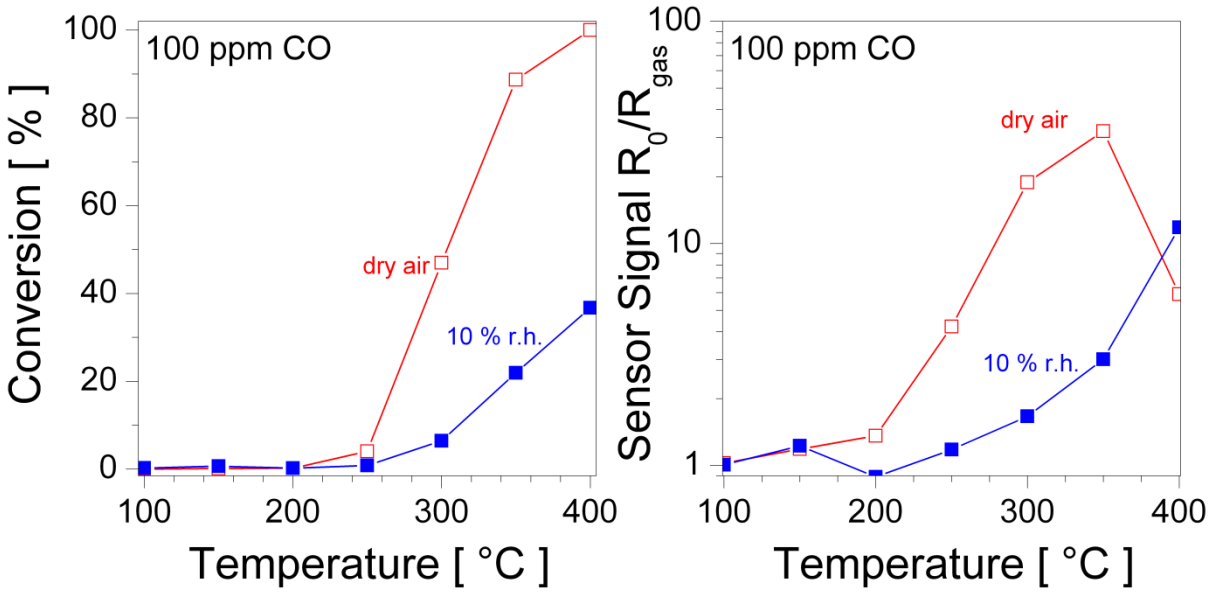

Supporting Figure 12. Catalytic conversion of 100 ppm CO measured on powders in dry and humid air (10 % r.h. at 25 °C) at different temperatures (left) and corresponding sensor signals measured under the same conditions (right). The trend in dry air is shown in red (empty squares), the trend in humid air in blue (filled squares).

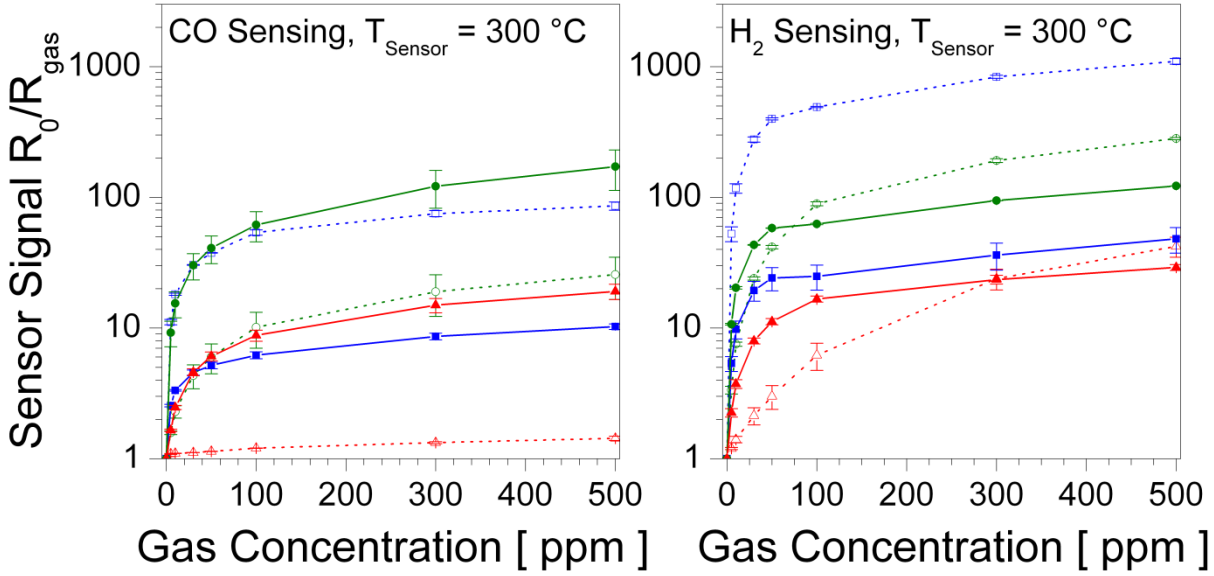

Supporting Figure 13. Gas sensing performance of undoped SnO_2 (blue squares), 0.2 wt% (green circles) and 2.0 wt% (red triangles) Pt-doped SnO_2 measured at 300 °C in dry air (empty symbols) and 50 % r.h. (filled symbols). The calibration curves for 5-500 ppm CO (left) and H_2 (right)of are based on the averaged sensor signal of three independently measured sensors.

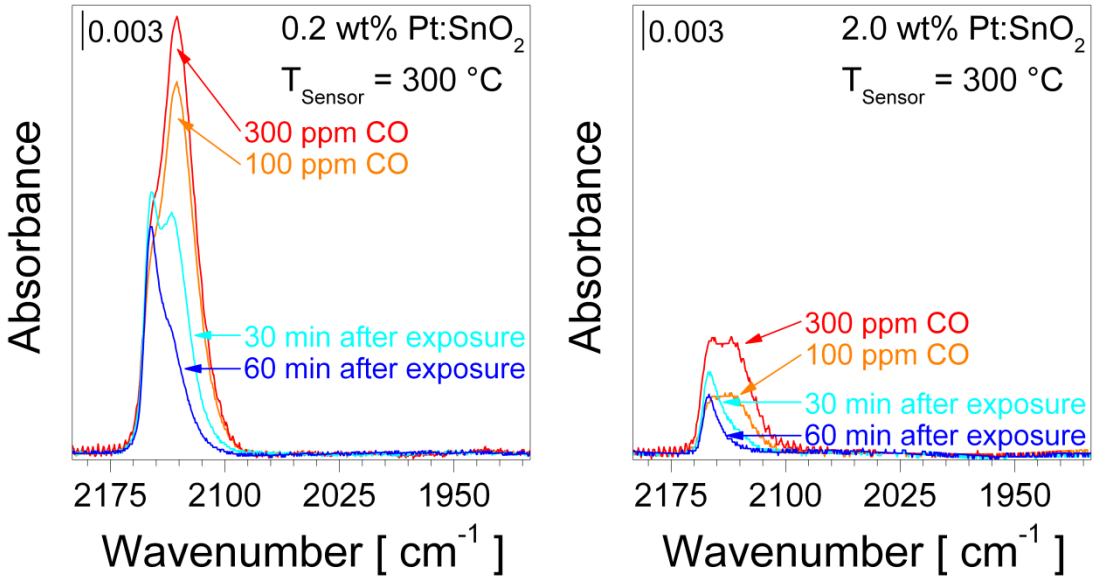

Supporting Figure 14. Baseline corrected carbonyl region of the DRIFT spectra of 0.2 wt% (left) and 2.0 wt% (right) Pt-doped SnO_2 during and after stepwise increased CO exposure: 100 ppm CO (orange), 300 ppm CO (red), 30 min after the exposure (cyan) and 60 min after the exposure (blue). The sensor temperature was 300 °C. The spectra were referenced to corresponding spectra recorded in dry air.

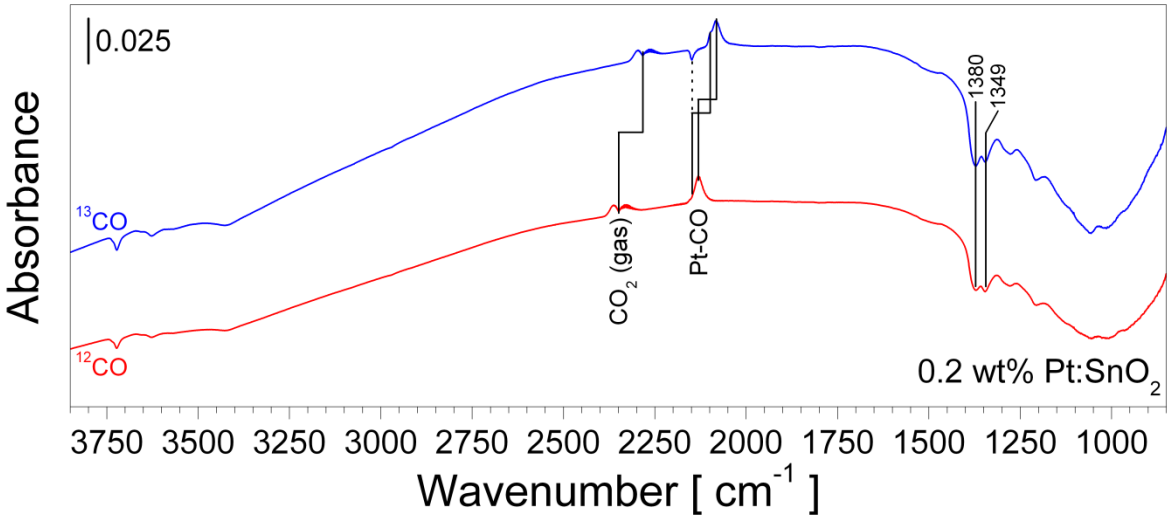

Supporting Figure 15. DRIFT spectra of 0.2 wt% Pt-doped SnO_2 exposed to 500 ppm of ^{12}CO in dry (red) and ^{13}CO (blue) in dry air. The sensor temperature was 300 °C. The spectra were referenced to a spectrum recorded in dry. The deviation of the exchange of the carbonyl band at higher wavenumbers (2148 cm^{-1}) is caused by CO which is still bound to the surface due to previous experiments.

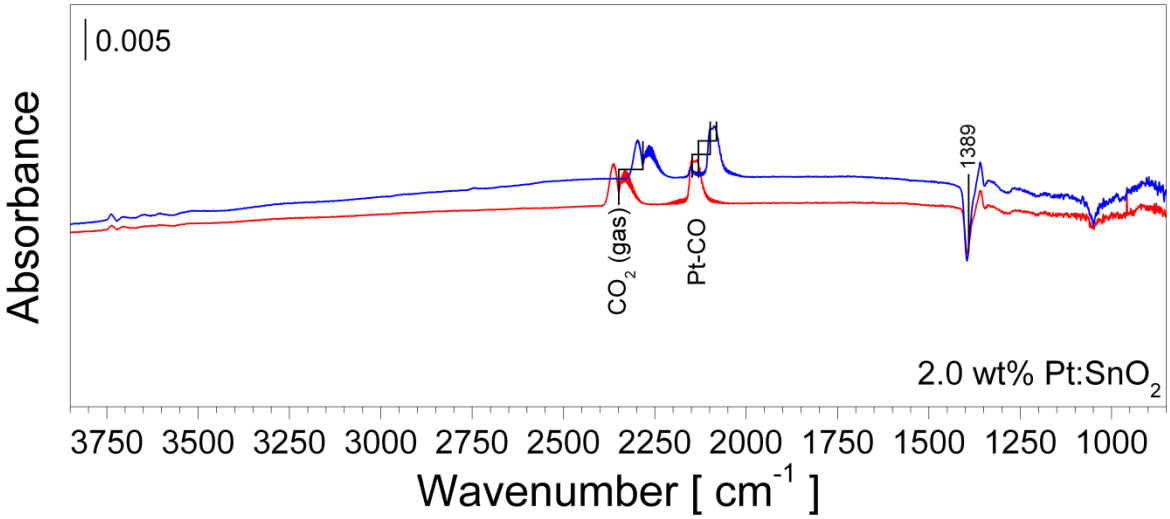

Supporting Figure 16. DRIFT spectra of 2.0 wt% Pt-doped SnO_2 exposed to 500 ppm of ^{12}CO in dry (red) and ^{13}CO (blue) in dry air. The sensor temperature was 300 °C. The spectra were referenced to a spectrum recorded in dry.

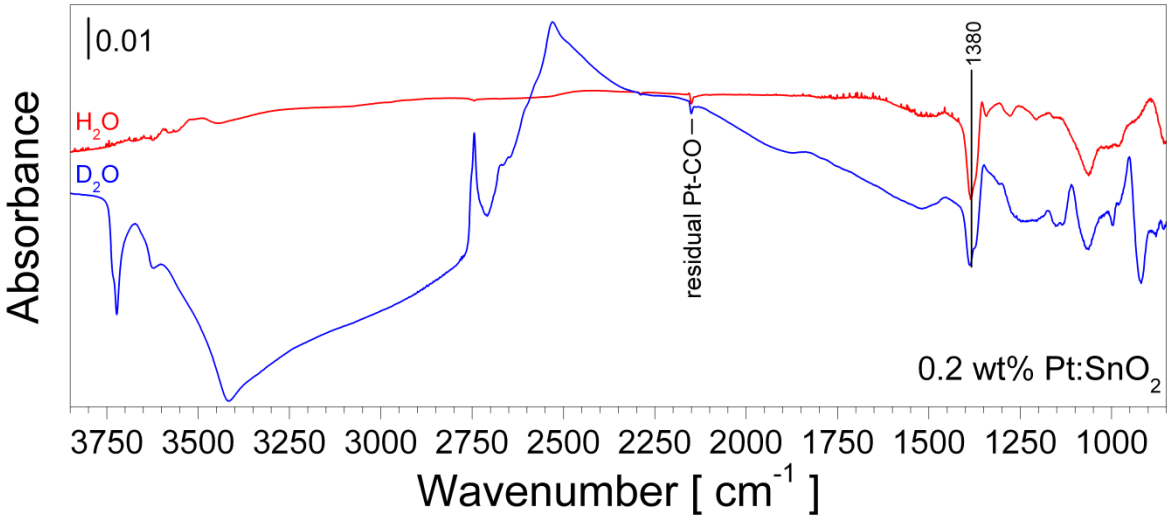

Supporting Figure 17. DRIFT spectra of 0.2 wt% Pt-doped SnO_2 exposed to H_2O in dry (red) and D_2O (blue). The water concentration was 10 % r.h. at 25 °C. The sensor temperature was 300 °C. The spectra were referenced to a spectrum recorded in dry.

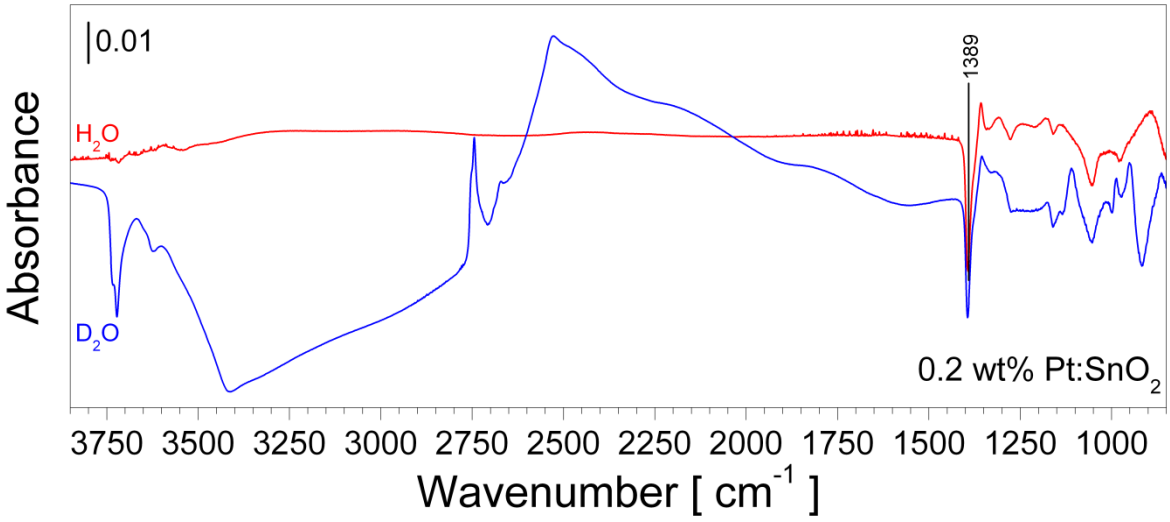

Supporting Figure 18. DRIFT spectra of 2.0 wt% Pt-doped SnO_2 exposed to H_2O in dry (red) and D_2O (blue). The water concentration was 10 % r.h. at 25 °C. The sensor temperature was 300 °C. The spectra were referenced to a spectrum recorded in dry.

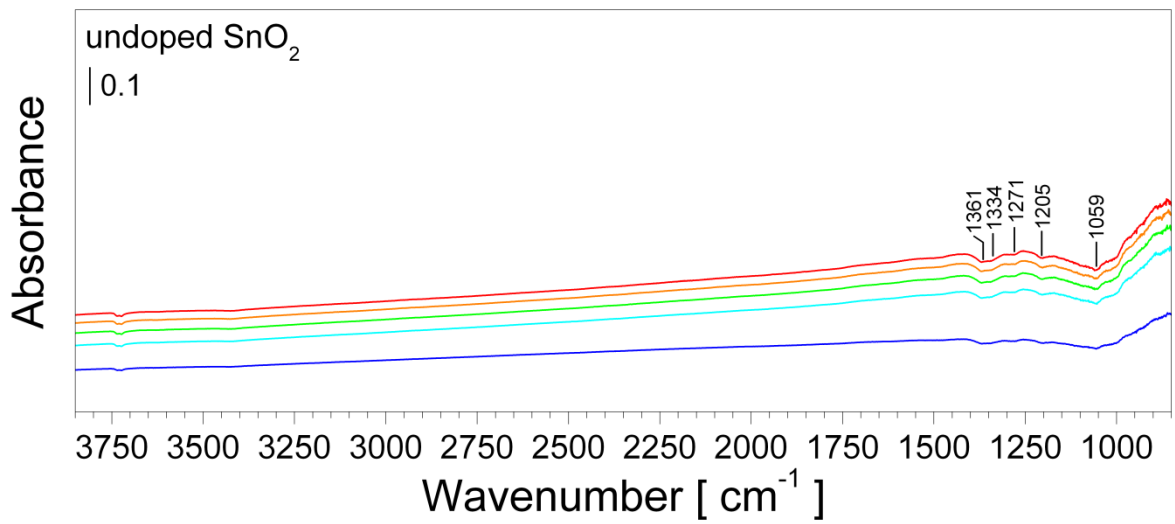

Supporting Figure 19. DRIFT spectra of undoped SnO_2 exposed to different CO concentrations in an O_2/N_2 mixture with 63.3 ppm O_2: 20 ppm CO (blue), 50 ppm CO (cyan), 100 ppm CO (green), 200 ppm CO (orange) and 500 ppm CO (red). The sensor temperature was 300 °C. The spectra were referenced to a spectrum recorded in in the pure O_2/N_2 mixture.

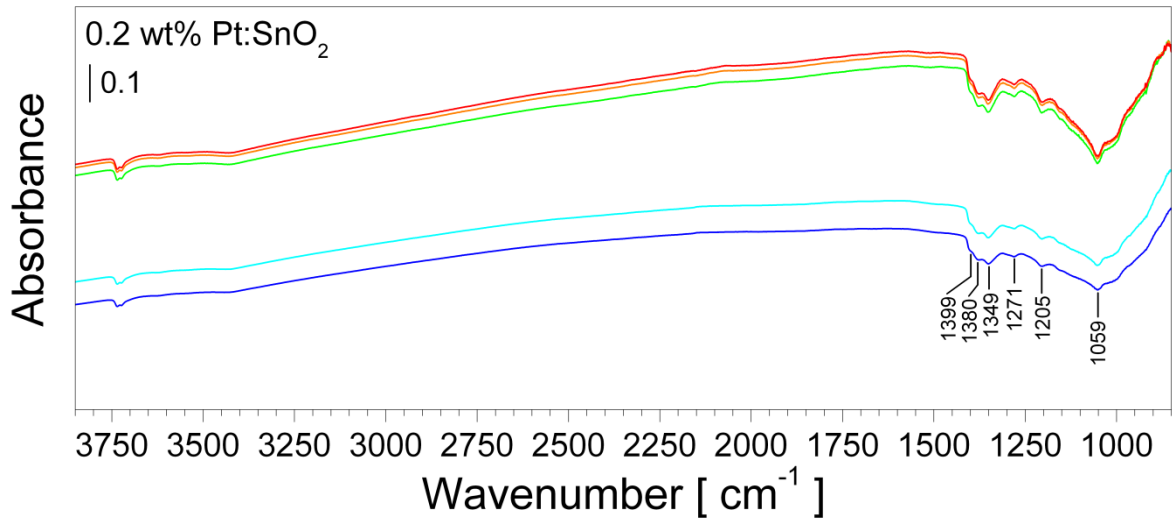

Supporting Figure 20. DRIFT spectra of 0.2 wt% Pt-doped SnO_2 exposed to different CO concentrations in an O_2/N_2 mixture with 66.5 ppm O_2: 20 ppm CO (blue), 50 ppm CO (cyan), 100 ppm CO (green), 200 ppm CO (orange) and 500 ppm CO (red). The sensor temperature was 300 °C. The spectra were referenced to a spectrum recorded in in the pure O_2/N_2 mixture.

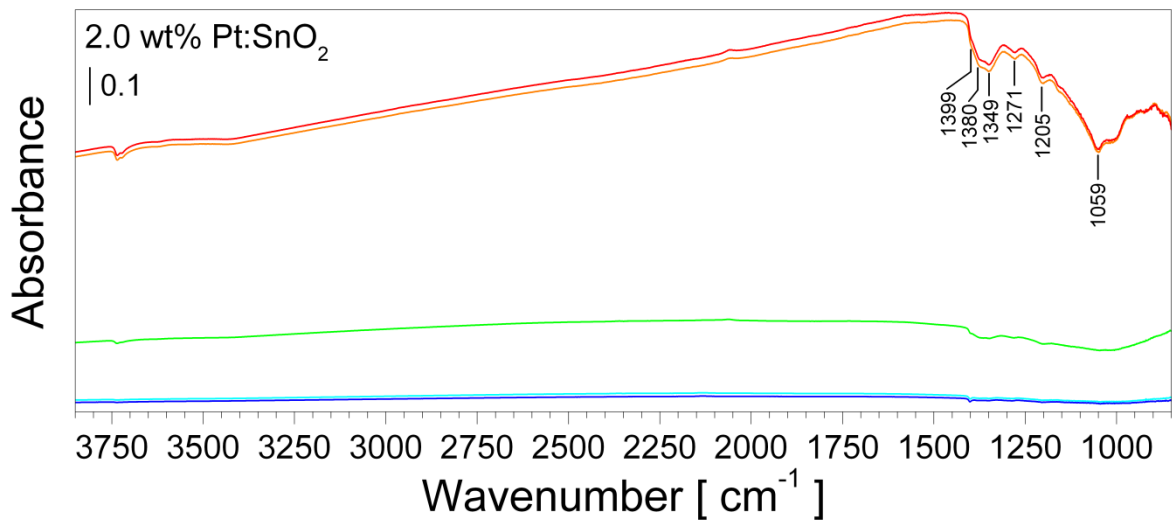

Supporting Figure 21. DRIFT spectra of 2.0 wt% Pt-doped SnO_2 exposed to different CO concentrations in an O_2/N_2 mixture with 63.9 ppm O_2: 20 ppm CO (blue), 50 ppm CO (cyan), 100 ppm CO (green), 200 ppm CO (orange) and 500 ppm CO (red). The sensor temperature was 300 °C. The spectra were referenced to a spectrum recorded in in the pure O_2/N_2 mixture.

11. Publications

Articles in peer reviewed journals:

- D. Degler et al., *Gold-Loaded Tin Dioxide Gas Sensing Materials: Mechanistic Insights and the Role of Gold Dispersion*, ACS Sensors, 1, 11, **2016**, 1322-1329
- D. Degler et al., *Structure and chemistry of surface-doped Pt:SnO_2 gas sensing materials*, RSC Advances, 6, **2016**, 28149-155.
- D. Degler et al., *Extending the toolbox for gas sensor research: Operando UV/vis diffuse reflectance spectroscopy on SnO_2-based gas sensors*, Sensors and Actuators B: Chemical, 224, **2016**, 256-259.
- D. Degler et al., *Identifying the active oxygen species in SnO_2 based gas sensing materials: an operando IR spectroscopy study*, The Journal of Physical Chemistry C, 119, **2015**, 11792-1179.
- D. Degler et al., *Structure-function relationships of conventionally and flame made Pd-doped sensors studied by X-ray absorption spectroscopy and DC-resistance*, Sensors and Actuators B: Chemical, 219, **2015**, 315-323.

Book Chapters:

- D. Degler & N. Barsan, *Experimental Investigations*, in *Gas Sensors Based on Conduction Metal Oxides*, by N. Barsan & K.-D. Schierbaum (editors), Elsevier, submitted
- H. W. P. de Carvalho et al., *Chapter 25: Sensors,* in *XAFS Techniques for Catalysts, Nanomaterials, and Surfaces*, by Y. Iwasawa, K. Asakura & M. Tada (editors), Springer International Publishing, **2017**, 383-396

Oral Presentations at Conferences:

- D. Degler et al., *Operando X-ray absorption spectroscopy: A key technique to understand the structure-function-relationship of noble metal doped gas sensing materials*, 16th International Conference on X-ray Absorption Fine Structure, 23-28 August, **2015**, Karlsruhe, Germany
- D. Degler et al., *Identification of the reactive oxygen species on SnO2 by using operando spectroscopy*, 4th GOSPEL Workshop GSSMO 2015,07-09 June, **2015**, Tübingen, Germany
- D. Degler et al., *In-situ and operando X-ray spectroscopy – a suitable tool to reveal the structure of noble metal doped sensing materials*, The 15th International Meeting on Chemical Sensors, 16-19 March, **2014**, Buenos Aires, Argentina

Poster Presentations at Conferences:

- D. Degler et al., *Neue Einblicke in die Struktur palladiumdotierter SnO2 Gassensoren mittels Röntgenabsorptionsspektroskopie*, 11. Dresdner Sensor-Symposium,9-11 December, **2013**, Dresden, Germany
- H. W. P. de Carvalho et al., *Operando-spectroscopic Study on the Structure Function Relationship of Pd-doped SnO2 Gas Sensors*, 12th Bunsentagung (Annual German Conference on Physical Chemistry), May, 9-1, **2013**, Karlsruhe, Germany
- D. Degler et al., *Metallphthalocyanine und deren Anwendung in der Gassensorik*, ANAKON, March 22-25, **2011**, Zurich, Switzerland

12. Curriculum Vitae

Personal data

Name : David Walter Degler
Date of birth : 14.10.1986
Place of birth : Reutlingen, Germany
Nationality : German

Education

04/2016-05/2016	Research stay in the group of Prof. A. Urakawa at Institute of Chemical Research of Catalonia (ICIQ) in Tarragona, Spain – *Development of time-resolved spectroscopic methods and automated signal/data processing* Funding was received from the German Academic Exchange Service (DAAD).
since 04/2013	PhD student in the group of Prof. U. Weimar & Dr. N. Barsan at the Eberhard Karls Universität, Tübingen, Germany Title of PhD thesis: "*Spectroscopic Insights in the Gas Detection Mechanism of Tin Dioxide Based Gas Sensors*"
03/2013	Final degree in chemistry (Diplom im Fach Chemie) Title of diploma thesis: "*An Electrical and Spectroscopic Study of Surface Doped Tin Dioxide Gas Sensors*"
06/2011-07/2011	Research stay in the group of Prof. K. Persaud at the University of Manchester, United Kingdom – *Comparison of classical analytical methods (GC/MS) and sensor arrays for the detection of chlorination byproducts in drinking water*
10/2007-03/2013	Studies at the Eberhard Karls Universität Tübingen
09/1997-06/2006	Secondary school (Dietrich Bonhoeffer Gymnasium, Metzingen)
09/1993-07/1997	Primary School (Freie Evangelische Schule, Reutlingen)

Further work experience

09/2006-05/2007	Alternative military service (Zivildienst), working nine months with disabled people

Memberships

since 2009	Member of the German Chemical Society (GDCh) and the GDCh subsection for analytical chemistry
since 2017	International X-ray Absorption Society (IXAS)

13. Academic Teachers

K. Albert, R. Anwander, N. Barsan, T. Chassé, D. Christen, G. Gauglitz, S. Grond, S. Keppler, N. Kuhn, H.-G. Mack, M.E. Maier, H.A. Mayer, A. Meixner, H.-J. Meyer, U. Nagel, C. Ochsenfeld, A. Oprea, E. Schweda, B. Speiser, U. Weimar, L. Wesemann, D. Wistuba, K.-P. Zeller, T. Ziegler

14. Acknowledgements

First and foremost, I'd like to thank Dr. Nicolae Barsan for the opportunity to work on this PhD thesis, his patience and humor in all scientific and non-scientific discussions and nonetheless for his great support. After all the joint research I agree with the words of Robert W. Bunsen "A chemist, who's not a physicist, is nothing", but not without adding that the same applies vice versa.
I would like to express my sincere gratitude to Prof. Dr. Udo Weimar for his kind and encouraging character as well as for giving me the opportunity to join his group as an undergraduate student and to conduct my diploma and PhD thesis in his group.
I could not have imagined having better mentors for my PhD study than Prof. Dr. Udo Weimar and Dr. Nicolae Barsan. Thanks for all the opportunities to visit conferences and other research groups - these experiences intensified my interest in research and interdisciplinary cooperation.

Besides my advisor Prof. Dr. Udo Weimar, I would like to thank the other members of my thesis committee: Prof. Dr. Carolin Huhn, Prof. Dr. Günter Gauglitz and Prof. Dr. Reiner Anwander. Furthermore, a special thanks to Prof. Dr. Günter Gauglitz for writing the second report.

I wish to express a genuine thank you to Prof. Dr. Jan-Dierk Grunwaldt and his group for the great cooperation and the interesting insights in the fields of catalysis and X-ray spectroscopy. Especially I would like to thank Dr. Sabrina Müller, Dr. Dmitry Doronkin and Prof. Dr. Hudson W. P. Carvalho for the joint work on the structure of noble metal loadings and the evaluation of the results obtained by X-ray absorption spectroscopy and transmission electron microscopy.

My sincere thanks also goes to Prof. Dr. Atsushi Urakawa for the opportunity to work at his laboratory and to his group for the great hospitality during my stay in Tarragona.

I dearly thank my colleagues and all members of the Weimar research group for their help, all scientific and non-scientific discussions; I thoroughly enjoyed each and every one of them. In particular I would like to thank Anna Stearz, Dr. Susanne Wicker and Dr. Julia Rebholz for the great cooperation and the inspiring discussions. Furthermore, I thank Dr. Alexandru Oprea for his great patience, advice and support concerning all kinds of experimental work.

A special thanks to my parents Lydia and Dieter, my brother Johannes and my girlfriend Hanna. Words cannot express how grateful I am for your continuous encouragement and support over all those years.